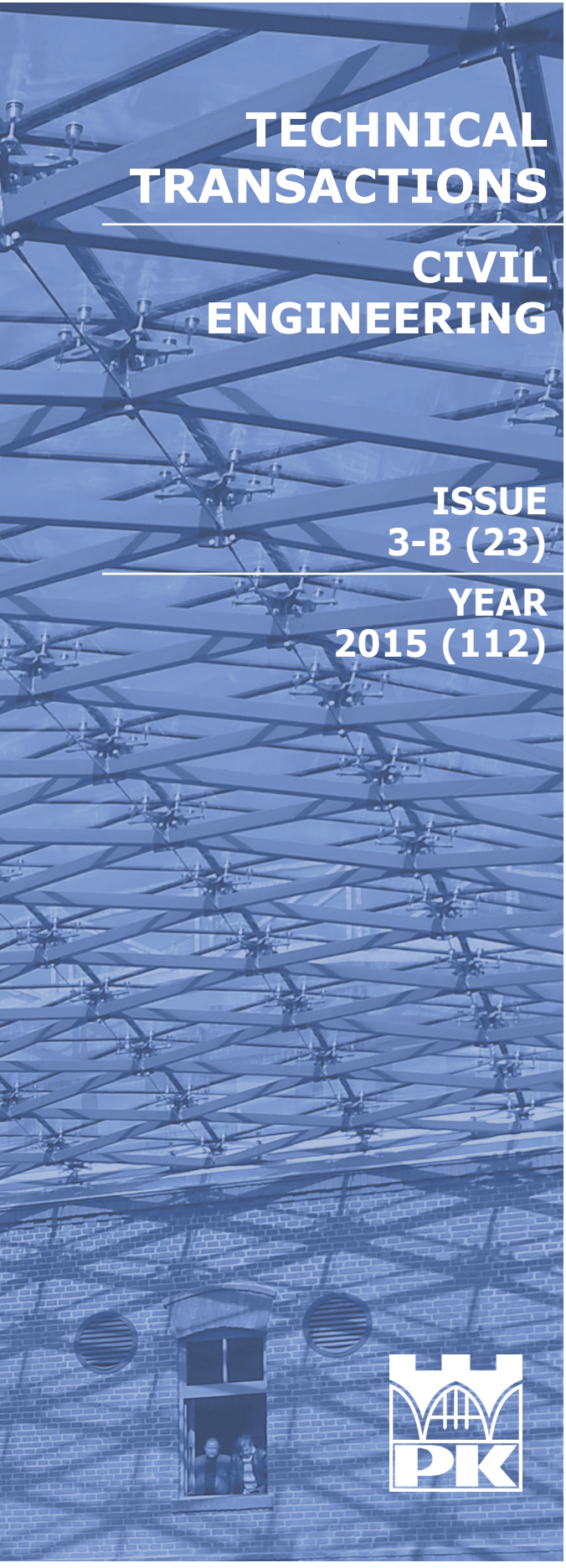

TECHNICAL TRANSACTIONS
CZASOPISMO TECHNICZNE

CIVIL ENGINEERING
BUDOWNICTWO

ISSUE 3-B (23)
ZESZYT 3-B (23)

YEAR 2015 (112)
ROK 2015 (112)

WYDAWNICTWO POLITECHNIKI KRAKOWSKIEJ

TECHNICAL TRANSACTIONS | CZASOPISMO TECHNICZNE

CIVIL ENGINEERING | BUDOWNICTWO

ISSUE 3-B (23) | ZESZYT 3-B (23)
YEAR 2015 (112) | ROK 2015 (112)

Basic version of each Technical Transactions magazine is its online version
Pierwotną wersją każdego zeszytu Czasopisma Technicznego jest jego wersja online
www.ejournals.eu/Czasopismo-Techniczne www.technicaltransactions.com www.czasopismotechniczne.pl

Civil Engineering Series
3-B/2015

TECHNICAL TRANSACTIONS | CZASOPISMO TECHNICZNE
CIVIL ENGINEERING | BUDOWNICTWO
3-B/2015

HENRYK CIUREJ*, PIOTR GWOŹDZIEWICZ*, ANTONI MAZERA**

ATYPICAL EXAMPLE OF THE REDUCTION OF THE SAFETY AND DURABILITY OF A TYPICAL MOTORWAY OVERBRIDGE

NIETYPOWY PRZYPADEK ZMNIEJSZENIA BEZPIECZEŃSTWA I TRWAŁOŚCI TYPOWEGO WIADUKTU NAD AUTOSTRADĄ

Abstract

The present paper is related to the motorway overbridge, the technical state of which has been showing deficiencies related mainly to the presence of cracks. Verification of the design and construction documents was carried out prior to advanced analysis which covered the construction process with phases, loads acting in various periods of time as well as the progressing ground deformations. Conclusions drawn on the basis of the analysis results are not typical because the emergency situation is resulting from many simultaneously acting factors. The level of the reduction of the safety margin of the bridge has been estimated.

Keywords: *prestressed concrete, emergency state, analysis, finite elements method, prestressing technology, settlement, safety, durability*

Streszczenie

Opracowanie dotyczy wiaduktu nad autostradą, którego stan techniczny wykazywał nieprawidłowości związane głównie z obecnością zarysowań. Przeprowadzono weryfikację dokumentów z czasu budowy obiektu oraz zaawansowane analizy obliczeniowe obejmujące proces budowy, panujące obciążenia, a także postępujące odkształcenia podłoża. Wnioski wysunięte na podstawie analiz mają nietypowy charakter, ponieważ awaryjny stan ustroju jest wynikiem splotu wielu jednocześnie występujących czynników. Zmniejszenie zapasu bezpieczeństwa oraz trwałości obiektu zostało oszacowane.

Słowa kluczowe: *beton sprężony, awaria, analiza, metoda elementów skończonych, technologia sprężenia, osiadanie, bezpieczeństwo, trwałość*

DOI: 10.4467/2353737XCT.15.158.4333

* Ph.D. Eng. Henryk Ciurej, Ph.D. Eng. Piotr Gwoździewicz, Cracow University of Technology, Faculty of Civil Engineering.

** Msc. Eng. Antoni Mazera, Biuro Projektów Konstrukcyjnych, Cracow.

1. Introduction

The present paper is related to a bridge structure located at a G2 class main road axis over a motorway in the south of Poland (Fig. 1). The bridge built over the motorway is composed of two parallel, load-bearing structures. The cross-section of each of them is composed of three girders and there are six spans along the length of the bridge. The angles of intersection with supports and abutments axes are variable. The bridge is built in an area of geologically non-stable ground – this fact was already known at the time of construction. In effect of the ground settlements, redistribution of internal forces in the load-bearing structure was possible and this effect could provoke the structure overloading.

Fig. 1. View of the structure

On the basis of the owner's reporting of the presence of visible damage to the surface of the bridge members, complex investigation of the load-bearing structure was carried out. An advanced level of damage was observed, in particular represented by cracks on the surface of the structure.

The question of the reduction in bridge safety levels as an effect of progressive damage is raised frequently. The usual description of the problem is related to the corrosion process (e.g. [1]). The case which is the subject of the present research includes a substantial influence of nonconformities generated at the time of construction as well as related to external impact – for these reasons, it is more complex in comparison to the usual examples.

The aim of this work is to present: observed irregularities in the technical condition of the structure; the performed tests and analyses; conclusions relating to the possible origins of the existing damage; the influence of the damage on structural safety and durability. Additionally, a description of the structure is presented, the observed nonconformities and damage, and the results of the evaluation with regard to safety.

2. Description of the bridge and its history

A continuous six-span viaduct made of prestressed concrete with a total length of 180.88 m; its transversal cross-section consists of three main girders of a trapezoid cross-section joined with a deck slab of 0.25 m. The width of the structure reaches 13.70 m. The depth of the main girder is constant at 1.50 m, while the width varies from 1.20 m to 1.80 m from the bottom edge to the top. The axial spacings of the main girders are 4.30 m.

Girders are stiffened by the transverse beams located in the midspans as well as over the piers. Slab cantilevers are designed at the side girders and their length reaches 1.6 0 m. Length of the spans equals from east to west: 27.0 m, 29.22 m, 29.22 m, 33.25 m, 33.25 m and 27.0 m. Two angles of intersection between the main structure and the abutments line are different and their values are 49.84° and 60.83°.

The load-bearing structure is supported by column piers and abutments. All supports are based on reinforced concrete piles with a diameter of 1500 mm.

The bridge includes standard features: SMA runway pavement of the regular thickness; modular expansion joints; concrete pavement slab covered with an epoxy surface insulation; stone corbels; barrier and guard-rail. With consideration to the structural work, attention was paid to the fixed bearing position at the bridge abutment.

The bridge was designed in the end of nineteen-nineties, and its construction was executed in the years 2001–2003. Only a portion of the archived construction documents are available, the preserved documents are mainly related to the prestressing operation. These circumstances were considered as a reliable reference which, with additional assumptions described further, could be used for an analytical approach to the structure load-bearing capacity.

The design documents subjected to investigation allow the assumption that during the construction period, one of the principal difficulties was related to the state of the ground. At various points in the documents, expressions related to the operation of the ground compaction (consolidation) are present. These circumstances influenced the decision to change the solution used for the foundation of the piers, initially designed as supported directly on the concrete footing. The construction schedule of subsequent parts of the structure was also subjected to change. Initially, it was assumed that the bridge would be built in five phases starting from the eastern abutment, finally both, – the final construction drawings as well as the construction documents describe the progress of works starting from the western side. Additionally, initial analysis of the construction design and documents revealed an important difference between the values of the permanent prestressing forces in the design at the building permit phase and the design in the executive phase – in the other documents, the values of the forces are around 30% lower than in the first ones. The modifications introduced also influenced the details of the execution of prestress – it was decided that the grouting of cable ducts located in the bridge sections built in phases 4 and 5 would be carried out in one step.

3. Testing of the structure

The structure was subjected to tests aimed at evaluating the extent of damage. These tests were performed due to irregularities in the technical state of the bridge, particularly

a significant settlement of the runway in the immediate proximity of the bridge as well as the advanced cracking morphology of the beams.

The measurements of the runway presented a significant unevenness in the surface shape concentrated in particular in the road section approaching the bridge from the west. As a result of the settlement, a 6 cm ramp for vehicles arriving on the bridge from west was present. In the analysis, the dynamic factor for the loads was assumed to be at its utmost level.

In order to assess the state of the bridge in the area of the observed cracks, several tests were carried out. In the main program of testing, drilled cores were collected, passing through the observed cracks in the side beam of the side span from the west. The first of the cores was cut through the upper crack of 1.5 mm; the second, through the lower crack of 0.8 mm. The drill through the first of the crack delivered the following information:

– 15 cm from the surface, concrete cover was splitted by a vertical plane of crack,
– full inspection of the prestressing tendon duct in the area adjacent to the coupling anchorage in the joint of the segments was possible by means of opening the conical shield of the cable coupling anchorages.

Within the framework of the investigation, the quantity and positioning of the reinforcement were also verified, followed by checks of its state and the cover thickness.

Apart from destructive testing in the form of drilled cores, several other types of tests were conducted, both destructive as non-destructive. Tests were carried out by two independent laboratories. Cylinders, the diameters of which were 100 mm, were cut from the investigated bridge span and were used to assess the compressive strength and the secant modulus of elasticity. The strength results obtained for the tested cylinders were 60.7 MPa, 70.9 MPa, 70.3 MPa and 52.6 MPa. These values confirm that the concrete strength in the bridge was substantially higher than the strength related to the B40 concrete class assumed in the design (class description following the bridge code of the time [2] and laying between C30/37 and C35/45). Similar results were obtained with the pull-out test (results reported are from 40.5 MPa to 84.7 MPa) and with sclerometric tests (concrete class estimated was C40/50 or C45/55). Concrete splitting resistance, measured with the pull-off method, reached slightly above 2.0 MPa – this refers to the tensile resistance for class C20/25. On the other hand, measurements of the modulus of elasticity demonstrated that not all characteristic parameters of concrete are increased in a similar way. The value of the modulus of elasticity complies with the requirements of the typical values for class B45 (C35/45) only. Similarly, volume weight of the concrete collected from the structure proved to be 7% lower than the weight of typical concrete with basalt gravel. The measured properties of concrete present an important scatter.

In addition to the strength tests, chemical analysis was also carried out – the results confirmed the alkaline property of concrete with the pH value exceeding 11.

4. Description of the structural damage

Clearly visible cracks served as the fundamental reason to undertake the tests and evaluation of the technical state of the structure. In the western side span of the bridge, the south girder was the most damaged. Numerous horizontal and skew cracks were concentrated mainly in the area located more than 5.0 m from the support towards the abutment. The area

with a high concentration of cracks is located directly at the construction joint, which is 5.0 m from the support. Fig. 2 presents the crack distribution over the surface of the beam together with the position of the cable ducts and the joint between the construction segments built successively.

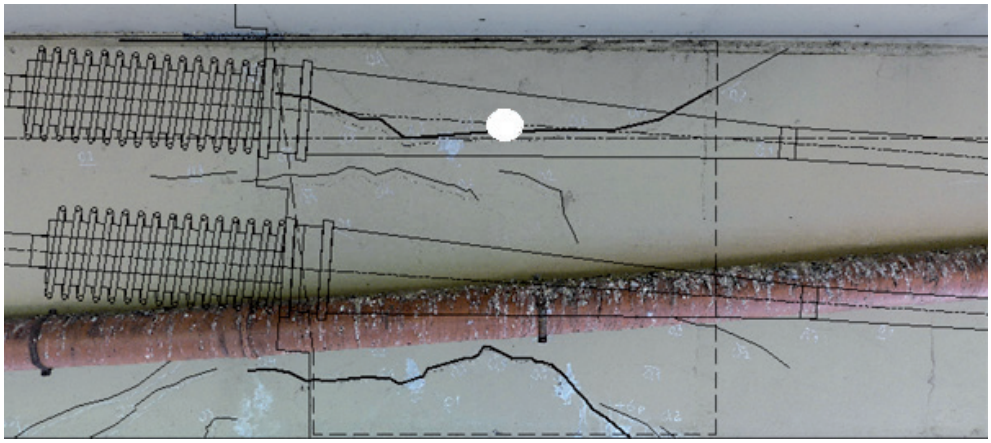

Fig. 2. Layout of cracks on the beam surface and the position of the joint between the structure segments and prestressing cable ducts

Due to the large width of cracks observed on the member's surface, the decision was taken to drill a core specimen along one of the cracks. The aim of this drill specimen was to investigate the depth and direction of the crack. The drilling was positioned at the level of the axis of the upper prestressing tendon, where the diameter of the cable duct progressively changes from 275 mms at the coupler to 100 mms at the entrance to the regular cable duct. In Fig. 2, the position of the drill is shown (indicated with a white dot). Because the crack width (Fig. 3) observed in the direction perpendicular to the surface was not decreasing, the drilling continued until the steel cover of the cable duct was reached. Inspection of the drill surface revealed the presence of another crack perpendicular to the drill axis and located 80 mm below the concrete surface. This crack is visible in the upper part of the drilled wall, slightly before the steel shield of the cable duct (Fig. 4). The observation of the crack inside of the drill specimen is in line with another observation of the concrete cover spalling – this was confirmed by means of an acoustic check of the concrete surface using a metal hammer.

Fig. 3. Crack position in the drill wall of the beam under investigation

Fig. 4. View into the drilled hole in the girder subjected to investigation. The steel cover of the prestressing cable duct and its interior are visible

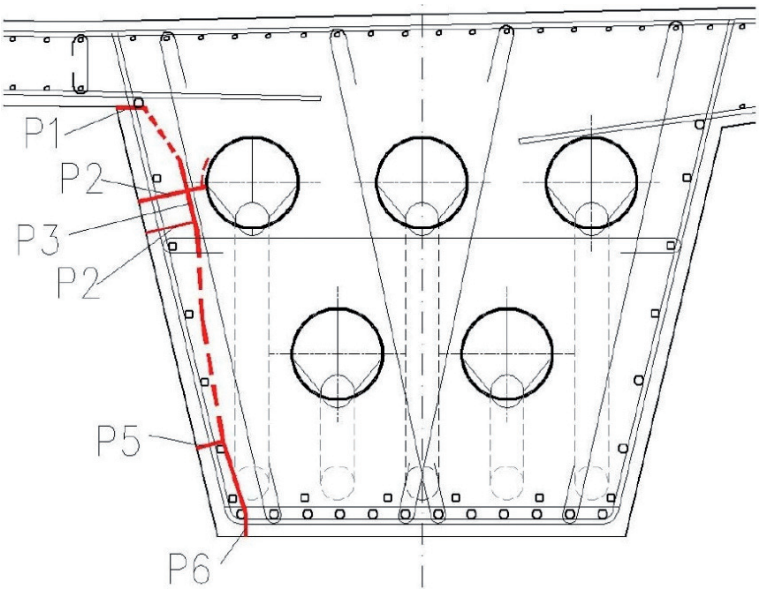

Fig. 5. Spalding of concrete along the depth of the girder – the continuous line represents the observed cracks, the dashed line represents their hypothetical trajectory. P1 to P6 – observed locations of cracks

The acoustic check indicated that the spalled layer occurs on the whole vertical edge of the beam from the slab at its top to the bottom edge and the length of the damaged area along the beam exceeds 2.5 m. The position of the observed splitting and its hypothetical trajectory are shown in Fig. 5.

The existence of the mesh cracking of concrete was observed in several zones of the bottom surface of the girders independently from the damage observed in the side span. The width of the cracks in these areas was measured at 0.1 mm and their directions were both parallel and perpendicular to the member axis. The layout of the cracks is similar to the distribution of the reinforcement in the girders. Verification by means of hammering has shown that the depth of the cracks reached 5–10 mm. The area of the widest cracks of this type from all surfaces of the girders was observed in the fourth span. In all areas of the mesh fissures their width in both directions is similar. It is suprising because prestressing of the girders introduced in the longitudinal direction has no influence on the cracks width although it should be expected that the prestress should force the perpendicular cracks to close.

Cracks of smaller widths (less than 0.05 mm) are observed on the girders' surface in many areas. Their presence may result from concrete shrinkage as well as thermal deformations of beams at the time of the concrete hardening. A partial explanation of their presence may be related to the diameter of the main reinforcing bars (28 mm) as well as the low cover thickness reaching only 35 mm.

Observations regarding materials inside of the structure in the area of drilled cores also brought many interesting observations. After penetrating the cable duct shield, it was found that instead of the duct being completely filled with cement grout as expected, there was a substantial lack of grout (Fig. 4). Punctual corrosion of the stressed, exposed prestressing strands was also found inside of the duct. The mortar filling the bottom part of the prestressing cable duct was non-cohesive – it was in the form of a powder with a grain size of 1–4 mm and with a white-beige colour. The lack of grout in the proper form, local corrosion of the prestressing strands as well as the corrosion points on the surface of the cable duct shield are evidence of the risk of tendon corrosion. The interior of the cable duct is shown in Fig. 6. Naked strands, local corrosion of the prestressing steel as well as of the internal surface of the duct shield was observed. Moreover, concrete splitting from the external surface of the cable duct shield was also observed (Fig. 4).

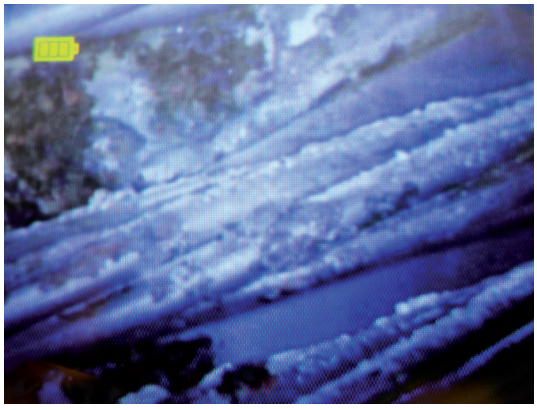

Fig. 6. View of the interior of the prestressing cable duct

Although initially it was considered that the position and corrosion levels of the prestressing cables be verified by means of projection [3], based on the relatively good condition of the prestressing cables and the existing cement grout in the ducts in other locations and cables, the concrete investigation was limited to drilling.

Subsidence is a major problem for the whole structure. The geodetic measurements which are available for the entire eleven-years history of the bridge prove large settlements

values and their important relative differences. The west abutment is the most exposed to the effects of subsidence and as a consequence, this support settled by 55.5 mm. Table 1 shows the medium settlement values for the supports of the bridge at the end of the monitoring period. The largest observed relative settlement is more than five times greater than the usual design assumption of 10 mm. For this reason, the influence on the structural safety must be investigated.

Table 1

Total settlement values of the bridge piers over 11 years of service

	Support number						
	A	B	C	D	E	F	G
Mean settlement [mm]	55.5	12.8	15.6	19.7	6.2	5.0	3.3
Relative settlements [mm]	42.7						
		2.8					
			4.1				
				13.5			
					1.2		
						1.7	

Although the support deformations are relatively large, their overall distribution only has a slight influence over the internal forces in the bridge girders. This is due to the relatively low bending rigidity of the main girders. Nevertheless, this influence is included in the presented results.

The damage and irregularities of the structure subjected to analysis are of various origins; however, they simultaneously influence its durability and safety. In order to assess the aggregate influence of the observed deficiencies, complex analysis of the structure was carried out as described below.

5. Varying safety margin for the bridge

5.1. Limit states verifications of the load-bearing structure according to the design phases

Prestressing force reduction

In the framework of safety verification of the structure, detailed analysis of the available documents relating to the bridge was carried out. All of the assumptions made as well as the static model formulation were declared to be correct. One of the principal observations based on the data included in the documents is related to the values of the prestressing forces. The notional tensile resistance of the 19T15 prestressing cables used in the design is:

$$F_d = f_{pk} A_p = 1860 \text{ MPa} \cdot 19 \cdot 1.50 \text{ cm}^2 = 5301 \text{ kN}$$

The generally governing admissible level of maximal stressing force reaches 80% of this value:

$$P_{0max} = 0.80 \cdot 5301 \text{ kN} = 4240.8 \text{ kN}$$

In the design at the phase of the building permit the permanent prestressing forces (after all losses) were estimated and the final stressing level of the tendons was assumed at the level of 59% to 68% of the admissible stress level (see Tab. 2). Such low tension was resulting from the decision of a relatively low initial stress level in prestressing cables as well as the friction losses in cables stressed only at one end. Nevertheless, the construction drawings created at the next step of the project process – at the final phase of design – provide the values of the permanent prestressing forces reaching 41% to 49% only of the admissible stressing forces (also see Tab. 2). In accordance with the values given in the construction drawings, prestressing procedures were formulated and approved; furthermore, tensioning of cables was carried out. Considering the lack of both substantiation for such prestressing force reduction as well as of controlling evaluation of its influence on the load-bearing conditions, a check-up calculation of the bridge girders was undertaken.

Table 2

Permanent prestressing force in the spans in the initial and construction design

Span No.	Final force (initial design) [kN]	Final force (construction design) [kN]
1	2513	1745
2	2427	1781
3	2873	1781
4	2493	1787
5	2813	1788
6	2480	2032

A lower value of prestressing forces in the bridge structure, which could potentially result from a misunderstanding of the design provisions from the first phase, has an influence on the static effect of prestress. It was estimated that proportional to the force decrease, the bending moments as well as compression forces provoked by prestress are 19% lower than initially assumed. As a result, the safety margin for normal stresses in cross-sections is reduced and in many sections of the girders, cracking of the concrete at the bottom surface of the spans may appear. Moreover, lower prestressing forces influence the load-bearing capacity for bending. The principal conclusions regarding this problem are presented further in this paper.

Load-bearing capacity for bending

The varying safety margin for the member regarding its load-bearing capacity for bending was investigated in accordance with the Eurocode 2 approach [4]. Table 3 gives the maximal bending moment resulting from the loads. The influence of the force decrease is presented for span 6, which is where the damage was observed.

Table 3

Maximal bending moment for the final situation

Span/Support No.	Maximal bending moment [MNm]
1	8.19
B	–11.62
2	7.91
C	–13.21
3	9.36
D	–12.61
4	8.13
E	–11.10
5	9.18
F	–11.76
6	8.08

In this evaluation, the influence of the supports settlement was also accounted for. Its general effect is positive due to the fact that the static bending moment is reduced as an effect of this deformation. The load-bearing capacity for bending estimated following the simplified approach – from the equilibrium conditions – equals $M_{Rd} = 10.63$ MNm. The relative decrease of the capacity estimated with the general approach (following the strain diagram in cross-section) was showing 10.3% reduction of the initial value. In effect, the safety margin for the member cross-sections drops from 31.6% to 18% and this has a substantial influence on the overall safety of the bridge.

Load-bearing capacity for shear

In the same way as for the bending moment the safety margin for shear was reduced. The area of damage concentration is located in the area of the contact between the two parts of the bridge which were the last to be constructed. The initial capacity for the shear force was estimated for the non-cracked phase according to the expression given in EC2:

$$V_{Rd,c} = [(0.18/\gamma_c)\, k(100\rho_l f_{ck})^{0.333} + 0.15\sigma_{cp}]b_w d$$

With the assumption of the parameters taken from the bridge design, the value of:

$$V_{Rd,c} = 1265 \text{ kN}$$

is reached. This value is compared to the maximal shear force obtained from the static calculation, reduced in effect of prestressing force action:

$$V_{Ed} = 1430 \text{ kN} – 2480 \text{ kN} \cdot \sin 11.1° = 952 \text{ kN}$$

The supports' relative settlements are also included in this result. The above values are typical for a regular PC structure, where shear is not bringing any risk of collapse and even cracking in shear has a safety margin of 33%.

A lower value of the prestressing force results in both a reduction of the shear load-bearing capacity and an increase in the static force from loads:

$$V_{Rd,c} = 901 \text{ kN}$$

and

$$V_{Ed} = 1430 \text{ kN} - 2032 \text{ kN} \cdot \sin 11.1° = 1038 \text{ kN}$$

Shear force is 15.2% higher than the ultimate limit state load-bearing capacity for shear in the first phase. As a consequence of the lower prestressing force, shear may provoke cracks, although considering safety factors for loads and concrete strength concrete may resist the applied stress level. The remaining load-bearing capacity of the cross-section in phase II based mainly on the shear reinforcement is sufficiently high and reaches (with vertical stirrups composed of 6 bars of 16mm in the spacing of 12 cm) the level of:

$$V_{Rd,s} = 1430 \text{ kN}$$

Based on the evaluation results, it may be concluded that the shear force in cross-section is increased as an effect of lower prestressing force and on the other side, load-bearing capacity for shear is shifted from the first phase to the second phase (with cracks). This will have an significant influence on the durability of the member. In this area, an approach based on the durability model presented in [5] is included in the further plans of this analysis.

5.2. Analysis of the influence of damage on the load-bearing capacity of the structure

Regarding the location of the area subjected to damage as well as the type of the irregularities, it was recognised that they may negatively influence the load-bearing capacity of the beam under shear forces in particular. The lack of the cement grout in the cable ducts causes a radical decrease of the shear resistance evaluated in accordance with the present calculation methods. Moreover, the concrete cover splitted on the whole depth of the girder cannot be taken into consideration in the evaluation of its shear resistance.

The analysis in this scope was undertaken in agreement with the regulations of the Eurocode 2 [4] and was carried out for the cross-section situated directly at the interconnection of the bridge segments where the cable duct diameter is increased as a consequence of the size of the coupling anchorages. The compressive strength of concrete was assumed to be at its design value (ULS) as $f_{cd} = 28.6$ MPa and the mean stress provoked by prestress was calculated as $\sigma_{cp} = 5.75$ MPa. As a consequence of the detected lack of cement grout in the cable ducts, the width of the cross-section was reduced in accordance with the principles given in [4]. With the diameter of the coupling anchorages shield being 275 mm and the multiplication factor for the empty ducts at 1.2, the substitute width of the beam was reduced from 120 cm to only 21 cm. The reinforcement ratio of the longitudinal bars was estimated to

be at a level of 0.37%. With the mentioned assumptions, the resulting shear force resistance, related to the concrete cracking, reaches a value of $V_{Rd,c}$ = 337 kN, while the shear force obtained from the static calculation is V_{Ed} = 952kN. By comparison with the values estimated for the non-damaged cross-section, it can be concluded that the importance of cracks on the girder safety is no more questionable.

Moreover, the value of the principal tensile stress in the skew direction was estimated – this is related to the risk of the skew cracks. Local stress values were considered on the assumption that the whole cross-section weakened by the presence of voids is acting in the force transfer. The principal stress reaches 70% of the concrete tensile strength. This gives evidence of an increased risk of exceeding the concrete strength and evidence of the appearance or development of cracks in the case of the cumulative action of various simultaneous loads on the structure.

6. Conclusions

The structure subjected to the investigation is substantially weakened as an effect of the combination of several independent factors. A decrease of the prestressing force causes a substantial reduction of the safety margin. The observed instances of damage have further influence on the load-bearing capacity. The settlement of supports does not negatively affect the overall balance of the internal forces. The investigation of the structural consequences with regard to safety is separately carried out for various limit states. Estimation of the structural durability decrease which is an evident effect of the damages is an important subject worth of further analysis.

Strengthening of the structure is necessary as is the elimination of the potential dangers. Due to the complexity of the case, an advanced model of the structure must be built in order to perform a detailed analysis of the multiple influences. Such a model will allow the estimation of the real margin of safety in a much more precise manner than that which is provided by the grid model. The construction of such model is also in the further plans related to this case.

References

[1] Bruce S.M., McCarten P.S., Freitag S.A., Hasson L.M., *Deterioration of Prestressed, Concrete Bridge Beams*, Land Transport New Zealand Research Report 337, Wellington, New Zealand 2008.

[2] PN-91/S-10042 Obiekty mostowe. Konstrukcje betonowe, żelbetowe i sprężone. Projektowanie.

[3] Drobiec Ł., Jasiński R., Piekarczyk A., *Diagnostyka konstrukcji żelbetowych*, Tom 1, PWN, Warszawa 2015.

[4] EN 1992-2:2005 Design of concrete structures. Concrete bridges. Design and detailing rules.

[5] Destrebecq J.-F., Gwoździewicz P., Midro M., *Assesment of bridge structure durability – analysis and experimental verification*, Architecture Civil Engineering Environment, Vol. 1/2015, 69–75.

TECHNICAL TRANSACTIONS | CZASOPISMO TECHNICZNE
CIVIL ENGINEERING | BUDOWNICTWO
3-B/2015

WIT DERKOWSKI*, MATEUSZ SURMA*

COMPOSITE ACTION OF PRECAST HOLLOW CORE SLABS WITH STRUCTURAL TOPPING

ZESPOLENIE STRUNOBETONOWYCH PŁYT KANAŁOWYCH Z NADBETONEM

Abstract

There is no interface reinforcement in composite floors made of HC slabs covered with structural topping. In such structures, the preparation of the top surface of the precast element has a major influence on longitudinal shear strength. The recommendations of various codes concerning the bearing capacity of the non-reinforced joint in concrete composite structures are presented in this paper. The results of the authors' own computational analysis have been compared with the results of experimental tests carried out by different research institutions. Calculations according to Eurocode 2 underrate the value of the bearing capacity. A much stronger conformity of the results was achieved for the calculations carried out according to previously existing standards or according to information given in Model Code 2010.

Keywords: *composite action, composite structures, hollow core slab, longitudinal shear, structural topping*

Streszczenie

W stropach zespolonych, wykonywanych z płyt HC z nadbetonem konstrukcyjnym, nie stosuje się zbrojenia zszywającego w złączu. W tych konstrukcjach przygotowanie powierzchni górnej prefabrykatu ma zasadniczy wpływ na nośność styku na ścinanie. W artykule przedstawiono zlecenia różnych dokumentów normowych w zakresie nośności niezbrojonego złącza w betonowych konstrukcjach zespolonych. Wyniki własnych analiz obliczeniowych porównano z rezultatami badań doświadczalnych prowadzonych w różnych ośrodkach naukowych. Obliczenia według Eurokodu 2 dają zaniżone wartości nośności. Dużo lepszą zgodność obliczeń z wynikami badań uzyskuje się dla obliczeń prowadzonych według wcześniej obowiązujących przepisów lub informacji zawartych w Model Code 2010.

Słowa kluczowe: *konstrukcje zespolone, nadbeton konstrukcyjny, płyta kanałowa, ścinanie podłużne, zespolenie*

DOI: 10.4467/2353737XCT.15.159.4334

* Ph.D. Wit Derkowski, M.Sc. Mateusz Surma, Institute for Building Materials and Structures, Faculty of Civil Engineering, Cracow University of Technology.

1. Introduction

The casting of a structural layer of reinforced concrete topping on the surface of prestressed HC slabs is a structural procedure often applied in engineering practice. The positive influence of concrete topping on the ultimate and serviceability limit states of hollow core slabs might be significant if full monolithism is developed between the topping and the precast slabs. The presence of the concrete topping on the upper surface of slabs not only improves the load bearing capacity of the floor structure and allows for better cooperation between adjacent slabs (e.g. in the case of transmission of concentrated or linear loadings) but it also improves the diaphragm action of the floor. Topping reinforcement participates in the carrying of negative bending moments (either intentional or unintentional) in the supports zones. Since the concrete topping layer improves the dynamic characteristics of the structure, this type of structural solution is commonly used in countries where seismic loadings represent a threat to the safety of the precast structures.

Experimental research carried out in various scientific centres all over the world demonstrated that the concrete topping makes a major contribution in increasing the bending moment capacity of HC slabs (increase of approximately 25% [6, 11, 23]) and the shear capacity (in case of the bearing on the rigid supports, increase of approximately 35% [2, 22, 23]). The application of a concrete topping positively influences on the behaviour of the slabs in a serviceability limit state by increasing both the flexural stiffness of the floor and its cracking moment by approximately 15% [18]. This positive influence of structural topping application is apparent in the analysis of the fire resistance of HC slab floors [3] and in the improvement of the acoustic characteristics of these floors. Concrete topping is also one of the most preferable means of levelling the upper surface of floors constructed with precast elements which have different cambers due to prestressing.

It should be emphasised that the current HC slab production technologies (extrusion or slip-forming) do not allow for placing any transverse reinforcement in the cross-section of the slab, including the interface reinforcement. If the reinforcement crossing the interface between the topping and the precast element is necessary, it could be placed in the longitudinal joints between adjacent precast HC elements during the floor execution stage.

The concrete topping is most frequently implemented as a layer not thinner than 40 mm (usually 40–80 mm) with anti-shrinkage mesh reinforcement. Considering fire safety of HC slabs, it is advised that the thickness of the concrete topping in the mid-span should not exceed 50 mm, and the reinforcement of the topping layer in the support zone should not be greater than ø 6 mm every 150 mm in the longitudinal direction of the slab [15]. It is recommended that the concrete class of this layer should not be lower than C20/25.

The analysis of the bearing capacity of the interface between the concrete topping and the precast element under longitudinal shear in the aspect of design guidelines and international experimental research is considered in this paper. In actuality, this is a very complex problem, since on the behaviour of this interface influence not only the magnitude and type of both direct actions (for example operational load) and indirect actions (for example shrinkage and creep of concrete), but also number of the factors connected with the execution of the structure (for example the material characteristics of concrete, shaping of the joint interface, its moistening, contamination, possible cracking, presence of laitance etc.) Factors having an effect on the quality of HC slabs with topping composite action are graphically presented in Fig. 1 [6].

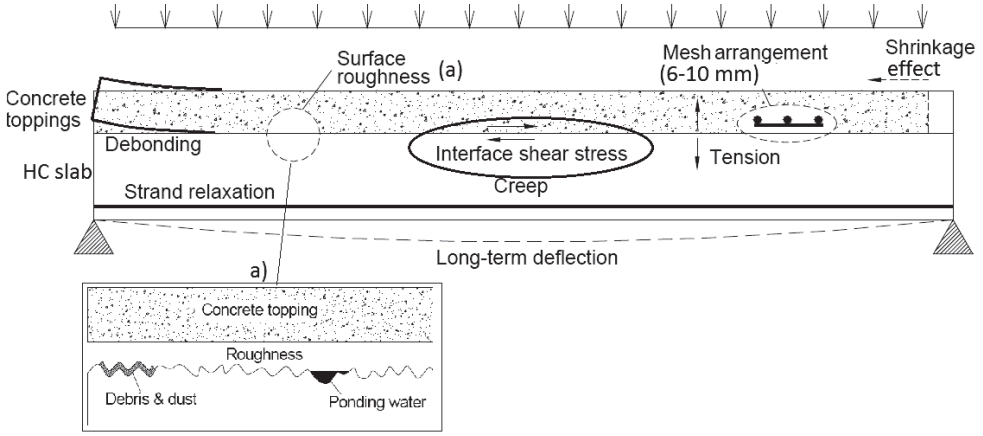

Fig. 1. Factors influencing the composite action of the HC slab with topping [6]

Effectiveness of the adhesive bond forces between the precast element and an in-situ concrete topping depends also from the preparation of the surface of the precast element and the degree of filling of the roughness of the old concrete with the grout of the new concrete mix.

The basic parameter which characterises the surface of the precast element is the average roughness R_a – this represents the medium deviation of the surface profile from the medium line (Fig. 2).

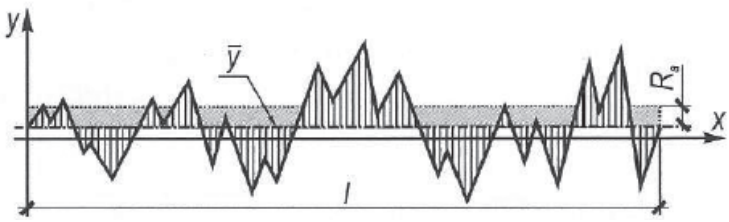

Fig. 2. Definition of the average roughness

In particular code regulations, the roughness of the precast element is defined in different ways. In [10] the classification due to the roughness measured by means of the engineering method (a sand patch method), easily applicable in the building site conditions, has been assumed. Four categories are distinguished:

– very smooth – for a non-measurable R_t;
– smooth – for $R_t < 1.5$ mm;
– rough – for $1{,}5 \text{ mm} \leq R_t < 3.0$ mm;
– very rough – for $R_t \geq 3.0$ mm.

In EN 1992-1-1 [10], which will henceforth be referred to as EC2, and in many other codes (for example PN-B-03264 [20]), four different types of surface have been introduced.

These are defined by means of the type of the technological procedures applied at the stage of precast element execution:

- very smooth surface – obtained in steel moulds, plastic moulds or especially prepared wooden moulds;
- smooth surface – a slip-formed or extruded surface, or a free surface left without further treatment after vibration;
- rough surface – surfaces having at least 3 mm of unevenness at a spacing of about 40 mm, obtained by raking and aggregate exposure;
- indented.

Execution mistakes at the stage of the production, i.e. inappropriate methods of obtaining the rough surface of the precast element, might cause the formation of micro-damage to this surface and contribute to a reduction of the bearing capacity of the joint. Contaminations of the joint surface such as air bubbles and water puddles resulting from the improper moistening of the precast element surface or the segregation of the concrete topping grout may lead to a significant decrease in adhesion [6]. Sawdust, hydraulic oil, dirt and construction debris must be cleaned off prior to casting the topping [17]. In practice, the methods of casting and compacting the topping layer of the concrete and further maintenance are of major importance, together with the atmospheric conditions during each of these procedures. Research [5] has shown that the proper compacting of the topping concrete layer (using a vibrator) can increase the joint strength by up to 100% higher than in the case of poor compaction (for example, with use of a steel rod). The influence of all those execution aspects of concrete topping casting, on the later behaviour of the whole structure, is very often underrated by the designers and contractors.

2. Analytical model of composite action

In composite structures consisting of two different concretes which were cast at different times, with no existing transverse reinforcement crossing the interface, the proper work of the structure is possible only as a result of the occurrence of the bonding forces between the two elements. These forces arise from physicochemical phenomena, i.e. adhesive bond and friction at the contact surface.

Adhesion is characterised by the properties of combined materials. At the time of the setting of topping concrete, chemical reaction between the components of the fresh cement grout and the anhydrated cement particles in the precast element occur [13]. Penetration of the new concrete mix into local unevenness of the precast element surface results in the occurrence of the mechanical bond in the form of aggregate interlock mechanism [24].

The occurrence of external stresses perpendicular to the joint interface and pressing adjacent surfaces, σ_N, is connected with the occurrence of the friction force in the interface surface, the magnitude of which depends on the friction coefficient μ.

In the classical model of contact surface behaviour used to determine of the interface shear strength $\tau_{Rd,j}$ under the stresses σ_N, the Coulomb hypothesis is adjusted as a basis for the majority of standardised methods. This hypothesis assumes that the bearing capacity of the joint depends on so-called coherence (being the function of adhesion factor c and tensile strength of the weaker concrete f_{ctd}) and friction, characterised by the coefficient μ:

$$\tau_{Rd.j} = c \cdot f_{ctd} + \mu\sigma_n \leq 0.5 \cdot \nu \cdot f_{cd} \quad (1)$$

where:

f_{cd} – is the design compress strength of the concrete,
f_{ctd} – is the design tensile strength of the concrete.

The expression given in the standards describing tangent shear stresses at the interface of the composite elements is determined according to the basic rules of the strength of the materials proportional to the shear force. These stresses can be calculated from the expression:

$$\tau_{Ed} = \frac{\beta \cdot V_{Ed}}{z \cdot b} \quad (2)$$

where:

β – is the ratio of the longitudinal force in the topping area and the total longitudinal force in the compression zone, calculated for the section considered;
z – is the lever arm of the composite cross-section (usually assumed as $z = 0.8d$, where d is the effective height of the cross-section);
b – the width of the interface;
V_{Ed} – design shear force.

When calculating the bending strength of the joint in composite structures, the interface itself is usually treated as being only under shear action – this is apparent in the construction of the code formulas, including only tangent stresses from external loadings However, if we assume that the interface is parallel to the longitudinal axis of the element and analyse the trajectory of the principal stresses, it can be proved that the interface is also under the action of normal stresses. Magnitude and notation of those stresses depend not only on the position of the analysed cross-section at the length of the element, but also on the position of the interface along the height of the cross-section.

European standard EN 1168+A3:2011 [7], concerning precast hollow core floor slabs, assumes the possibility of the occurrence of two models of failure of the composite cross-section as a result of exceeding tensile strength for the following shear actions:

- type a) – shear failure of the concrete webs as a result of principal tensile stresses;
- type b) – shearing off of the topping layer as a result of interface shear capacity excess.

In the case of structural failure as a result of type b) longitudinal shear, code [7] recommends the application of the procedure given in EC2 [8]. The longitudinal shear resistance of the composite elements, constructed from precast element and an in-situ topping layer without transverse reinforcement, consist of bond between composite elements concretes and friction between elements and presence of interface reinforcement (if any). Interface surface characteristics are described by the following parameters: c – adhesive coefficient and μ – friction coefficient.

In the currently withdrawn polish standard PN-B:03264:2002 [20], similar to many others codes and recommendations previously applied in European countries (e.g. ***fib*** Bulletin 6 [9], published in 1995), the method of the determination of the interface longitudinal shear capacity was analogical to EC2, except from slightly higher values of coefficient c. ***fib*** recommendations [9] additionally indicated the necessity of including in calculations of

longitudinal tangent stresses at the interface τ_{Ed} –the additional component of those stresses, connected with placing reinforcement in filled cores of the support zone of HC slab.

The values of coefficients *c* and μ suggested by [7–9] and [20] are compiled in the Table 1.

Table 1

Values of *c* and μ coefficients

Roughness	Adhesive coefficient *c*		Coefficient of friction μ	
	Eurocode 2 EN 1168	***fib*** Bulletin 6 PN-B 03264	Eurocode 2 EN 1168	***fib*** Bulletin 6 PN-B 03264
Very smooth	0.025÷0.1	0.02	0.5	0.5
Smooth	0.2	0.35	0.6	0.6
Rough	0.4	0.45	0.7	0.7
Indented	0.5	0.50	0.9	0.9

Chapter 7 (section 7.3.3.6) of Model Code 2010 [10], which is dedicated to structural designing, presents exactly the same calculation algorithm as EC2 for the interface between two concretes without crossing reinforcement. However, section 6.4.3 of this same document, which discusses issues of modelling and the designing of the bond between the two concretes, gives different, more accurate information resulting from experimental studies. The ultimate capacity of the interface under shear forces is defined there as the sum of the adhesion effect with the interlock mechanism, friction under shear forces and dowel action of the transverse reinforcement crossing the interface:

$$\tau_u = \tau_a + \mu\left(\rho \cdot \kappa_1 \cdot f_y + \sigma_n\right) + \kappa_2 \cdot \rho \cdot \sqrt{f_y \cdot f_{cc}} \le \beta_c \cdot \nu \cdot f_{cc} \tag{3}$$

where τ_a is the strength due to the adhesion and mechanical interlock.

For the joint without reinforcement or with a small amount of reinforcement ($\rho < 0.05\%$), it can be assumed that: $\tau_u = \tau_a$.

The medium values of adhesive bond stress τ_a and friction coefficient μ, given in MC2010, were assumed on the basis of the research by Randl [21] – see Table 2. Those values were determined for the adequately prepared joint for concrete C50/60 and C20/25.

Table 2

Values of τ_a and μ coefficients, according to MC2010 [10]

Roughness	Adhesive bond stress τ_a	Coefficient of friction μ
Smooth	(0.5–1.5)*	0.5–0.7
Rough	~1.5–2.5	0.7–1.0
Very rough	~2.5–3.5	1.0–1.4

* values not given in [10], but suggested by [21].

In the further part of this article, information abbreviated as MC2010 will concern the model given in clause 6.4.3.

Since in [10], following [21], only medium values of shear strength for individual surface roughness were given; for the purposes of the calculation of the composite element limit strength, it seems essential to determine the design values for the suggested adhesive bond strength. This can be calculated according to the following expression:

$$\tau_{Rd.d} = \frac{1}{\gamma_c}\tau_{a.m} \cdot \frac{f_{ctk0.05}}{f_{ctm}} \tag{4}$$

and for each rage of adhesive bond stress, the following results were obtained:
- for smooth surface – 0.23–0.70 MPa;
- for rough surface – 0.70–1.15 MPa;
- for rough surface – 1.15–1.60 MPa.

In American standard ACI 318M-11 [1], two methods for determining of the interface capacity of the composite are presented. According to method A, the values of the horizontal shear force V_u and shear horizontal strength V_{nh} should be compared. The expression allowing the determination of the value V_{nh} is the function of the width of joint b_v and the effective height of the cross-section, for a non-reinforced clear surface joint, roughened and free from cement wash. If the surface was not intentionally roughened, but minimal crossing reinforcement was applied, then $V_{nh} = øb_v d$ [kN]. The interface capacity condition could be written as follows:

$$\varphi V_{nh} \geq V_u$$

where φ is the safety coefficient for strength calculations, equal to 0.85.

According to method B, horizontal shear force can be calculated as the difference between horizontal compressing and tensile forces in individual cross-section segments. In this case, the bearing capacity of the joint is calculated at the surface of joint $b_v \cdot l_v$, where l_v is the length of the shear cross-section. Method B assumes a limitation of the maximum interfacial shear stress, to a value not exceeding 0.55 MPa (design value).

When applying approach [1] to method B, higher horizontal shear strength results are obtained compared to method A due to the averaging of horizontal shear stress. Another difference between these two methods is the use of the depth parameter d in method A – this is a simplification of the lever arm between the tensile and compressive cross-section forces, which can be stated more formally as $(d - a/2)$, where a is the depth of the compressive stress block.

3. Research on the interface shear

The experimental tests carried out in Poland by A. Ajdukiewicz et al. [2] were developed in order to clarify the actual behaviour of slabs with an in-situ concrete topping layer without interface reinforcement. The interaction of the topping was very satisfactory, up to level of

over 95% load at failure. The results of the experiment showed that in the case of a well-developed interface surface, shear resistance at the interface is much higher in comparison to the idealised shear resistance calculated according to [7] or [8]. This proves that rules given in these codes may be omitted in practical situations, because the value of the surface factors c and μ may be considered to be too conservative.

M. Gohnert [12] studied the influence of technological aspects on the longitudinal shear strength of the interface. As tests results for beams with topping under flexure showed, a poor correlation exists between the horizontal shear strength and the compressive strength of the concrete. It is therefore not advisable to specify the horizontal shear strength as a function of the concrete compressive strength. However, the regression analysis does indicate an upward trend in shear capacity as the concrete strength is increased. Although the influence of the concrete strength may be less apparent than other factors, the compressive strength does influence the shear strength; therefore, at least a minimum compressive strength should be specified.

Specifying a roughness only by stating the instrument used to create the undulations is not sufficient; an actual measurement of roughness should be specified. A brush or rake can produce a vast range of roughness values depending on the stiffness of the instrument, the amount of pressure applied and the viscosity or age of the mix. A significant increase in the shear capacity as a function of the roughness is shown in [12].

The latest American research focused on the interfacial shear strength between HC slabs and the topping layer with the units fabricated using different typical producer practices [16]. Twenty-four push-off specimens with varying base block surface conditions fabricated using dry-mix (extruder procedure) and wet-mix (slip-former procedure) were tested. The precast slabs were fabricated with different surface conditions to determine the influence of surface roughness on interface shear strength. Elements with machine finished, longitudinally raked, longitudinally/transversely broomed or sandblasted and top surfaces were prepared. In some specimens, a non-shrink sand-cement grout, with a thickness of approximately 1.5 mm was applied to simulate the work of slabs with the presence of laitance.

According to Mones and Brena [17], the interfacial shear stress limit of 0.55 MPa specified in [1] for intentionally roughened surfaces is conservative for all surface conditions tested including machine-finished specimens. Test result show that higher shear strengths of unreinforced composite interfaces can be obtained by roughening the hardened surface. For dry-mix HC slabs, a strong positive linear correlation was observed between surface roughness and interfacial shear strength and horizontal slip capacity. The interfacial shear strength of wet-mix HC units was related to both surface roughness and the presence of laitance. Roughened interfaces developed a higher strength and horizontal slip capacity than machine-finished interfaces. Sandblasting removed the laitance layer from the wet-mix HC slabs and improved interfacial shear strength by providing a higher quality cohesive bond and, to a lesser extent, by increasing the surface roughness. Grout generally did not impair the interfacial shear strength of dry-mix and wet-mix HC slabs surfaces. In fact, grouted dry-mix specimens had significantly higher interfacial shear strength and horizontal slip capacity than companion specimens that were not grouted. The results for grouted wet-mix specimens are not so clear, but it has been shown that, in general, the grout layer does not impair the join work.

Based on the results of the experimental push-off type tests, carried out by Moenes [16], the authors of this paper calculated the values of the shear stresses τ_{Ed}. Taking into account the

knowledge concerning the concrete topping strength, it was possible to determine adhesion coefficient *c*. The results of these calculations are presented in Table 3. Because for each type of surface only two computational results were available, for the purpose of further analysis, the smaller from obtained results was applied. The minimal value of the coefficient *c* was compared with the values of adhesion coefficients recommended by codes [8] and [20], and the minimal value of shear stress was compared with the recommendations of [1] and [10] – see Table 4.

Table 3

Characteristic interface strength parameters, determined on the basis of researches [16]

Specimen	Surface condition	Max. force F_{test} [kN]	Shear stress τ_{Ed} [MPa]	Topping tensile strength f_{ctm} [MPa]	Adhesion coefficient c_{test} [–]	Mean value of adhesion coefficient $c_{test.m}$ [–]
DRY-MFX-1	Machine finished	206.8	**1.45**	2.9	**0.50**	0.46
DRY-MFX-2		152.1	**1.06**	2.5	**0.42**	
DRY-SBX-1	Sandblasted	161.9	**1.13**	2.9	**0.39**	0.44
DRY-SBX-1		215.3	**1.50**	3.1	**0.48**	
DRY-LRX-1	longitudinally raked	223.3	**1.56**	2.9	**0.54**	0.50
DRY-LRX-2		205.1	**1.43**	3.1	**0.46**	
DRY-TBX-1	Transversely broomed	287.8	**2.01**	3.1	**0.65**	0.65
DRY-TBX-2		319.4	**2.23**	3.4	**0.66**	
DRY-MFG-1	Machine finished, grouted	275.8	**1.93**	2.9	**0.66**	0.76
DRY-MFG-2		377.2	**2.63**	3.1	**0.85**	
DRY-LRG-1	Longitudinally raked, grouted	276.7	**1.93**	3.1	**0.62**	0.61
DRY-LRG-2		266.0	**1.86**	3.1	**0.60**	
WET-MFX-1	Machine finished	198.4	**1.38**	3.1	**0.45**	0.37
WET-MFX-2		127.7	**0.89**	3.1	**0.29**	
WET-SBX-1	Sandblasted	267.8	**1.87**	3.0	**0.62**	0.57
WET-SBX-2		225.1	**1.57**	3.1	**0.51**	
WET-LBX-1	longitudinally broomed	222.0	**1.55**	3.1	**0.50**	0.42
WET-LBX-2		144.1	**1.01**	2.9	**0.35**	
WET-TBX-1	Transversely broomed	257.5	**1.80**	2.9	**0.62**	0.57
WET-TBX-2		247.8	**1.73**	3.3	**0.52**	
WET-MFG-1	Machine finished, grouted	157.5	**1.10**	2.9	**0.38**	0.39
WET-MFG-2		165.5	**1.15**	2.9	**0.40**	
WET-LBG-1	Longitudinally broomed, grouted	247.3	**1.73**	2.7	**0.64**	0.61
WET-LBG-2		218.4	**1.52**	2.6	**0.59**	

As conducted analyzes demonstrate, the interface strength parameters determined for the test results presented in master thesis [16] are in each case significantly higher than their equivalents given in codes or standards. The adhesion coefficient for the smooth surface given in [8], as well as the shear stress given in [1], are at least twice as small as those obtained in the tests. Fairly strong correlations (while maintaining of all safety reserves) are obtained for the parameters c and μ taken from previously obligatory codes (e.g. in [20] or [21]), as well as using the information from Chapter 6 of Model Code 2010 [10].

Table 4

Comparison of the research results with calculation results

Surface condition	Min. value of adhesion coefficient obtained in tests $c_{test.m}$ [–]	Adhesion coefficient given in [8] c [–]	Adhesion coefficient given in [20] c [–]	Min. value of shear stress obtained in tests τ_{Ed} [MPa]	Shear stress given in [1] τ_{Rd} [MPa]	Design shear stress for [10] $\tau_{Rd.d}$ [MPa]
DRY-MFX	**0.42**	0.2	0.35	**1.06**	0.55	0.23–0.70
DRY-SBX	**0.39**	0.2	0.35	**1.13**		0.70–1.15
DRY-LRX	**0.46**	0.4	0.45	**1.43**		~1.15
DRY-TBX	**0.65**	0.4	0.45	**2.01**		~1.15
DRY-MFG	**0.66**	0.2	0.35	**1.93**		0.23–0.70
DRY-LRG	**0.60**	0.4	0.45	**1.86**		~1.15
WET-MFX	**0.29**	0.2	0.35	**0.89**		0.23–0.70
WET-SBX	**0.51**	0.2	0.35	**1.57**		0.70–1.15
WET-LBX	**0.35**	0.4	0.45	**1.01**		~1.15
WET-TBX	**0.52**	0.4	0.45	**1.73**		~1.15
WET-MFG	**0.38**	0.2	0.35	**1.10**		0.23–0.70
WET-LBG	**0.59**	0.4	0.45	**1.52**		~1.15

4. Calculation example – comparison of design standards

To present the differences arousing from application of the different codes, concerning longitudinal interface shear capacity of the hollow core slab with concrete topping, computational example has been conducted. For the calculations, a prestressed HC slab with a height of 500 mm and made of C50/60 concrete was assumed. The concrete topping with a height of 60 mm and made of C20/25 class concrete was layered on the upper surface of the slab. It was also assumed that the slab is simply supported and uniformly loaded with the self-weight g_d = 6 kN/m^2, an additional static load Δg_d = 1 kN/m^2 and a service load of a variable value.

In order to determine the coefficient of compressive stress distribution carried by the topping concrete and slab (coefficient β), detailed analyses of the diagram of stresses along the height of the cross-section were carried out. Stresses due to self-weight, prestressing, additional loads and service loads at the appropriate levels were calculated. Additionally, stresses from the shrinkage difference for two different materials (topping and slab concrete) were determined. The distribution of stresses in the composite cross-section is presented at the schematic diagram below (Fig. 3).

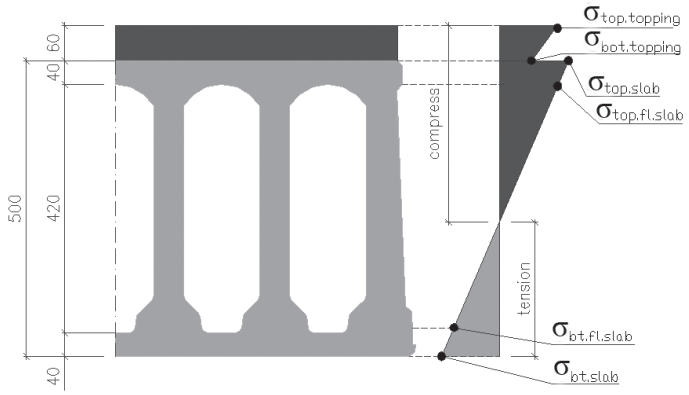

Fig. 3. Concrete stress distribution on the height of the composite cross-section

Initial calculations concerned the determination of the longitudinal shear strength, making allowance for those types and characteristics of surface preparation, which are used for hollow core slabs – i.e. smooth and rough surface according [8] or [20]; rough or very rough surface according to [10] and rough surface according [1]. The results of this analysis at the adopted level of service loading q_d = 5 kN/m^2 are presented in Table 5. Table 6 presents the values of longitudinal shear stresses that would possibly appear in the joint of the analysed floor with a span length variable in the range from 14 m to 20 m.

Table 5

Comparision of interfacial shear strength calculated for different codes

v_{Rd} [kPa]							
EC 2 EN 1168		***fib*** Bul. 6 PN-B 03264		MC2010		ACI 318M-11	
smooth $cf_{ctd} + \mu\sigma_n$	290 + 6 = **296**	smooth $cf_{ctd} + \mu\sigma_n$	508 + 6 = **514**	smooth rough	**230-700 700-1150**	clean, free of laitance and intentationally roughened	**550**
rough $cf_{ctd} + \mu\sigma_n$	580 + 8 = **588**	rough $cf_{ctd} + \mu\sigma_n$	652 + 8 = **660**	rough very rough	**700-1150 1150-1600**		

As the calculation results demonstrate, the smallest interface shear strength values were definitely obtained when applying design procedures recommended by EC2 (and therefore recommended by code EN 1168, which in this range has a direct reference to EC2). Limitation of the shear stresses, given in ACI-318M [1], is convergent with recommendations of previously obligatory standards for smooth surfaces but when concerning the surfaces regarded in Europe as rough, this limitation should be treated with greater caution. It should be noted that the PCI Design Handbook [19] states that experience and testing indicate that normal finishing methods used for precast concrete surfaces (in Europe considered as a smooth surfaces) may be treated as intentionally roughened. Given in Chapter 6 of the latest version of Model Code [10] interface shear strength magnitudes, result in the highest values, even when taking into consideration only the lower limits of the recommended ranges.

Table 6

Interfacial shear stress for different span length of the slab

	L = 14 m	L = 16 m	L = 18 m	L = 20 m
v_{Ed}	81 kPa	99 kPa	117 kPa	135 kPa

It should also be pointed out that the contribution of friction forces in the interface shear strength is very small for floor structures. The magnitude of the component connected with friction $\mu\sigma_n$ depends on the level of service loading. However, even for extreme levels of loading, the component itself, when analysing composite floors, remains at a negligible level of 1–4% for smooth surfaces and 1–2% for rough surfaces. In Table 7, the values obtained for the analysed floor with a 16 m span and service loading in the range of 3.5 kN/m^2 to 10.0 kN/m^2 are presented.

Table 7

Interfacial shear strength obtained for different live loads

		EC2	***fib*** Bul. 6	EC2	***fib*** Bul. 6	EC2	***fib*** Bul. 6	EC2	***fib*** Bul. 6
Live load q [kN/m^2]		3.5		5.0		7.5		10.0	
smooth	cf_{ctd} [kPa]	290	508	290	508	290	508	290	508
	$\mu\sigma_n$ [kPa]	5.2		6.5		8.8		11.0	
	$\mu\sigma_n/cf_{ctd} + \mu\sigma_n$	**2%**	**1%**	**2%**	**1%**	**3%**	**2%**	**4%**	**2%**
rough	cf_{ctd} [kPa]	580	652	580	652	580	652	580	652
	$\mu\sigma_n$ [kPa]	6.0		7.6		10.2		12.9	
	$\mu\sigma_n/cf_{ctd} + \mu\sigma_n$	**1%**	**1%**	**1%**	**1%**	**2%**	**2%**	**2%**	**2%**

For the emphasizing deserves also the fact, that obtained design bearing capacity values of non-reinforced interface of HC slab and concrete topping – even in case of application of the most strict recommendations given in standards or codes – provides much higher values than possible stresses obtained for typical uniformly loaded floor structures. The problem with the bearing capacity of the interface between the precast slab and the concrete topping might possibly occur only in situations in which high values of concentrated or linear loadings would generate high magnitudes of transverse forces.

5. Conclusions

Each year in Europe, more than 20 million square meters of prestressed precast hollow core slabs are being produced. Very often, directly on the upper surface of the precast element, the layer of structural concrete topping is cast in order to improve the performance of the floor structure. Commonly used technologies of HC floor element production disable the possibility of the application any kind of transverse reinforcement. For that reason, the interface between the slab and the concrete topping in most cases remains non-reinforced. In these situations, the quality of the upper surface of the precast HC element (both its formation during the production process and the preparation of the surface prior to casting the topping) has a significant influence upon the interface capacity.

In this paper, different recommendations of various standards and codes have been presented (EC2, EN 1168, ***fib*** Bulletin 6, PN-B-03264, Model Code 2010, ACI-318M) concerning the scope of the bearing capacity of concrete composite structures without interface reinforcement. Comparisons of these guidelines were conducted on the basis of computational examples, where for individual standards, different results of interface shear capacity were obtained. For a better recognition of the problem, the results of the experimental research carried out by other scientists (especially by Mones [16]), giving considerations for different ways of forming the upper surface of the HC slabs, were analysed. It was demonstrated that calculations according to the current obligatory European codes ([7, 8]) provided the lowest possible values of joint bearing capacity, these were far smaller than the values obtained in the experiments. Similar conclusions were drawn in other, earlier pieces of research (e.g. [2]). The analysis of the existing databases, covering the results of experimental research of the composite concrete beams, revealed that the values of ultimate loads obtained on the experimental path are 3–11 times bigger than the values calculated according to the procedures presented in [8]. For the monolithic elements, the ratio of the experimental to calculated failure loads remained within the range of 1 to 3 [14]. The introduction of the decreased values of coefficients c and μ (characterising the composite joint) during the changes to the European standards and codes taking place at the beginning of the century was not justified. The values of those coefficient in previously regulations (e.g. [9] and [20]) give the interface strength values closer to the real interface capacity. The recently published Model Code 2010 [10] introduced changes to both the classification and the characteristics of individual types of interface, as well as in the procedure of calculation of the longitudinal shear capacity given in Chapter 6. It appears that the mean values of the adhesive bond stresses suggested

in [10] allow for a good representation of the actual performance of those types of joints. In this paper, the procedure of transition from medium values of adhesive bond stresses to design values of those stresses, that could be applied in the structural design, has been presented.

Analyses carried out by the authors demonstrated that in the case of ceiling or roof slabs, the participation of the friction effect in joint longitudinal shear capacity is negligible and can be omitted in calculations.

References

[1] ACI 318M-11, Building Code Requirements for Structural Concrete and Comentary, American Concrete Institute, USA 2011.

[2] Ajdukiewicz A. et al., *Experimental study on effectiveness of interaction between pretensioned hollow core slabs and concrete topping*, ACCE, No. 1, 2008.

[3] Derkowski W., Kreska M., *Fire resistance of prestressed hollow core slabs*, Proc. of KS2015 Conference, Kraków 2015 (in Polish).

[4] Derkowski W., Surma M., *Composite action in prestressed rib and beam floor systems without transverse reinforcement*, Materiały Budowlane 11/2011, 1–6 (in Polish).

[5] Djazmati B., Pincheira J.A., *Shear stiffness and strength of horizontal construction joints*, ACI Structural Journal, Vol. 101, 2004.

[6] Elliot K.S. et al., *Bending capacity of precast prestressed hollow core slabs with concrete topping*, Malaysian Journal of Civil Engineering, Vol. 20, No. 6, 2008.

[7] EN 1168:2005+A3:2011 Precast concrete products – Hollow core slabs, 2011.

[8] EN 1992-1-1:2008 Eurokod 2: Design of concrete structures – Part 1-1: General rules and rules for buildings, 2008.

[9] ***fib*** Bulletin 6, Special design considerations for precast prestressed hollow core floors, ***fib***, Lausanne, Switzerland 2000.

[10] ***fib*** Bulletin 65, Model Code for Concrete Structures 2010, ***fib***, Lausanne, Switzerland 2012.

[11] Girhammar U.A., Pajari M., *Tests and analysis on shear strength of composite slabs of hollow core units and concrete topping*, Malaysian JCE, Vol. 22, 2008.

[12] Gohnert M., *Horizontal shear transfer across a roughened surface*, Cement & Concrete Composites, Vol. 25, 2003.

[13] Halicka A., *Study of stress and strain in contact plane and support zone of composite elements involving the shrinkage and expansive concrete*, Wydawnictwa Uczelniane, Lublin 2007 (in Polish).

[14] Hegger J., Görtz S., *Nachträglich ergänzte Querschnitt mit horizontal Fuge nach DIN 1045-1*, Beton- und Stahlbetonbau 98, Heft 5, 2003.

[15] Jansze W. et al., *Structural behavior of prestressed concrete hollow core floors exposed to fire*, BIBM, 2014.

[16] Mones R.R., *Interfacial strength between prestressed hollow core slabs and cast-in-place concrete toppings*, Masters of Science in Civil Engineering, 2012.

[17] Mones R.R., Brena S.F., *Autors' response to discussion on hollow-core slabs with cast-in-place concrete toppings*, PCI Journal, Vol. 59, No. 1, 2014.
[18] Pajari M., *Shear capacity of hollow core slabs on flexible supports*, VTT Research Notes 1587, Espoo 1994.
[19] PCI Design Handbook, Precast and Prestressed Concrete, USA, 2004 Stitmann A., Ueda T., Shear-strength of precast prestressed hollow core slabs with concrete topping, ACI Structural Journal, Vol. 88, No. 4, 1991.
[20] PN-B-03264:2002 Konstrukcje betonowe, żelbetowe i sprężone. Obliczenia statyczne i projektowanie, PKN, Warszawa 2002.
[21] Randl N., *Design recommendations for interface shear transfer in **fib** Model Code 2010*, Structural Concrete 14, 2013, No. 3, 230–241.
[22] Scott N.L., *Performance of precast prestressed hollow core slab with composite concrete topping*, PCI Journal, No. 2, 1973.
[23] Stitmann A., Ueda T., *Shear-strength of precast prestressed hollow core slabs with concrete topping*, ACI Structural Journal, Vol. 88, No. 4, 1991.
[24] Walraven J.C., Mercx, W., *The bearing capacity of prestressed hollow core*, Research Raport, Delft 1983.

TECHNICAL TRANSACTIONS | CZASOPISMO TECHNICZNE
CIVIL ENGINEERING | BUDOWNICTWO
3-B/2015

WIT DERKOWSKI*, MATEUSZ SURMA*

TORSION OF PRECAST HOLLOW CORE SLABS

SKRĘCANIE PREFABRYKOWANYCH PŁYT KANAŁOWYCH

Abstract

Pretensioned hollow core slabs are one of the most widely applied precast elements in the modern building industry all over the world. Due to the possibility of their use under various support or loading conditions, these elements repeatedly work under a complex stress state. Theoretical analysis of the phenomena of the interaction of shear and torsion in the above-mentioned HC elements is presented. The theoretical basis and design regulations of the computational model included in code PN-EN 1168+A3:2011 along with parametrical analysis of that model are demonstrated. The largest experimental research program of hollow-core slabs under shear and torsion conducted thus far is also briefly described – this study was carried out in Finland in 2004 and was the basis for the development and calibration of the numerical computational model formulated in Chalmers University of Technology in Göteborg, Sweden.

Keywords: *hollow core slab, prefabrication, pretensioned element, shear, torsion*

Streszczenie

Strunobetonowe płyty kanałowe są jednym z najczęściej stosowanych stropowych elementów prefabrykowanych na świecie. Ze względu na możliwość funkcjonowania płyt w różnych warunkach podparcia czy obciążenia niejednokrotnie elementy te pracują w złożonym stanie naprężenia. W artykule przedstawiono analizę teoretyczną zjawiska interakcji skręcania ze ścinaniem poprzecznym w rozważanych elementach. Zaprezentowano podstawy teoretyczne i wytyczne projektowe modelu obliczeniowego zawartego w normie PN-EN 1168+A3:2011 wraz z analizą parametryczną modelu. Skrótowo opisano również największe dotychczas zrealizowane badania doświadczalne ścinanych i skręcanych płyt, zrealizowane w 2004 roku w Finlandii, które posłużyły do opracowania i kalibracji numerycznego modelu obliczeniowego wykonanego w Chalmers University of Technology w Göteborgu.

Słowa kluczowe: *płyty kanałowe, prefabrykaty, skręcanie, strunobeton, ścinanie*

DOI: 10.4467/2353737XCT.15.160.4335

* Ph.D. Wit Derkowski, M.Sc. Mateusz Surma, Institute for Building Materials and Structures, Faculty of Civil Engineering, Cracow University of Technology.

1. Introduction

Pretensioned hollow core slabs are most often designed as simply supported elements, and the computational analysis of such designs are based on the assumption of plane stress state. In most cases, it is assumed that the floor slabs are under the action of loading which is uniformly distributed over the whole surface of the slab. Hollow-core slabs, although constructed from precast elements, might be treated as floor plate with the possibility of the redistribution of loads to the adjacent precast elements. Such a performance by the floor is possibly due to monolithisation of the structure by casting the concrete in longitudinal joints between slabs or (in many structures) by casting the structural concrete topping layer [4].

The assumption of the plane stress state in the cross-section of the slab is justified when the element is subjected to uniformly distributed loading over its entire surface and supported on two parallel, relatively rigid supports, e.g. walls or beams with a large cross-section. In many cases, this assumption does not reflect the actual conditions of work and behaviour of the element. If only one of the elements of the floor structure is supported or loaded in a non-uniform way, then the distribution of the transverse force through the joint of the slabs may cause torsion of the adjacent slabs. The following slabs are examples of the occurrence and influence of torsional moments [1]:

a) elements supported on three edges, e.g. corner slab, with longer edge supported on the wall (see Fig. 1, detail: 1);
b) elements loaded with concentrated force in the longitudinal edge area, e.g. force from the trimmer beam acting as support for the neighbouring beam in the area of the large opening or recess cut for the purposes of staircases (see Fig. 1, detail: 2);
c) elements supported with one corner on the column (see Fig. 1, detail: 3);
d) slanted slabs in the support area, causing the lack of parallelism of the opposite supports (see Fig. 1, detail: 4);
e) elements supported on relatively slender beams, i.e. slim floor type [5].

The necessity to guarantee the safety of the HC slabs, which are widely applied in the modern building industry all over the world, brings an urgent need for the detailed analysis of the behaviour of these elements, including the influence of torsion, and the application of suitable design procedures.

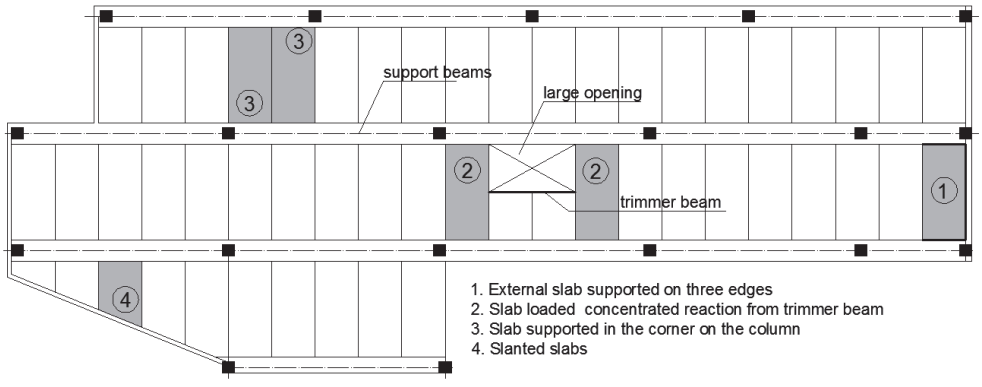

Fig. 1. Specific support and loading situations causing the torsion of the slab

2. Calculation of hollow core slabs under torsion and shear

Both transverse force V_{Ed}, and torsional moment T_{Ed}, occurring in the cross-section of the HC slab, generate tangent shear stresses. Tangent stresses τ_V, due to the transverse shear action, obtain the largest value at the level of the centroid of the cross-section and values of zero at the horizontal edges. In the so-called free, non-constrained shear, in case of full freedom of axial displacements, tangent stresses τ_T due to the torsional moment are distributed linearly along the width of the element, obtaining the highest value at the outline and a value of zero at the center line of the cross-section. The thinner the walls of the cross-section under torsion, the smaller its torsion resistance, thus at the relatively small values of the torsional moment T_{Ed} the maximum tangent stresses τ_T reach significant values.

In case of the constrained torsion, i.e. in the cross-sections where the interaction of the different internal forces appear (M_{Ed}, T_{Ed}, V_{Ed}, N_{Ed}), at the height of the cross-section develop additional tangent stresses, due to the transverse forces. These stresses are different from zero in the centre of the cross-section, but the strains they cause are negligibly small [10]. In the case of the assumption of torsion and shear interaction in the element with a non-solid cross-section (e.g. hollow core slab with empty cores, not filled with concrete), one outermost web is subjected to the combined action of the stresses $\tau_V + \tau_T$, the value of which is definitely higher than the stresses acting on the remaining webs (Fig. 2).

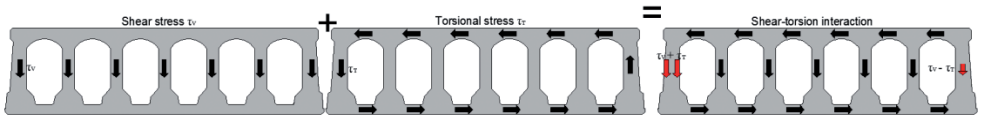

Fig. 2. Distribution of the tangent stresses in a cross-section of the hollow core element

A significant increase of the tangent stresses due to the interaction of shear and torsion may cause the value of the principal tensile stress σ_1 to overrun the tensile concrete strength. As a result, cracks start to form in the concrete, and they develop in the direction implicated by the trajectory of the principal tensile stresses. In calculations, it is assumed that in the areas subjected to major shear actions, the development of cracks on the vertical parts of the element (e.g. concrete webs of the slab) have a slanted course, and the angle of deviation from the longitudinal axis of the element remains in the range from 22° to 45°. With the effect of the additional torsion, the cracks may propagate helically at the level of the element surface at an angle of about 45°. The failure of the element without transverse reinforcement takes place at the moment of the occurrence of the first helical circumferential crack [9].

Based on the general assumptions of the concrete mechanics, both the values of the tangent stresses τ_V and τ_T, and the principal tensile stresses in the concrete σ_1 can be described with the following expressions (1)–(3):

$$\tau_V = \frac{V_{Ed} \cdot S_{cs}}{b_w \cdot I_{cs}} \tag{1}$$

$$\tau_T = \frac{T_{Ed}}{W_T} \tag{2}$$

$$\sigma_1 = \frac{\sigma_{cp}}{2} - \sqrt{\left(\frac{\sigma_{cp}}{2}\right)^2 + \tau^2} \le f_{ctd} \tag{3}$$

where:

- V_{Ed} – transverse force acting in the considered cross-section;
- T_{Ed} – torsional moment acting in the considered cross-section;
- S_{cs} – static moment of the part of the cross-section above the centroid horizontal axis of the cross-section;
- I_{cs} – moment of inertia of the cross-section;
- b_w – the sum of the widths of the webs at the level of the centroid of the cross-section;
- W_T – sectional modulus of the cross-section under torsion;
- σ_{cp} – the mean compressive stress, measured positive, in the concrete due to the design axial force (including the prestressing force) and bending moment;
- f_{ctd} – design tensile concrete strength, $f_{ctd} = f_{ctk}/\gamma_c$.

When analysing pretensioned hollow core slabs, the possibility of the occurrence of cracks due to simultaneous torsion and shear actions is a substantial problem because, for technological reasons, hollow-core slabs do not have transverse reinforcement. The shear resistance of such a slab, assuming the absence of cracks due to bending, is limited by the tensile strength of the concrete ribs. Slant crack forming in the webs propagate in the direction of top and bottom flanges. The failure usually appears in the support zone, where the full transmission length has not been reached, and the value of the prestressing force remains incomplete. Introducing the compressive force from prestressing into the cross-section causes the natural increase of crack resistance of the concrete element subjected to shear and torsion. It is the effect of the two-axial state of stresses resulting from shear and eccentric compression, delaying the forming of the cracks [9].

The lowest value of the pure shear resistance usually appears at the level of the smallest width of the web, i.e. in the half-height of the cross-section. The general condition of the shear strength for pretensioned hollow-core slabs is described by analogical expressions included in EN 1168+A3:2011 [6], Model Code 2010 [8] and Eurocode 2 [7]:

$$V_{Rd.c} = \varphi \cdot \frac{I_{cs} \cdot b_w}{S_{cs}} \cdot \sqrt{f^2_{ctd} + \beta \cdot \alpha \cdot \sigma_{cp} \cdot f_{ctd}} \tag{4}$$

where:

- α – l_x/l_{pt2} for prestressing strands, max. 1.0;
- l_x – the distance from the concerned cross-section to the front of the element;
- l_{pt2} – upper design value of transmission lengths (1.2 l_{pt});
- σ_{cp} – ompressive stress from the prestressing in the concrete;

φ – empirical reduction factor (φ = 0.8 by EN 1168 and MC2010; φ = 1.0 by Eurocode 2);
β – reduction factor (β = 0.9 by EN 1168; β = 1.0 by Eurocode 2 and MC2010).

The engineering evaluation of tangent stress from torsion action τ_T in the cross-section of the hollow core slab requires simplification of the cross-section geometry by reducing to thin-walled rectangular cross-section. The guidelines in the latest version of Model Code 2010 [8] and EC2 [7] concerning the determination of the effective width of the separated shell, refer to the solid reinforced cross-sections or box sections with reinforced walls. There are no unequivocal regulations describing how to assume a simplified cross-section for hollow-core slabs, which are practically without reinforcement, especially that in common practice various shapes of the cross-sections of HC units are being applied – the most popular examples of cross-sections are shown in Fig. 3.

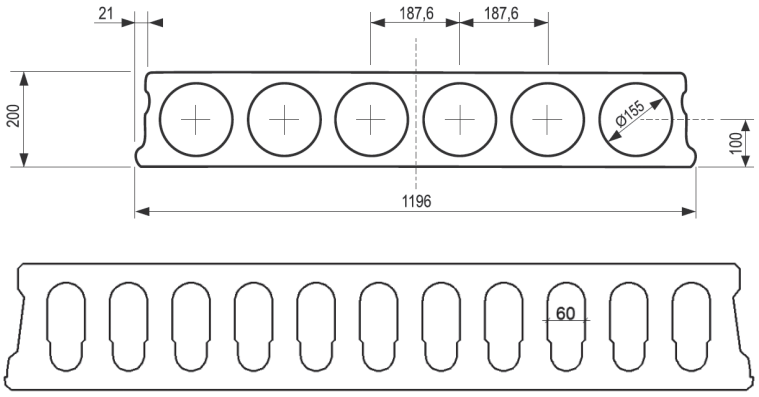

Fig. 3. Examples of cross-sections of HC slabs

In most cases, the simplification of the hollow-core slab cross-section consist on assumption of rectangular box section with the walls thickness equal the smallest width of the outermost webs of the real slab (Fig. 4). The equivalent width of the wall of the reduced cross-section t should not exceed the ratio A/U, where:
A – area of the cross-section, including the area of the cores;
U – perimeter of the reduced cross-section according to Fig. 4 [2].

For the simplified box section, the torsional sectional modulus W_T is expressed by the equation:

$$W_T = 2t \cdot \left[h - \frac{(t_{top} + t_{bottom})}{2} \right] \cdot (b_{sl} - b_{w.out}) \tag{5}$$

where $t = t_{top}$ (or $b_{w.out}$) for the calculation of stresses in the top or bottom flange (or in the outermost web).

Other geometrical denotations for the purpose of the W_T calculation are given in Fig. 4.

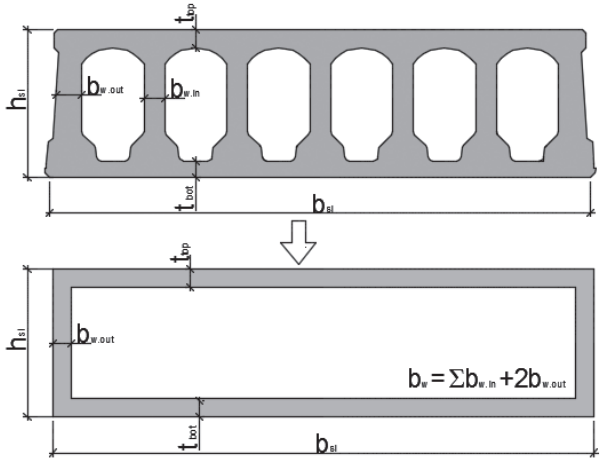

Fig. 4. The method of transformation of the real HC slab cross-section into a reduced thin-walled cross-section

Pure torsion resistance in the pretensioned hollow-core cross-section, which is reached in the moment of the appearance of the first crack, should be determined separately for horizontal flanges of the cross-section $T_{Rd.top}$ and outermost webs $T_{Rd.web,}$ according to the following equations:

$$T_{Rd.top} = W_{t.top}\sqrt{f_{ct}^{\ 2} + \sigma_{cp} f_{ctd}} \tag{6}$$

$$T_{Rd.web} = W_{t.web}\sqrt{f_{ct}^{\ 2} + \alpha\sigma_{cp} f_{ctd}} \tag{7}$$

The analytical computational model of the shear resistance in the case of simultaneous actions of transverse forces and torsional moment, is based on the assumption that the tangent stresses from shear and torsion could be super-positioned. As a result, shear strength $V_{Rd.c}$ is reduced by the design value of the transverse force caused by torsion V_T:

$$V_{Ed.n} = V_{Rd.c} - V_T \tag{8}$$

where $V_{Ed.n}$ is a 'net' value of the transverse force, due to transverse shear only.

The value of the transverse force from torsion actions V_T can be evaluated in the following way [1]:

$$V_T = \frac{T_{Ed} \cdot b_w \cdot I_{cs}}{2b_{w.out} \cdot (b_{sl} - b_{w.out}) \cdot [h_{sl} - (t_{top} + t_{bot}) \cdot 0.5] \cdot S_{cs}} \tag{9}$$

Under the assumption $I_{cs}/S_{cs} \approx d$ and $[h_{sl} - (t_{top} + t_{bot})\cdot 0.5] \approx d$, where d denotes the effective height of the cross-section, the expression defining V_T force can be written as:

$$V_T = \frac{T_{Ed} \cdot b_w}{2b_{w.out} \cdot (b_{sl} - b_{w.out})} \tag{10}$$

The abovementioned equation was accepted in standard [6] concerning the designing of the hollow-core slabs.

3. Experimental tests and numerical analysis of HC slabs under torsional actions

The issue of the influence of torsion in hollow-core slabs was the subject of an extensive experimental program carried out at full scale, in the VTT Research Centrum of Finland in 2004 [11–14]. This is the world's leading institution engaged in the problem of hollow-core floor slab performance. Research program assumed testing the influence of pure torsion and interaction of torsion and shear on single elements and panel floors consisting of the assembly of four hollow-core slabs.

In the first stage of the experiment [11], individual elements loaded with two alternating concentrated forces (see Fig. 5 [L]) were tested. One force was located in the corner zone of passive support, the other in the corner zone of active support (with the possibility of displacement). This static scheme, with concentrated forces applied to the element eccentrically relative to the axis of the element, allowed for the induction of pure torsion action.

In all slabs, failure occurred by the cracking of the top surface of the precast element, which developed at the angle of 45° to the longitudinal axis of the element. For slabs with a height of 400 mm, the value of the torsional rigidity determined from experimental investigations was close to the value determined analytically; however, for slabs with a height of 200 mm, the calculated value of stiffness was 30% smaller than that obtained from tests. Design torsional resistance was respectively 60% and 70% of the strength acquired from the experimental testing for slabs with heights of 200 and 400 mm.

In the second stage [12], fifteen simply supported hollow-core elements were tested. In those tests, the effect of shear was acquired due to the application of one or two concentrated forces in the support zone; additionally, the effect of torsion was induced by applying two concentrated forces in two alternating corners of the slab (see Fig. 5 [P]).

In ten out of fifteen tests, slabs were supported on neoprene pads and the cores remained empty (as opposed to being filled with concrete). For those slabs, the transverse bending of the element cross-section caused lateral cracking and accelerating failure which took place at a load value lower than the design strength. In the remaining five cases, the cores were filled with concrete in the support zone and the slabs were supported directly on the non-deformable beam. Change of the support conditions had a major influence on the bearing capacity of the slabs – this reached values comparable or higher than the analytical calculation results.

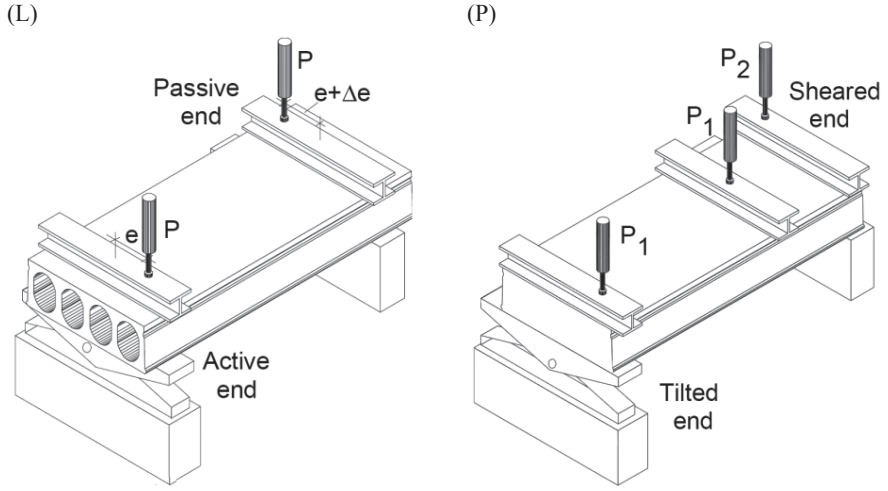

Fig. 5. Testing stand for pure torsion (L) and torsion-shear interaction (P) [11, 12]

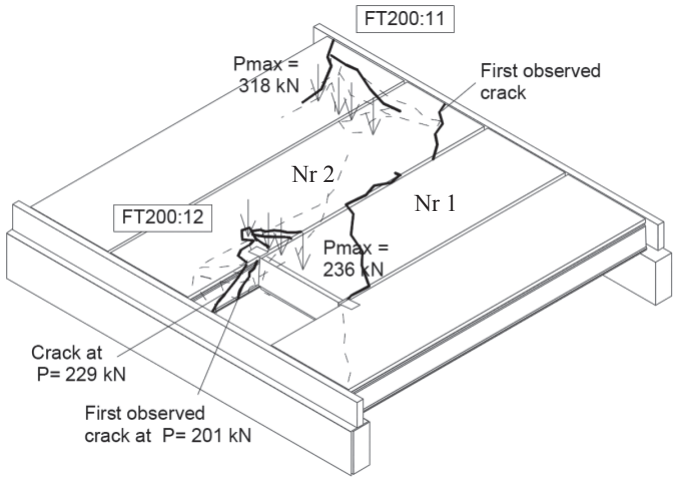

Fig. 6. Testing stand for the torsion-shear interaction for HC200 with the recess [13]

In the third stage [13], twelve floor slabs consisting of four hollow-core elements with heights of 200 mm were put to the tests of interaction of torsion and shear (see Fig. 6), thus being the tests of confined torsion. In the area of the support zone of one of the middle elements, a recess was made and shortened slab No1 was supported on the two adjacent slabs by the steel trimmer beam. The loading was applied as two linear arrays, each consisting of four concentrated forces localised in the zone of the trimmer-beam support and the opposite corner of slab No. 2. The force causing failure of the floor slab was significantly larger than that for the single element from the second stage of the testing program. It was also noted that the trimmer-beam in the recessed area carries only a minor proportion of the support reaction

from the variable loading applied to slab No1, and the major proportion of it is carried by the slab joints filled with the concrete.

In the tests of the torsion and shear interaction [14] of the hollow-core slabs with a height of 400 mm, fifteen floor slabs were tested. In the first twelve tests, the value of the transverse force was limited to the maximum value concerning the serviceability limit state, and there were no distinct symptoms of failure observed. The remaining three testing elements were loaded up to failure, and the damaging force was from 25% to 97% larger than that in the tests of single slabs with the same support conditions.

Since major differences between the test results of strength and torsional rigidity and the results of the earlier analytical calculations were observed, the need for development of more accurate computational models was necessary. The conducted experimental tests served the purpose of the development and calibration of the numerical computational model utilising FEM analysis, executed by the Holcotors team at Chalmers University of Technology in Göteborg.

The results of the calculations of torsion and shear interaction on the basis of FEM analysis differ from the results of analytical calculations according to the code EN1168. They give much higher values of capacity, independently from the loading scheme with transverse force and torsional moment. However, for the case of pure torsion, FEM calculations provided lower values of strength than analytical calculations. This is associated with a different model of failure, and as a consequence, the possibility of cracking of the top flange of the slab – this is not taken into consideration by the code EN 1168.

The authors of the Swedish model are of the opinion that diagrams created on the basis of the numerical analysis could be the most convenient and at the same time, the most accurate method of designing hollow core slabs under those types of actions [2]. The exemplary diagrams of torsion-shear interaction for the prestressed slab with a height of 200 mm and a transmission length in the range of the width of the shear zone equal to 0.8 m (black continuous line) and 0.5 m (grey continuous line) have been presented. The straight grey line represents an interaction curve determined on the basis of the standard method EN1168. The map of cracking based on the FEM analysis is presented in Fig. 7, pictures (a) – (j) [3].

4. Parametric analytical studies

For the purpose of presenting the scale of the torsion effect in hollow-core slabs, the computational example on the basis of analytical model presented above was conducted. For the benefit of calculations, hollow-core slabs made from concrete class C50/60 were assumed with three different cross-section heights of 200 mm, 320 mm, 500 mm and effective spans of 8 m, 12 m and 16 m. Slabs were assumed to be simply supported, loaded with their own weight with an additional static load of Δg_d = 1 kN/m^2 and uniformly distributed live load of q_d = 5 kN/m^2. In the analysis of torsion, the value of the applied design torsional moment was assumed to be within the range 13–36 kNm depending on the height of the slab. This value was determined in the exact same way as for the case when the considered element acts as a support for the trimmer-beam of the adjacent slab with the recess. Torsional strength of the flange was determined from equation (6), and the outermost web from equation (7). The sectional modulus was calculated from equation (5).

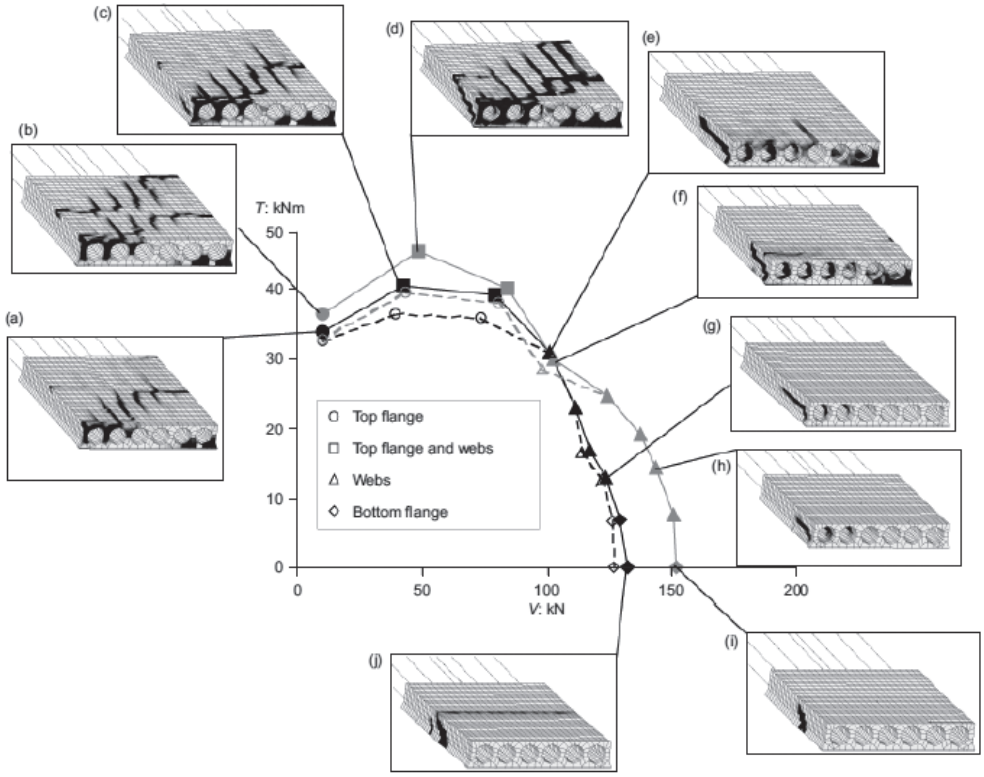

Fig. 7. Torsion and shear interaction for HC200 slab, according to the Holcotors numerical model

The subject of the first analysis was a strength comparison of hollow-core slabs with different cross-sections depending on the production technology. The cross-sections of elements produced using slip-forming technology (approximately rectangular cores) – type 1, and extruded elements (circular cores) – type 2, were compared. The results of the calculations of transverse force due to torsion in the external web V_T (also as a percentage of the total shear load capacity $V_{Rd.c}$) and the 'net' value of the transverse force $V_{Ed.n}$ compared to the value of shear force due to vertical load V_{Ed} were presented in Table 1.

The results of the conducted analysis proved that with the assumption of a highly probable design value of the torsional moment (in practice, cases with bigger contribution of torsional moment e.g. due to the additional concentrated loads or additional torsion caused by flexibility of the supports, may happen) the contribution of torsion in overall bearing capacity of the slab's web equals around 22%–37%. Obviously, most susceptible to torsion are slabs with small cross-section heights – in those elements, with unfavourable loading configurations, design deficiency of the shear capacity may arise.

The influence of the structural topping concrete layer on changes in maximal tangent stresses and transverse forces in the slab's web due to the interaction of torsion and shear, were also subjected to the analysis. Calculations were carried out for a slab with a height of 320 mm and a span of 12.0 m loaded with variable loading q_d = 5 kN/m^2 and a design

torsional moment of 22 kNm. A layer of reinforced concrete topping was assumed with three different thicknesses: 50 mm, 65 mm and 80 mm. Full composite action between the precast floor element and the topping layer was considered. The results of the calculations are presented in Table 2.

The presence of the topping concrete layer changes the geometry of the cross-section, and thus influences the magnitude of tangent stresses in the outermost web of the slab. As a result of increasing the thickness of the topping concrete, a constant increase of the transverse force from torsion V_T (see eq. [7]) is obtained. Due to the fact that simultaneously, the increase of the topping concrete thickness is followed by the increase of transverse shear strength $V_{Rd.c}$ (because the height of the cross-section increases), the final influence of the topping concrete on torsion-shear bearing capacity can be assumed negligible.

Table 1

Limit transverse force in outermost rib under torsion-shear interaction

			Cross-section type 1 	Cross-section type 2 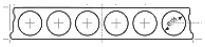
HC200	$V_{Rd.c}$	[kN]	139	94
	V_T	[kN]	51	30
	$V_T/V_{Rd.c}$	[%]	37	32
	$V_{Ed.n} = V_{Rd.c} - V_T$	[kN]	88	64
	V_{Ed}	[kN]	61	56
HC320	$V_{Rd.c}$	[kN]	156	158
	V_T	[kN]	45	46
	$V_T/V_{Rd.c}$	[%]	29	29
	$V_{Ed.n} = V_{Rd.c} - V_T$	[kN]	111	112
	V_{Ed}	[kN]	101	110
HC500	$V_{Rd.c}$	[kN]	289	280
	V_T	[kN]	84	62
	$V_T/V_{Rd.c}$	[%]	29	22
	$V_{Ed.n} = V_{Rd.c} - V_T$	[kN]	205	218
	V_{Ed}	[kN]	156	157

Table 2

The influence of the thickness of the topping concrete on changes in tangent stress and transverse forces in the slab's web due to the interaction of torsion and shear

		Thickness of the concrete topping layer [mm]			
		0	50	65	80
$V_{Rd.c}$	[kN]	156	174	180	186
V_T	[kN]	45	55	60	65
$V_T/V_{Rd.c}$	[%]	29	32	33	35
$V_{Ed.n} = V_{Rd.c} - V_T$	[kN]	111	119	120	121
V_{Ed}	[kN]	101	112	117	121

5. Conclusions

In the case of designing precast, pretensioned hollow-core floors, with complicated support conditions (e.g. support on three edges; on non-parallel supports; direct support on the columns; cases of slim floor structures) or non-uniformly distributed loading (e.g. linear loading and loading with concentrated forces), it is necessary to take into consideration simultaneous actions of torsional moment and transverse force. Both torsional moment and transverse force generate tangent stress. In the case of compound actions of torsion and shear in the hollow core slab, one outermost web is subjected to the joined influence of tangent stress with a considerably higher value than the remaining webs, which may lead to cracking and loss of bearing capacity.

The computational method of taking into account this phenomenon presented in the code PN-EN 1168+A3:2011 is based on the same principal assumptions as EC2 and Model Code 2010 but introduces several simplifications. The conducted computational analysis proved that the contribution of torsion actions in the bearing capacity of the outermost web of the hollow core element could be significant, and in the case of small height slabs (e.g. 150 mm up to 200 mm), endangered by the presence of significant torsional moments, design deficiency of the shear capacity may arise. Experimental tests and advanced numerical analyses conducted in leading research centres around the world demonstrated that the results of capacity calculations according to the standards, for the case of torsion and shear interaction, are significantly lower than values obtained from experimental tests or precise numerical calculations, which lead to acquiring a larger safety margin. However, it should be noted that in case of pure torsion, overestimated values of design resistance are obtained – this is caused by the occurrence of a different failure model than that assumed by the standards, i.e. torsional cracking of the upper surface of the slab, instead of cracking of the outermost webs.

The layer of the structural concrete topping cast on the precast elements is usually regarded as a method of increasing the capacity of the slab, but based on the conducted analysis, it can be concluded that in the case of torsion-shear interaction, this effect is insignificant.

References

[1] Broo H., *Shear and Torsion in Concrete Structures. Non-Linear Finite Element Analysis in Design and Assessment*, PhD Thesis, Chalmers University of Technology, Göteborg, Sweden 2008.
[2] Broo H., Lundgren K., Engstrom B., *Shear and torsion interaction in prestressed hollow core units*, Magazine of Concrete Research, No. 9, 2005.
[3] Broo H., Plos M., Lundgren K., Engstrom B., *Simulation of shear-type cracking and failure with non-linear finite element method*, Magazine of Concrete Research, No. 9, 2007.
[4] Derkowski W., Surma M., *Complex Stress State in Prestressed Hollow Core Slabs*, [in:] Monograph No. 478, *Recent Advances in Civil Engineering: Building Structures*, Cracow University of Technology, 2015, 9–28.
[5] Derkowski W., Surma M., *Shear Capacity of Prestressed Hollow Core Slabs on Flexible Supports*, Technical Transactions, 2-B/2013, 3–12.
[6] EN 1168:2005+A3:2011 Precast concrete products – Hollow-core slabs, 2011.
[7] EN 1992-1-1:2008 Eurokod 2: Design of concrete structures – Part 1-1: General rules and rules for buildings, 2008.
[8] ***fib*** Bulletin 65, Model Code for Concrete Structures 2010, ***fib***, Lausanne, Switzerland 2012.
[9] Godycki-Ćwirko T., *Concrete, Reinforced and Prestressed Structures*, Scientific Commentary to PN-B-03264: 2002 –Chapter 9: Torsion, Warszawa 2005.
[10] Godycki-Ćwirko T., *Mechanics of concrete*, Arkady, Warszawa 1982 (in Polish).
[11] Pajari M., *Pure torsion tests on single hollow core slabs*, VTT Research Notes 2273, Finnland 2004.
[12] Pajari M., *Shear-torsion interaction tests on single hollow core slabs*, VTT Research Notes 2275, Finnland 2004.
[13] Pajari M., *Shear-torsion tests on 200 mm hollow core floor*, VTT Research Notes 2276, Finnland 2004.
[14] Pajari M., *Shear-torsion tests on 400 mm hollow core floor*, VTT Research Notes 2274, Finnland 2004.
[15] Seruga A., Sokal P., *Skręcane elementy z betonu sprężonego w świetle wybranych badań doświadczalnych*, Czasopismo Techniczne, 4-B/2012, 119–132.

TECHNICAL TRANSACTIONS | CZASOPISMO TECHNICZNE
CIVIL ENGINEERING | BUDOWNICTWO
3-B/2015

KRZYSZTOF DYDUCH*, RAFAŁ SZYDŁOWSKI**

MATERIAL-CONSTRUCTION SOLUTIONS APPLIED IN LONG-TERM REPAIRS OF REINFORCED GRANULATION TOWERS IN NITROGEN PLANTS

ROZWIĄZANIA MATERIAŁOWO-KONSTRUKCYJNE STOSOWANE W REMONTACH ŻELBETOWYCH WIEŻ GRANULACYJNYCH W ZAKŁADACH AZOTOWYCH

Abstract

In one of the oldest chemical plants in Poland are two reinforced concrete towers for fertilizer granulation which were built in the nineteen-thirties. These towers have operated continuously in a very hostile environment for about fifty years. The authors of this paper have used ad hoc methods of repair and protection with varying degrees of success for several years. In 2012, the renovation of one of the towers was designed and implemented with a view to its continuous use over a period of twelve years. A new comprehensive method of protecting the tower was applied due to its relatively long-term use. The resulting tower damage, the results of chemical and structural analysis of the concrete and coating stress are presented in this paper. Furthermore, security methods applied by them and their functionality after a few years of use as well as material and construction details relating to works performed to make the tower operational over the next twelve years are presented.

Keywords: *concrete, concrete corrosion, fertilizers, granulation tower, nitrogen plants*

Streszczenie

W jednych z najstarszych polskich zakładów chemicznych w latach trzydziestych poprzedniego stulecia wzniesiono dwie żelbetowe wieże do granulacji nawozów sztucznych. Wieże pracowały nieprzerwanie w agresywnym środowisku przez ponad 50 lat. W celu utrzymania ich w eksploatacji autorzy artykułu w ostatniej dekadzie stosowali z różnym skutkiem doraźne metody napraw i zabezpieczeń. W 2012 roku zaprojektowano i przeprowadzono remont jednej z wież z zamiarem jej dalszej eksploatacji przez okres 12 lat. Ze względu na długi przewidywany okres eksploatacji zastosowano zupełnie odmienny, kompleksowy system zabezpieczenia wieży. W artykule przedstawiono stan techniczny wieży przed naprawą, wyniki badań chemicznych i strukturalnych betonu oraz analizę wytężenia żelbetowej powłoki wieży. Zaprezentowano ponadto stosowane dotychczas doraźne metody napraw wraz z oceną ich skuteczności po kilku latach użytkowania, a także szczegóły materiałowo-konstrukcyjne remontu wykonanego z zamiarem nieprzerwanego użytkowania wieży przez okres 12 lat.

Słowa kluczowe: *beton, korozja betonu, nawozy sztuczne, wieża granulacyjna, zakłady chemiczne*

DOI: 10.4467/2353737XCT.15.161.4336

* Prof. Krzysztof Dyduch, Faculty of Architecture and Fine Arts, Andrzej Frycz Modrzewski Cracow University.

** Ph.D. Eng. Rafał Szydłowski, IMBS, Faculty of Civil Engineering, Cracow University of Technology.

1. Introduction

Granulation towers have long been an integral part of the process of granulation of fertilizers. In one of the oldest chemical plants in Poland, two reinforced concrete towers with an inner diameter of 19.6 m and a total height of 36.0 m (Fig. 1) were built in the nineteen-thirties. The upper part of the tower was rebuilt in the post-war years. For over fifty years, the towers operated in the aggressive environment of the chemical plant until the present century. Their poor technical condition and the necessity to keep them operational due to the increasing global demand for fertilizers in agriculture led to their further use in parallel with a modern mechanical fertilizer granulation line. Therefore, since 2002, the towers have been temporarily repaired to prevent their further degradation. In recent years it has been decided to develop the project and repair the towers with the intention of putting them into operation for a further 12 years. The need to ensure safe operation of the structure for such a long time in an aggressive environment forced the authors of this paper to search for materials and repair methods that are much more durable than those used in previous repairs and intended to last for a period of several years.

a) b)

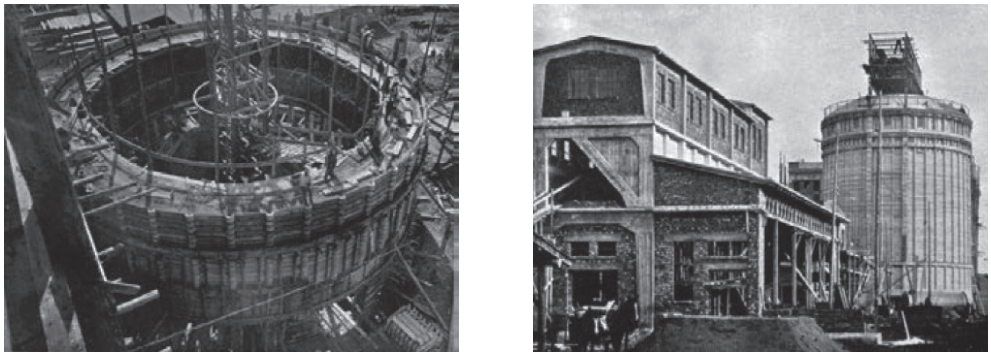

Fig. 1. a) One of the granulation towers during construction; b) A view of one of the towers from the nineteen-thirties

In this work, the experts present the structure of the granulation towers, their technical condition after many years of operation, an analysis of structural stress, the results of chemical analysis and the state of the concrete corrosion. Also, the methodology of emergency repairs and their effectiveness as well as the technology of the repairs are presented considering that they are to be used for the next 12 years.

2. Description of the building in structural terms

The structure of the tower is mixed (Fig. 2). The foundation up to a level of +6.00 m is formed by a reinforced concrete monolithic structure with a height of 3.0 m supported by columns. The main part of the cylindrical shell between the levels of +6.00 and +32.00 m

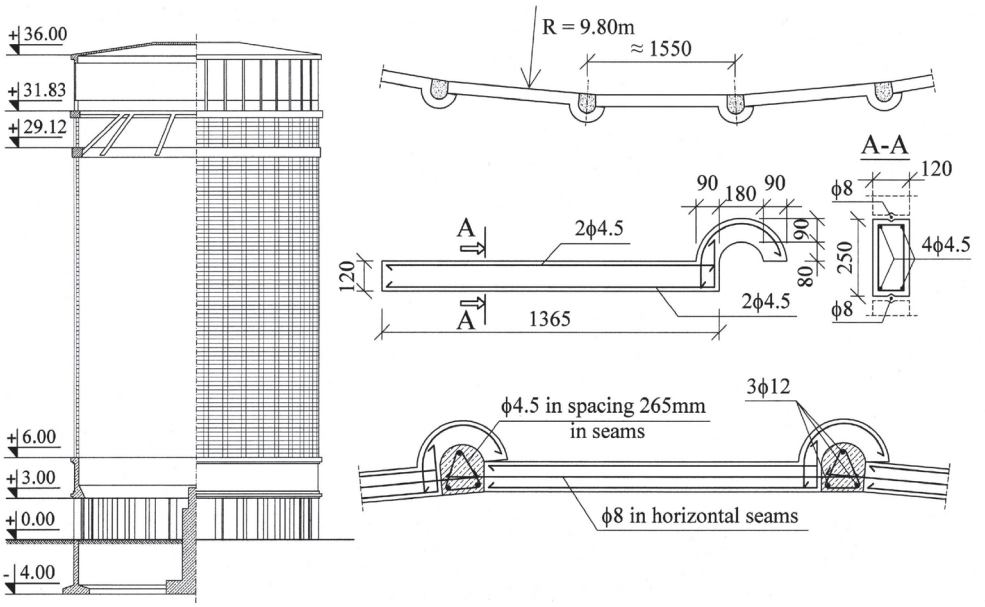

Fig. 2. Geometry and structural details of the granulation towers

is made of reinforced concrete key aggregates using Monnoyer's system. The technology of the erection of polygonal buildings (or circular buildings with a large diameter) using key aggregates was developed by Dumas, the Belgian engineer, mainly for building chimneys. An essential element of the system is a key aggregate with a height of 0.25 m, ending with a head in the form of a hook, the hollow interior of which allows for the insertion of vertical steel bars combined with stirrups. For the analysed towers, key-aggregates with a cross-section of 0.12 × 0.25 m and a modular length of 1.55 m are used. The longitudinal reinforcement of the key aggregate is formed by 4 bars ϕ 4.5 mm. A triangular core composed of three bars ϕ 12 mm and stirrups ϕ 4.5 mm are placed every 265 mm inside the hooks. As a result, a cylindrical coating with a thickness of 0.12 m with 40 vertical ribs on the circumference placed every 1.55 m is created.

Monolithic reinforced concrete tie beams are made at levels of +29.12 and +31.83 m. These beams support a technological ceiling with a strut steel construction. The crowning of the tower is made of a reinforced concrete-masonry structure covered with a reinforced concrete beam-and-slab plate.

3. Description of the damage in 2002 (after 50 years of operation)

In 2002, after fifty years of operation in the aggressive environment of the plant, the towers were subjected to advanced degradation as a result of the ammonium and sulphate corrosion of the concrete. The monolithic foundation of the tower (Fig. 3) as well as the prefabricated

cylindrical shell (Fig. 4) were seriously destroyed. Losses of concrete in the prefabricated wall reached two-thirds of the wall thickness. Additionally, there was considerable local damage to the cross-section of the vertical ribs. In the lower monolithic part of the tower, the concrete cover of the cylindrical walls, columns and tie beams were damaged. Almost completely corroded reinforcing bars were localized.

Fig. 3. Corrosion of monolithic foundation of the tower in 2002

Fig. 4. Corrosion of the prefabricated cylindrical shell (2002)

The samples of concrete taken from the ribs of the cylindrical coating and the columns of the foundation of tower No. 2 were characterised by a very strong absence of alcalisation (pH of the aqueous extract amounted to 8.0–9.0), higher content of chloride ions (about 0.33% of the weight of the binder) and the content of sulphate ions was within the normal range (approximately 2.5% of the weight of the binder).

The samples of concrete taken from the ribs of the cylindrical coating and the columns of the foundation of tower No. 2 were characterised by a very strong absence of alcalisation (pH of the aqueous extract amounted to 8.0–9.0), higher content of chloride ions (about 0.33% of the weight of the binder) and the content of sulphate ions was within the normal range (approximately 2.5% of the weight of the binder).

4. Ad hoc repairs and strengthening of the towers

In 2002, ad hoc repairs were made and tower number 2 was strengthened with the intention of its further operation for a period of 5 years. It was presented by Dyduch, Płachecki et al. [1]. For the reprofiling of the damaged concrete elements (surface of the prefabricated shell of the tower, tie beams and monolithic foundation elements), class B25 mortar was recommended (or concrete in the case of more extensive damage) to be used on CEM-II/A-D silica Portland cement with the addition of high-quality plastic dispersion – this was based on a styrene-butadiene from a reputable supplier of construction chemicals and designed to improve repair screeds and make a bonding layer. On the basis of that dispersion, it was also recommended to use the bonding layer.

It was recommended to remove the concrete cover from reinforced concrete foundation columns and to protect these columns with a 5–7 cm thick reinforced layer. Additionally, the concreting of the monolithic ring wall from the outside was designed to be at a level of +3.00 to +6.00 m with 15 cm thick concrete reinforced with two meshes ϕ 8 every 150 mm on both surfaces and anchored to the original wall with ϕ 12 mm anchors spaced at 300 × 300 mm.

The reinforcement of the tie beams at a level of +29.12 and +31.83 m were designed in the form of steel casing as well as additional 10 HEA 160 vertical bars extending from a level of +6.0 to +29.12 m and anchored to the prefabricated cylindrical wall (Fig. 5). The role of the designed reinforcement was to safely transfer the loads from the top of the tower (technological ceiling, flat roof and reinforced concrete upward extension) and relieve the prefabricated coating.

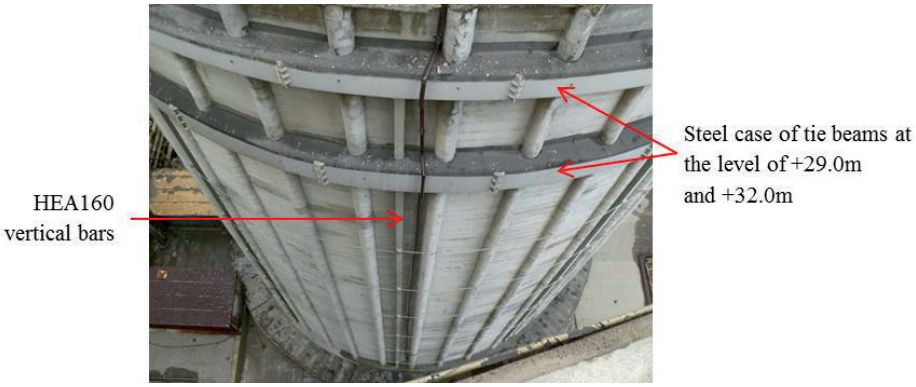

Fig. 5. Steel reinforcement of the granulation tower

The tower had again degraded 4 years after its repair. The precast coating reinforced concrete elements (Fig. 6a) were significantly damaged. The concreting of the pillars of the foundation was seriously cracked and loose. One of the reasons for the damage was certainly the contractor's breach of technological regimes contained in the project and instructions for the use of materials for re-profiling. Undoubtedly, the main reason for the damage was contaminated concrete and the aggressive environment around the towers – this was caused

a) b)

Fig. 6. a) damage of prefabricated shell elements four years after repair; b) exhaust chimney near the tower

by the location of exhaust chimneys in the immediate vicinity (Fig. 6b). Approx. 3 kg/h of ammonium nitrate (NH_4NO_3) is removed from the exhaust air coming from the chimneys. The contamination of concrete and its progress is presented in section 5.

5. The results of chemical testing of concrete

During the technical inspection of the towers, concrete samples were taken to assess the degree of contamination and evaluate the protective properties of the cement material in relation to steel. The condition of the concrete was evaluated on the basis of the pH value of the aqueous extract, the content of sulfate, chloride and nitrate ions, and observations made using a scanning electron microscope.

The measurements of the pH value of the aqueous extract were made with a pH meter microprocessor with an accuracy of ± 0.05 pH. The content of sulphate (SO_4^{2-}), nitrate (NO_3^-) and chloride (Cl^-) ions was determined according to [2]. Sulphates were identified in the acetone environment by titration with a standard $BaCl_2$ solution in relation to Nitrosulfonazo III. Chloride ions were analysed using a MERCK test by bonding them into $HgCl_2$ (the mercurometric method). Nitrates were identified by using an ion-selective electrode (nitrate electrode).

Table 1 summarises the results of chemical analysis of the samples taken from tower No. 1 in 2006 and 2013. When analysing the pH value of an aqueous extract, it may be noted that the value ranged from 8.70 to 11.70 (average value – 10.03) in 2006, while in 2013, it ranged from 8.20 to 8.70 with the average value of 8.43. Such a strong reduction of pH over seven years results from a progressive corrosion of sulfate and ammonium concrete. The elimination of calcium hydroxide from the cement binder causes a strong decrease of pH, which results in the absence of the protective properties of concrete for reinforcing steel. The concentration of Cl^- ion, calculated in relation to the weight of the binder, does not exceed the limit values (0.4%). This indicates that the concrete did not undergo changes associated

with chloride corrosion. In the considered period of seven years, a significant increase in SO_4^{2-} ions was identified – this proves the progressive corrosion of sulphate. The ion content, as compared to the weight of the binder in 2007, amounted to 2.5% in all three tested samples. Meanwhile, in the samples taken in 2013, that value ranged from 3.5 to 5.0 (with an average value of 4.38). Figure 7 presents the results of observation in the scanning electron microscope for one of the samples taken in 2013. The results present a leaky structure formed by the processes of dissolution and sulfate corrosion (Fig. 7a), as well as its confirmation in EDS analysis (ettringite formation – Fig. 7b).

Table 1

The results of chemical analysis of the concrete samples

Year of test	Sample number	pH	SO_4^{2-}	Cl^-
			% of binder weight	
2006	1	8.7	2.5	0.33
	2	11.7	2.5	0.08
	3	9.7	2.5	0.08
2013	1	8.2	5.0	0.14
	2	8.5	4.5	0.22
	3	8.3	4.5	0.14
	4	8.7	3.5	0.20
Ultimate values		> 11.8	≤ 3.0	< 0.4

a)

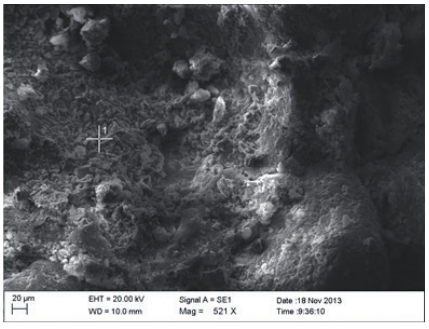

b)

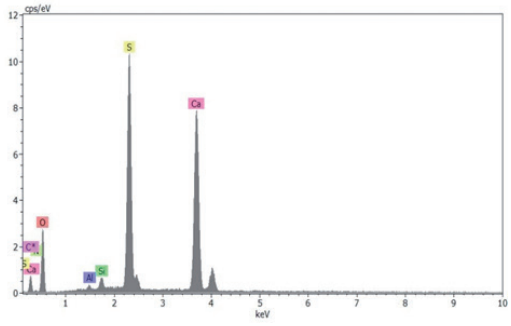

Fig. 7. The results of the observation of the concrete sample in the scanning electron microscope: a) leaky structure formed by the processes of dissolution and sulfate corrosion; b) EDS analysis results (ettringite formation)

6. The material and construction solutions used in the renovation of the towers for the purpose of their use for a further twelve years

6.1. Basic assumtions

In 2011, the decision was taken to repair and secure the two towers, thus providing their trouble-free and uninterrupted use for the following twelve years (until 2024). The repairs of tower No. 2 conducted twice so far have proved that repair techniques will not bring satisfactory results over such a long period. Additionally, the progressive pollution and destruction of the concrete structure reported in the chemical and structural examination have confirmed the need for a much more efficient and more sustainable protection of the reinforced concrete elements.

6.2. The analysis of stress of the tower

In order to estimate the stress of the tower elements, a numerical model in the FEM system was built. The model included all operating fixed and variable loads (the weight of the tower components, technological floor load at a level of +31.83 m, snow and wind).

The analysis considered two options: Option 1 – prefabricated panel thickness reduced to 60 mm (equivalent to seriously damaged panels), Option 2 – the wall with a full thickness of 120 mm. In both options, the interaction of vertical steel pillars in the transferring of loads was taken into consideration.

In Figure 8, the analysis of the results in the form of vertical stresses in the coating (8a) and forces in the steel pillars (8b) for Option 1 are presented. Compression in the concrete

a) b)

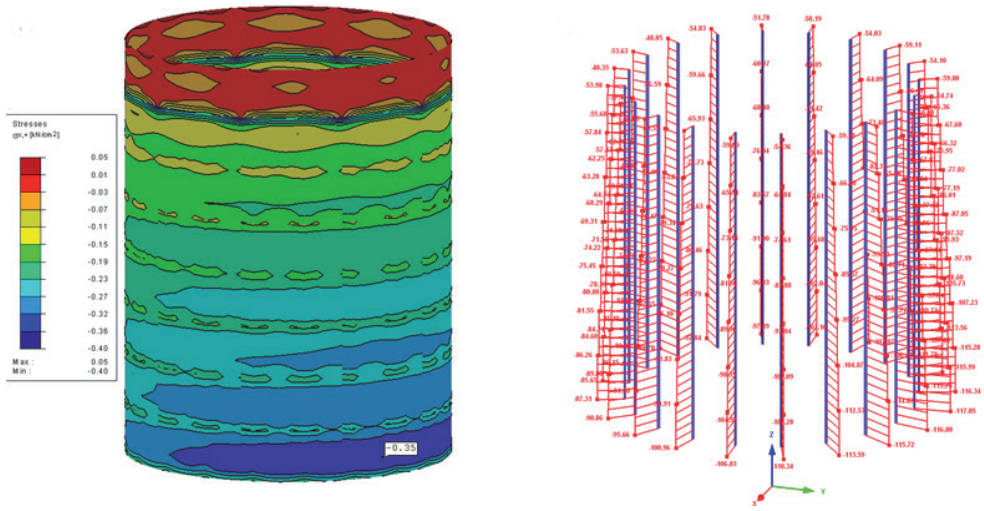

Fig. 8. The results of static analysis of the structure for Option 1: a) concrete shell vertical compression [kg/cm^2]; b) steel pillar forces [kN]

slabs of the coating amounted to 3.5 MPa for Option 1 and 1.9 MPa for Option 2. Forces in the steel pillars amount to 117.1 and 65.0 kN, which generate compression in the steel sections equal to 30.2 and 16.8 MPa.

The conducted analysis of stress indicates a high level of compression in the concrete slabs (3.5 MPa) in Option 1. Given a dramatically low technical condition of the concrete, the loss of even half of thickness of the coating resulting the concrete stress increase can be considered. As a result, the compressive stresses can cause a loss in the stability of the reinforced concrete cylindrical shell and losses of concrete fragments.

6.3. Material and structural solutions for repairs and reinforcements

Because of a high level of concrete stress, a low durability of previously conducted repairs and a long period of the planned operation of towers had to be used a good protection. The effectiveness of repairs to deeply damaged concrete elements depends on the bonding of the applied repair layer with a concrete base. For this reason, bonding layers are applied according to the 'wet on wet' principle, i.e. after the application of the bonding layer, prior to its bonding and drying, the surface should be repaired. This technological requirement hinders the execution of repairs. Defective execution of repairs decreases their efficiency and durability. Additionally, the effectiveness of repairs is worsened by the low strength and chemical contamination of concrete. In order to ensure long-term protection of the elements of the tower in a contaminated environment, it was necessary to find a more effective solution than the solution used previously. Among other proposals, the possibility of making an outer coating, made of stainless steel, was considered. Finally, the system of a reputable supplier of construction chemistry, not requiring the use of an additional bonding layer, was applied. After the removal of the corroded concrete particles and thorough cleaning of the concrete surface and reinforcing steel, it was recommended that the extensive loss of concrete be replaced with fine-grained, thixotropic repair mortar with controlled shrinkage, reinforced by synthetic fibers with an average compressive strength of 30 MPa (Fig. 9a – mortar '1'). The mortar is usally applied in layers with thicknesses of up to 25 mm. After the re-profiling of concrete cavities, the reinforced protective coating of 5–6 mm was applied all over the surface of the prefabricated wall. For this purpose, a two-component cement mortar with high strength and plasticity dedicated to strengthening of masonry structure (mortar "2") was used. This mortar includes fine aggregate, special additives and an aqueous dispersion of synthetic polymers. Due to the high content of synthetic resin, it forms a stable and durable layer which is impermeable to water and the aggressive components present in the atmosphere, and it is not a barrier to water vapour diffusion. The protective layer was reinforced with an alkali-resistant glass fibre mesh with meshes of 25 × 25 mm and a weight of 225 g/m^2, tensile strength of 45 kN/m and strain at rapture of less than 3%. Given the poor adhesion of the protective coating applied to the corroded concrete, the anchoring to the original wall of the tower was applied with the support of nail anchors spaced at not more than 400 mm in both directions.

Reinforced concrete foundation columns were encased in a 3mm thick steel layer (Fig. 9b) after all loose and cracked concrete parts were forged together. After prior reinforcement of concrete filling of a steel casing in accordance with Fig. 9b (4mm vertical bars ϕ 16, pasted into the parent concrete, transverse stirrups and pasted bonding inserts), the inside of the casing was flooded with self-compacting concrete.

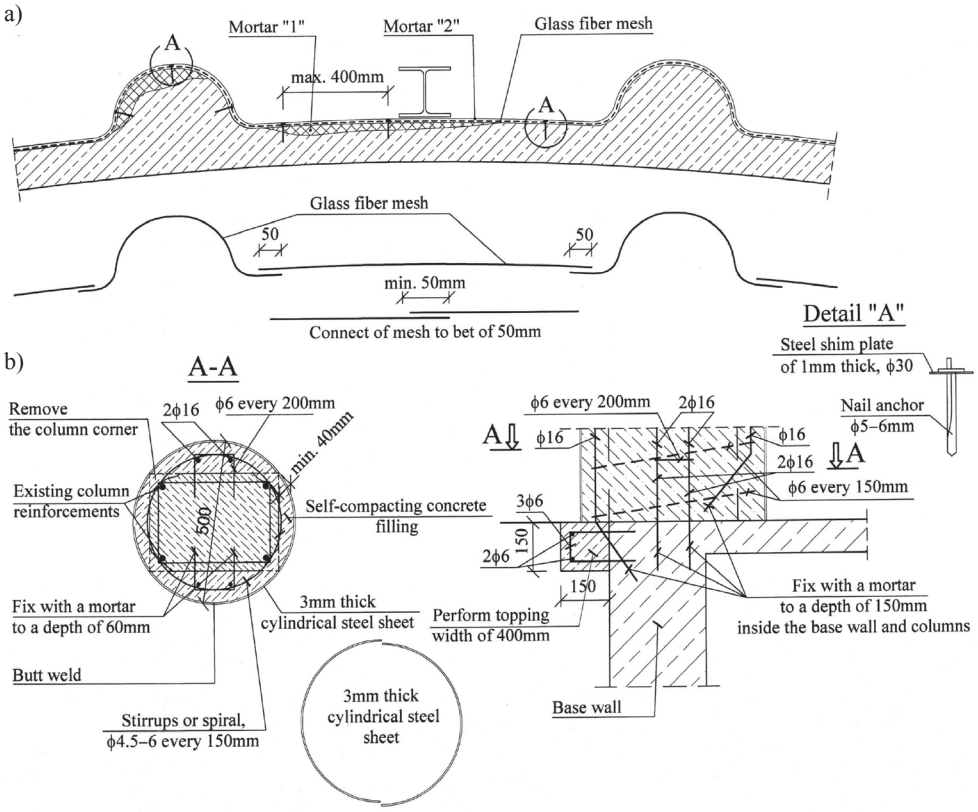

Fig. 9. a) details of protection of prefabricated concrete shell; b) reinforcement of foundation columns

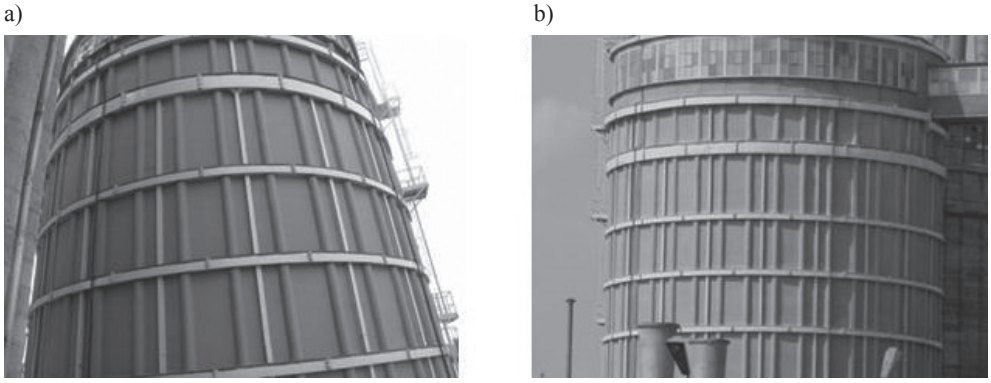

Fig. 10. a) the granulation tower shortly after renovation (mid-2012); b) the same tower after 2.5 years of operation

In addition to the complete repair and securing of protective coating, additional reinforcement was designed to increase the stiffness and stability of the wall. The number

of vertical HEA 160 steel posts was increased from 10 to 20 during the previous repair. Moreover, 6 reinforced peripheral tie beams with cross-sections of 300 × 300 mm, evenly spaced at 3.2 m, were designed. The tie beams were made from steel formwork (Fig. 10), armed longitudinally and transversely, and combined with the concrete wall.

7. Summary and conclusions

Taking into consideration the long-term, twelve-year use of the towers in the very aggressive environment and the sustainability of previously used methods of corrective repairs, a comprehensive but costly protection system was designed and implemented in one of the towers used for the granulation of fertilisers. The proposed technology has been accepted by the user of the building and executed under the supervision of designers and experts from the technical department of the manufacturer of the used construction chemistry products. Figure 10 shows a view of the tower shortly after renovation in mid-2012 (a) and at the beginning of 2015 (b). The inspection of the tower carried out after 2.5 years of operation showed no damage (cracks or delamination) to the protective layer. The results of the inspection bode well for the applied protection technology for the projected period of use until 2024. Keeping the tower in good condition will require only the renovation of the anticorrosion coating of steel elements.

References

[1] Dyduch K., Płachecki M., Sieńko R., Szydłowski R., *Repair and reinforcement damaged by corrosion reinforced concrete granulation tower in nitrogene plants* (in Polish), Proceedings of XXIII Conference on Structural Failures, Szczecin-Międzyzdroje, 23–26 May 2007, 733–740.

[2] BS 1881-124: 1988. Testing concrete – Part 124: Methods of analysis of hardened concrete.

[3] PN EN 1991-1-1. Eurocode 2: Design of concrete structures – Part 1-1: General rules and rules for buildings. September 2008 (in Polish).

[4] PN EN 1991-1-4: 2005+A1: Eurocode 1: Actions on structures – Part 1-4: General actions – Wind actions. April 2010.

TECHNICAL TRANSACTIONS | CZASOPISMO TECHNICZNE
CIVIL ENGINEERING | BUDOWNICTWO
3-B/2015

IWONA GALMAN*, JAN KUBICA*

STRESS–STRAIN CHARACTERISTICS OF BRICK MASONRY UNDER COMPRESSIVE CYCLIC LOADING

ZALEŻNOŚCI NAPRĘŻENIE – ODKSZTAŁCENIE MURÓW CERAMICZNYCH ŚCISKANYCH CYKLICZNIE

Abstract

This paper presents the results of laboratory experiments carried out on twelve clay brick masonry wallettes of two types under cyclic compressive loading. In the paper, the procedure adapted for testing is described and the results are discussed. The failure models and cracking patterns of the tested specimens are presented. The effects of the repeated load on the behaviour and mechanical properties of the wall are observed and discussed. Based on the results, the analytical formula for the determination of the failure envelope curve is also proposed.

Keywords: *uniaxial compression tests, brick masonry, cyclic loading, envelope curve*

Streszczenie

W artykule zaprezentowano rezultaty badań laboratoryjnych dwóch serii (łącznie 12) murów poddanych cyklicznej sile ściskającej. Przedstawiono procedury badań i obrazy zniszczenia, a wyniki poddano dyskusji. Obserwowano wpływ powtarzającego sie obciążenia ściskającego na zachowanie i parametry materiałowe muru. Podjęto próbę analitycznego opisu krzywej charakterystycznej: obwiedni.

Słowa kluczowe: *ściskanie, mury ceglane, obciążenie cykliczne, obwiednie badania cyklicznego*

DOI: 10.4467/2353737XCT.15.162.4337

* Ph.D. Iwona Galman, Prof. Jan Kubica, Department of Structural Engineering, Silesian University of Technology.

1. Introduction

Stress–strain relationship σ–ε is taken as the basic characteristic of material behaviour under loading. Usually, it is a curvilinear relationship dependent upon different factors. One of these factors is the loading scheme. Laboratory and theoretical investigations of the σ–ε relationship have been conducted for several years in many research centres worldwide. It is worth mentioning the paper published by Kaushik et al. [1] covering the collection and juxtaposition of test results and analytical considerations on the stress–strain relationship in masonry walls loaded to failure in one cycle. Nowadays, it could be taken that the σ–ε characteristic of masonry walls under monotonically compression is rather well described, whereas the examination of this relationship of masonry under cyclic loading remains incomplete. Karsan & Jersa [2] were the first to propose a description of the σ–ε characteristic of the cyclically loaded material with three characteristic curves: the envelope curve, the stability-point curve and the common-point curve of the σ–ε relationship. These recommendations, although initially developed for concrete, were also adopted for the characterisation of masonry. Since the nineteen-seventies, there have been trials to mathematically describe these curves. Sinha [3–5] proposed a definition of the σ–ε curve with an exponential function. Later, Nazar & Sinha [6] represented the characteristic curves with a fourth-order polynomial function. In 2013, Alshebani [7] returned to exponential representation. Evolution and different approaches to mathematical (analytical) description were also observed in the definition of loading curve (exponential [8], polynomial [9, 10]), which is useful in the assessment of damage intensity of the structure.

Conclusions from these analyses are interesting from a qualitative point of view. Nevertheless, the results have no practical use or quantitative meaning in Poland or other Central European countries as the tests were conducted on different types of masonry than those used in Central Europe. Moreover, results of these investigations were often contradictory to each other. Therefore, it is necessary to perform such analyses with masonry walls made of the most popular local components: solid clay brick on cement–lime mortar.

2. Experimental test

The experimental investigations were performed on two types of test specimens made of solid clay brick of strength class ‘15’ (f_b = 18.7 N/mm^2) and cement–lime mortar (1:1:6) class M5 (f_m = 6.8 N/mm^2). Specimens of **CV** type were used to determine the compressive strength of masonry and the stress-strain relationship according to the method given in EN 1052-1:2001 [11]. Masonry specimens of **MW** type had higher overall dimensions (according to the requirements specified in standard [11]) and the most popular thickness used in the construction of load-bearing walls in Poland (1 brick, i.e. 250 mm). Dutch/Flemish bond (also very popular in Poland) was applied so the longitudinal joint was formed in every second layer.

The shape, dimensions and the view of both types of test specimens ready for testing are shown in Fig. 1.

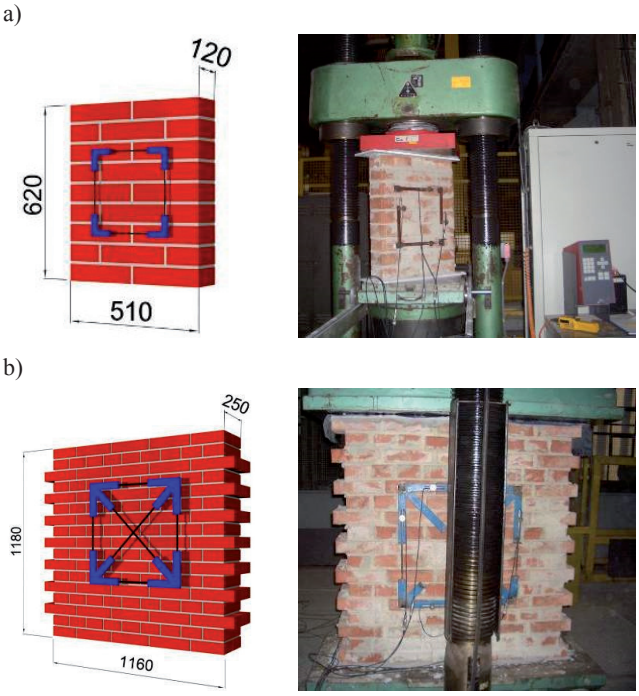

Fig. 1. The shape, dimensions and view of both types of specimens ready for testing: a) type **CV**; b) type **MW**

Measuring frames with inductive (LVDT) sensors for the purposes of measuring deformations to an accuracy of 0.0002 mm were located on both sides of each masonry specimen. The dimensions of a frame, recording vertical and horizontal deformations, were equal to 300 × 300 mm in case of **CV** models and 600 × 600 mm in case of walls **MW**.

The tests of the **CV** type masonry wallettes (smaller specimens) were performed using a hydraulic press machine with a 2000 kN range capacity while the tests of the **MW** masonry walls were carried out using a hydraulic press machine with a maximal range of 6000 kN. Before placing the specimens in the press machine, both top and bottom surfaces of each specimen were levelled with a cement mortar. To eliminate friction between the surfaces of the steel heads of the machine and the specimens' surfaces, special pads were used: 10 mm Teflon pads for the **CV** series specimen and a double layer of polyurethane foil with graphite grease between the layers for the **MW** series specimens.

Three of the six **CV** series specimens and five of the six **MW** series wallettes were cyclically loaded with the load increasing in each cycle. The rest of the specimens were used as reference members and were loaded in one cycle. The loading history for the cyclically compressed masonry is presented in Fig. 2.

The load ratio during all tests was equal to 2 kN/s. The first level of load for the **CV** series masonry specimens was equal to 50 kN and was then increased by 50 kN in each cycle. The first level of load for the **MW** series walls was equal to 300 kN, then 600, 900 and 1200 kN, in the next cycles, this was stepped up by 150 kN until failure. For each cycle, the load was sustained for ~3 minutes in order to stabilise the state of deformations.

a)

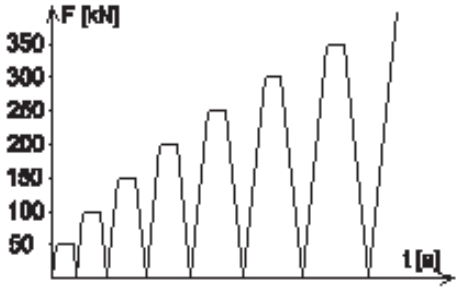

b)

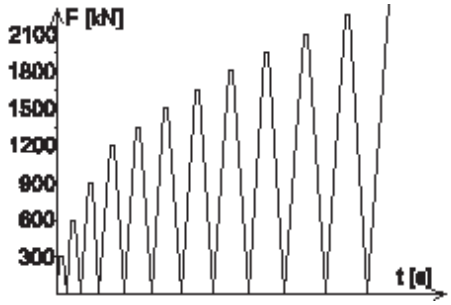

Fig. 2. Loading history for specimen testing: a) **CV** series; b) **MV** series

Table 1

Exemplary failure patterns

Series	One cycle loading		Cyclic loading	
	side A	side B	side A	side B
CV	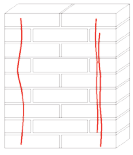	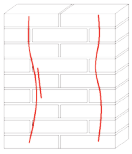	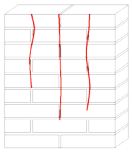	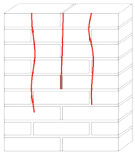
	CV-d-2		CV-c-2	
MW	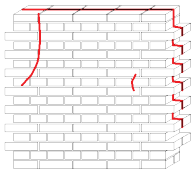	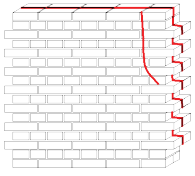	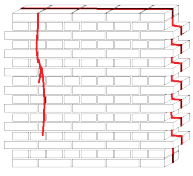	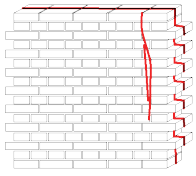
	MW-d		MW-c-1	

3. Test result and discussion

3.1. Modes of failure

Significant differences between modes of failure of specimens loaded cyclically and those loaded in one cycle were not observed. Exemplary sketches of failure (crack) patterns of masonry wallettes representing both series and both types of loading are shown in Table 1. All tested elements (**MW** and **CV** series) failed in a similar manner independent of the mode of loading (cyclic or in one cycle). In Fig. 3, an exemplary failure of **MW** series masonry wallettes as well as the **CV** series are presented.

a) b)

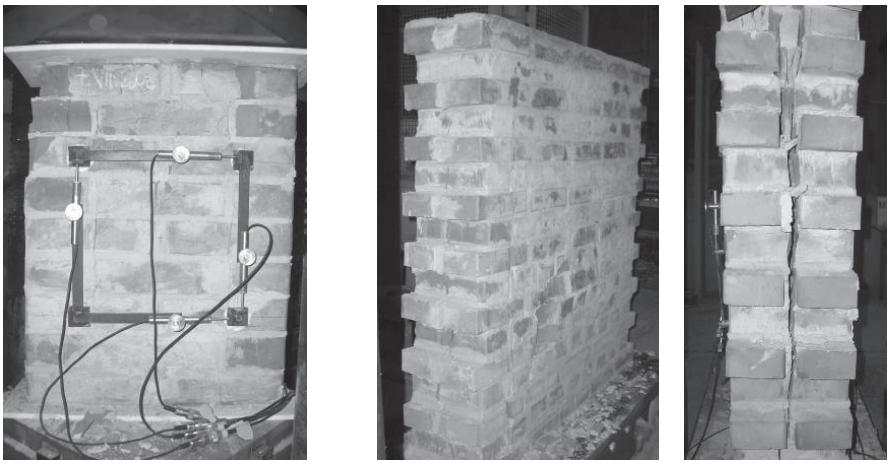

Fig. 3. Failure of: a) **CV** type model; b) **MW** type model

The failure was caused by the formation of a few cracks oriented perpendicularly to the bed joints which divided the specimen into a few independent columns, see Fig. 3. In case of the wallettes with a thickness of one brick (**MW** series), splitting in the plane of a longitudinal joint was additionally observed. The cracking parallel to the face surface of the wall divided the specimen into two independent wall plates as is shown in Fig. 3b.

3.2. Main results

The main results of the investigations, which include cracking stresses σ_{cr} (corresponding to the first crack appearance), ultimate stresses σ_u and corresponding strains ε_{cr} and ε_u, are presented in Table 2. The average values of strains ε_{cr} and ε_u were determined based on the data recorded by four LVDT sensors. In the sixth column of Table 2, the correlation between σ_{cr} and σ_u stresses is shown. The last column displays the number of cycles at which the point of failure war reached for each tested specimens (including reference members loaded in one cycle).

The first cracks in the small specimens with thicknesses of 1/2 of a brick (**CV** type) appeared at the σ_{cr} stress level of 6.52–7.34 N/mm^2. The value of the ultimate stress at failure for these panels was similar and ranged from 11.85 to 14.92 N/mm^2. An increase in the cracking strain ε_{cr} and ultimate strain ε_u of the cyclically loaded wall with respect to elements loaded in one cycle was observed (by 9% and 17% respectively).

In larger walls (**MW** series), the first cracks in cyclically loaded elements appeared at the stress level of 4.78–6.15 N/mm^2, while in monotonically loaded wallettes the first cracks were observed at a slightly higher level of stress, 6.38 N/mm^2. The value of the ultimate stress at failure was similar for all tested specimens of this type and ranged between 8.67 and 10.71 N/mm^2. Analogically to the elements in the **CV** series, it was observed that the ratio

between the cracking stress, σ_{cr}, and the ultimate stress, σ_u, was quite similar. The value of the ultimate strain in the wallette loaded in one cycle was only slightly smaller than in the specimens subjected to cyclic loading.

The number of cycles was similar for all masonry walls subjected to repeating load. It seems that shape and overall dimensions as well as the existence of longitudinal joints at every second level, as in the case of **MW** series specimens, have no influence on the number of cycles required to reach the point of failure for masonry wallettes subjected to uniaxial compression.

Table 2

Main results of investigations

Test specimen	σ_{cr} [N/mm^2]	σ_u [N/mm^2]	ε_{cr} [ε_u 10^{-3}]	ε_u [$\times 10^{-3}$]	σ_{cr}/σ_u	Number of cycles
CV-d-1	6.83	13.14	0.92	2.61	0.52	1
CV-d-2	7.31	14.92	0.94	2.54	0.49	1
CV-d-3	6.98	13.98	1.02	2.63	0.50	1
CV-c-1	6.52	12.48	0.94	2.89	0.52	16
CV-c-2	7.34	14.57	1.04	3.29	0.50	18
CV-c-3	7.11	11.85	1.16	2.91	0.60	15
MW-d	6.38	10.42	1.03	2.35	0.61	1
MW-c-1	5.55	9.94	0.90	2.5	0.56	15
MW-c-2	5.48	9.36	1.01	2.65	0.59	14
MW-c-3	6.15	10.71	0.93	2.47	0.53	16
MW-c-4	4.78	8.67	0.77	2.45	0.55	13
MW-c-5	5.96	9.89	0.97	2.71	0.60	15

3.3. Failure envelope

The results of cyclic tests allowed defining a failure envelope of the stress–strain relationship. The envelope is created by connecting points of the maximum strain in each cycle. A typical σ–ε relationship for masonry subjected to cyclic loading with the envelope is presented in Fig. 4.

To eliminate the material and strength differences, further comparison of results was performed with normalized $\sigma_i/\sigma_{max,i} - \varepsilon_i/\varepsilon(\sigma_{max})$ relationships. Averaged normalised failure envelopes for the **CV** and **MW** masonry walls are shown below in Fig. 5.

It was observed that in the high initial range of compressive stresses (up to ~0.7 σ_{max}) for masonry with a half-brick thickness (**CV** series), the resultant relationships are linear which signifies near-elastic behaviour of the masonry. For specimens with a thickness of 1 brick (**MW** series) up to a level of ~30% of σ_{max} (first visible crack appearance), the diagrams have a distinctly curvilinear character (non-linear elastic behaviour of the material) and then, in the range from 30% to ~75% of σ_{max} (rapidly increasing plastic-brittle damage deformations), fracture development stabilises at the similar level and the diagrams have a more or less

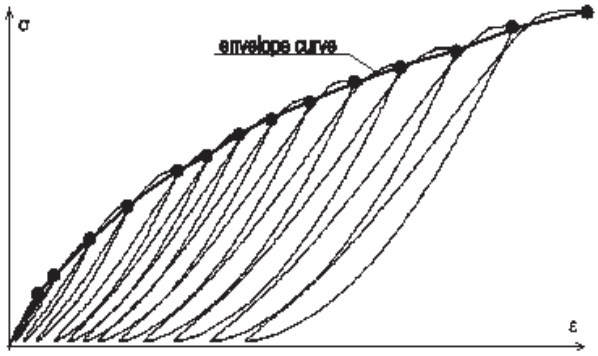

Fig. 4. Typical σ–ε relationship for masonry subjected to cyclic loading with the construction of the envelope curve

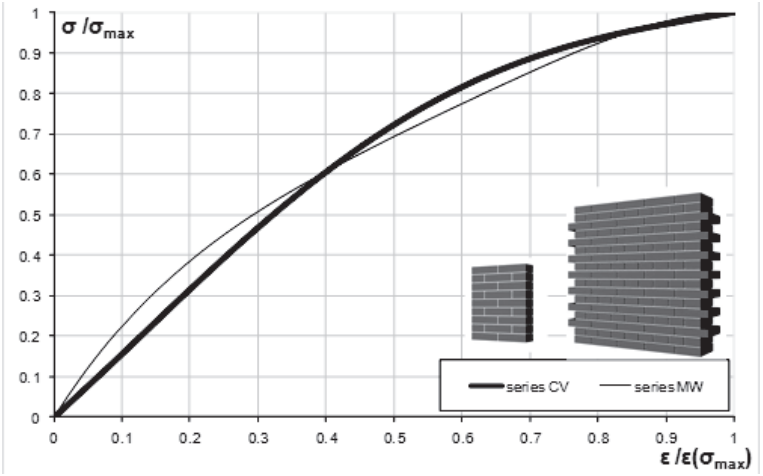

Fig. 5. Averaged normalised envelopes for **MW** and **CV** series models

linear character. This can be explained by the fact that in the **MW** series masonry walls, there is an unbounded longitudinal joint located at every second layer in the axis of the wall which has an effect on the behaviour of that wall. When stresses exceed the value of 75% of σ_{max}, the process of fracture and disintegration of the material is very quick, leading to failure.

Describing the curves with fourth-order polynomials, the following proposed formula was used:

$$\frac{\sigma}{\sigma_{max}} = a \cdot \left(\frac{\varepsilon}{\varepsilon(\sigma_{max})} \right)^4 + b \cdot \left(\frac{\varepsilon}{\varepsilon(\sigma_{max})} \right)^3 + c \cdot \left(\frac{\varepsilon}{\varepsilon(\sigma_{max})} \right)^2 + d \cdot \frac{\varepsilon}{\varepsilon(\sigma_{max})} \tag{1}$$

where a, b, c, d are polynomial coefficients (determined values are specified in Table 3).

Table 3

Constant coefficients of **polynomial function**
$\boldsymbol{\sigma/\sigma_{max,i} - \varepsilon/\varepsilon(\sigma_{max,i})}$ for eq. (1)

Series	Values of constant coefficients			
	a	*b*	*c*	*d*
MW	–2.17	5.00	–4.47	2.64
CV	1.16	–2.52	0.87	1.49

The next diagram (Fig. 6) presents $_i/\sigma_{max,i} - \varepsilon_i/\varepsilon(\sigma_{max,i})$ relationship for the one cycle tests (continuous line) and the failure envelope obtained from the cyclic tests (dashed line) for the **CV** and **MW** masonry walls series.

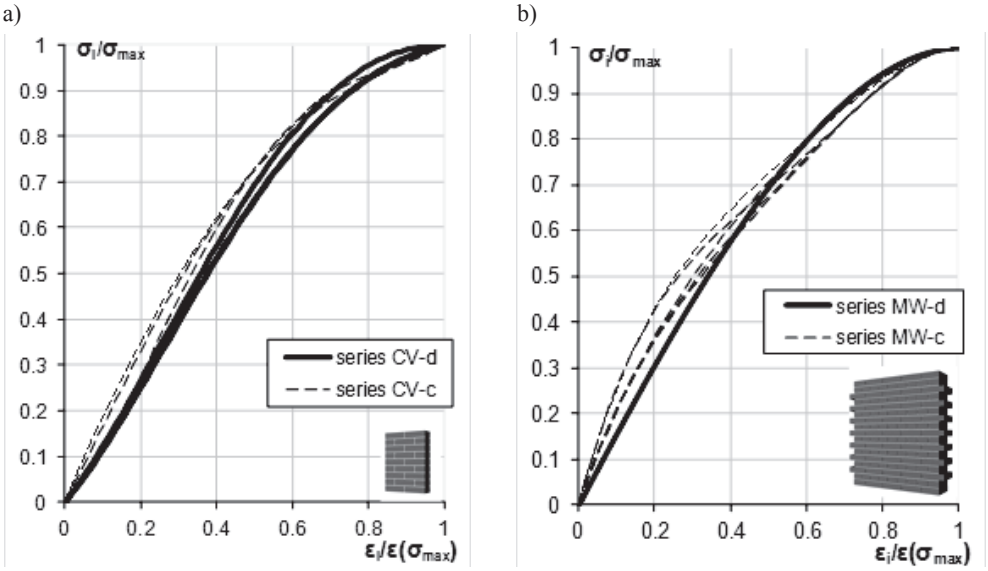

Fig. 6. Normalised $\sigma_i/\sigma_{max,i} - \varepsilon_i/\varepsilon(\sigma_{max,i})$ relationships for: a) **CV**, b) **MW** series models

It was observed that the characteristic obtained from the monotonic tests, both for the **CV** and **MW** series elements, differs significantly from the envelope of the cyclically loaded elements – it has a linear characteristic over a greater range than in the case of monotonically loaded masonry walls. The curves obtained in the cyclic tests show that at the level of ~30% of the ultimate stress softening or even local depletion of load-bearing capacity is observed in the areas where brittle fracture occurred. In the subsequent cycles, non-elastic strains develop.

3.4. Loading curves

Knowledge of σ–ε loading curves in cyclic compressive loading allows evaluating the damage intensity of the structures. Exemplary σ–ε relationship for the loading curves of the masonry walls with a one-brick thickness (**MW-c-1**) is shown in Fig. 7. The dashed line corresponds to the cycle when the first cracks were appeared. Based on this figure, the value of strains related to cracking stresses σ_{cr} (values given in column 2 of Table 2) is ε_{cr} (values shown in column 4 of Table 2). After unloading, the residual value of strain amounted to $\varepsilon_{cr,r}$. In the following loading cycles the value of residual strains clearly increased while the values of initial modulus of elasticity (tangent of the angle of stress-strain relationship $E_i = (\Delta\sigma_i/\Delta\varepsilon_i)$, determined for each cycle from the stress range 0 to $1/3\sigma_{max,i}$) decreased systematically.

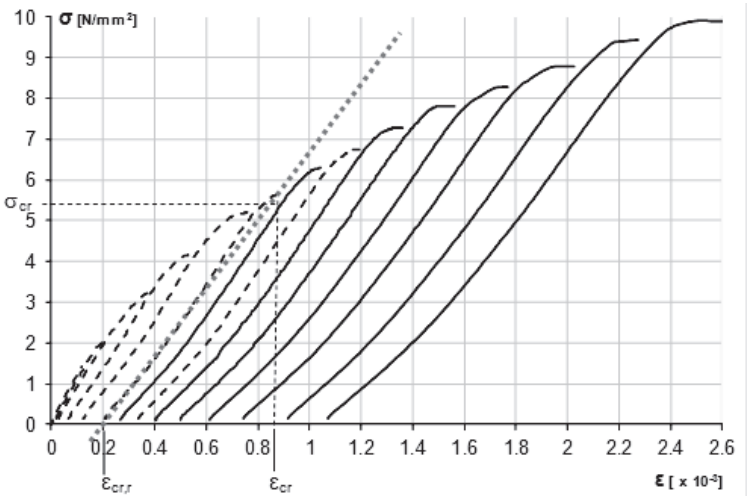

Fig. 7. Normalised $\sigma_i/\sigma_{max,i} - \varepsilon_i/\varepsilon(\sigma_{max,i})$ relationships for: a) **CV**, b) **MW** series models

The shape of the loading curves for the **MW** series changes with the developing degradation of the masonry walls. The curves before cracking have different characteristics that the curves after cracking. The phenomenon of the curvature change during the process of cyclic loading was not observed in the masonry walls with half-brick thickness.

Graphical interpretation of the normalised loading curves for both types of tested specimens is presented in Fig. 8.

The loading curve for the **MW** masonry walls before cracking clearly has a linear-elastic character whereas the loading curve after cracking is a concave curve. In the cracked material, relaxation is observed when the element is unloaded. During the following loading cycle, firstly, the existing damage is compressed and the cracks are closed. The change of the curve from concave to convex is observed if such material starts to behave as new, undamaged material. A hardening effect is then observed. This phenomenon was observed only in the case of **MW** series wallettes. It is probably also connected with the existence of an internal longitudinal crack at every second level of the wallette. Horizontal tensile stresses

in a direction perpendicular to the plane of the specimen produced by vertical compressive loads generated the internal cracks and local damage. Therefore, the degradation process is more distinct.

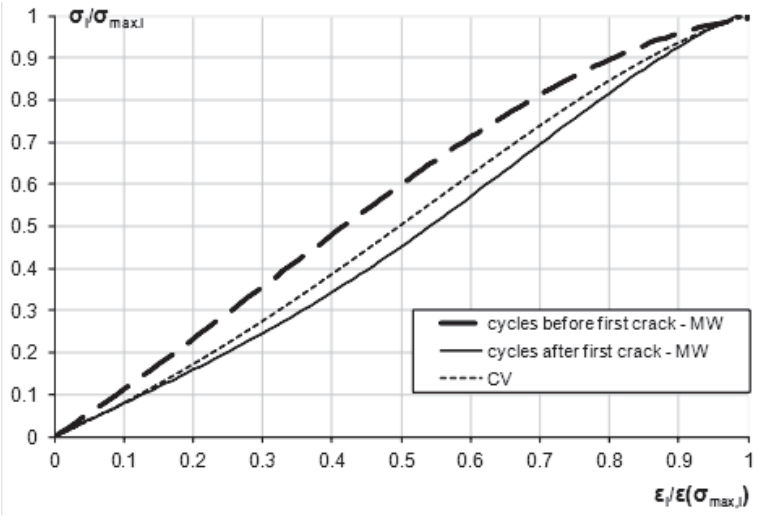

Fig. 8. Normalised loading curve $\sigma_i/\sigma_{max,i} - \varepsilon_i/\varepsilon(\sigma_{max,i})$

There was no need to group the loading curves into curves before and after cracking for the half-brick thick masonry wallettes (**CV** series); σ–ε loading curve was well described for all cycles by a single relationship. Graphically, the loading curve for the **CV** series lies between the curves for the **MW** series. Its shape is close to linear – strains increase proportionally to stresses.

3.5. Discussion of results

Figure 9 presents a comparison of envelope curves of cyclic tests performed by the authors and the relationships obtained by other authors.

Differences between the presented curves can be observed. These differences are due to the use of different materials for construction of the wallettes as well as different dimensions of the testing elements.

Obviously, the wallettes made with the use of wedging elements (as was the case in external research examples) will exhibit a higher load-bearing capacity than the wallettes made from bricks without a mechanical wedge. The envelope curves obtained in the tests of the wallettes with small-size self-wedging elements are located above the analogical curves obtained for the full-brick wallettes.

Moreover, as was the case in the **MW** series wallettes, the use of the longitudinal joint significantly weakens the wallette. Lower values of stresses cause higher strains in comparison to the wallettes without an internal joint.

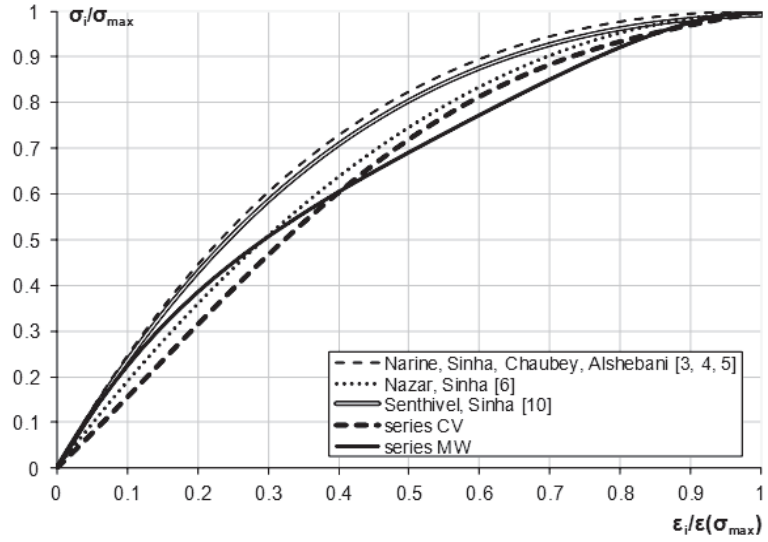

Fig. 9. Normalised $\sigma_i/\sigma_{max,i} - \varepsilon_i/\varepsilon(\sigma_{max,i})$ relationships for own and external research

In general, based on the presented diagram it can be stated that the cyclic-load envelope curve has two forms: before cracking and after cracking. Before cracking, its course is more linear (except for the **MW** series, which was discussed in 3.3). After reaching cracking stress level, a change of curvature can be observed due to the degradation of the wallette caused by cracking and damage.

5. Summary and conclusions

The paper presents the results of laboratory tests of 12 masonry wallettes subjected to compressive loading. The walls differed in shape, overall dimensions and loading scheme. Based on the results of the presented tests and analytical analyses, the following conclusions may be formulated:

- the values of the cracking strain, ε_{cr}, and the ultimate strain, ε_u, of cyclically loaded masonry walls are greater than the values obtained for monotonic loading tests;
- the values of the cracking stresses, σ_{cr}, and the ultimate stresses at failure, σ_u, do not depend on the loading scheme;
- σ–ε relationship for masonry wallettes loaded in one cycle is different than the envelope obtained in cyclic loading: the character of the envelope of σ–ε curves for the cyclically loaded elements is considerably more non-linear than the character of this envelope for the monotonically loaded elements;
- the characteristic of the σ–ε loading curve allows describing the evaluation of damage intensity of the structure;

– in the case of masonry walls with an internal joint (**MW** series), the shape of the loading curve changes due to the progressive degradation of masonry during cyclic loading;
– the proposed mathematical description of the envelope curve does not have a universal character due to the limited number of tested specimens and using only one type of masonry units and mortar, further investigations, both experimental and analytical are necessary.

References

[1] Kaushik H., Rai D., Jain S., *Stress-Strain Characteristics of Clay Brick Masonry under Uniaxial Compression*, Journal of Materials in Civil Engineering, ASCE, Vol. 19, No. 9, 2007, 728–739.

[2] Karsan J., Jersa J., *Behavior of Concrete Under Compressive Loading*, Journal of Structural Division, ASCE, Vol. 95, No. 12, 1969, 2543–2563.

[3] Naraie K., Sinha S., *Behaviour of Brick Masonry Under Cyclic Compressive Loading*, Journal of Construction Engineering and Management, 1989, 1432–1445.

[4] Chaubey U., Sinha S., *Cyclic compressive loading response of brick masonry*, Journal of Masonry International, Vol. 4, No. 3, 1991, 94–98.

[5] Alshebani M., Sinha S., *Stress- Strain Characteristics of Brick Masonry Under Uniaxial Cyclic Loading*, Journal of Structural Engineering, Vol. 125, No. 6, 1999, 600–604.

[6] Nazar M., Sinha S., *Mathematical model for loading/unloading stress-strain curves of interlocking brick masonry*, Proc. 7th International Masonry Conference, London 2006.

[7] Alshebani M., *Permissible Stress Level of Brick Masonry under Compressive Cyclic Loading*, Journal of Civil Engineering and Architecture, Vol. 7, 2013, 153–157.

[8] Narin K., Sinha S., *Loading and Unloading Stress-Strain Curves for Brick Masonry*, Journal of Structural Engineering, 1989, 2631–2644.

[9] Alshebani M, Sinha S., C*yclic compressive loading unloading curves of brick masonry*, Structural Engineering and Mechanics, 1999, 375–382.

[10] Senthivel R., Sinha S., *Behaviour of Calcium Silicate Brick Masonry Under Cyclic Uniaxial Compression. Masonry*, Proc. 6th International Masonry Conference, Vol. 9, London 2002, 412–422.

[11] EN 1052-1:2001 Methods of test for Masonry – Part 1:Determination of compressive strength.

TECHNICAL TRANSACTIONS | CZASOPISMO TECHNICZNE
CIVIL ENGINEERING | BUDOWNICTWO
3-B/2015

PIOTR GWOŹDZIEWICZ*

THE APPLICABILITY OF SHAPE MEMORY ALLOYS IN STRUCTURES

O MOŻLIWOŚCIACH WYKORZYSTANIA STOPÓW Z PAMIĘCIĄ KSZTAŁTU W BUDOWNICTWIE

Abstract

The structural application of shape memory materials is relatively new. It is possible that these materials provide the unusual property of creating stress in steel bars in a thermomechanical way. Depending on the alloy composition and production treatment, the characteristic transformation temperatures as well as the mechanical properties of the material vary and this may limit its technical effectiveness. The present work is focused on the material parameters from the point of view of practice.

Keywords: *shape memory alloys; prestressing; concrete members*

Streszczenie

Zastosowania konstrukcyjne materiałów z pamięcią kształtu są stosunkowo nowe. Materiały te mogą prezentować nietypową właściwość wywoływania naprężeń w prętach stalowych wskutek reakcji termomechanicznej. Charakterystyczne temperatury przemian fazowych, a także właściwości mechaniczne stopu zależą od jego składu oraz procesu produkcji, co może mieć wpływ na techniczną efektywność materiału. Niniejsza praca dotyczy cech materiałów z pamięcią kształtu z punktu widzenia praktycznych zastosowań.

Słowa kluczowe: *materiały z pamięcią kształtu; sprężenie; elementy betonowe*

DOI: 10.4467/2353737XCT.15.163.4338

* Ph.D. Eng. Piotr Gwoździewicz, Cracow University of Technology, Faculty of Civil Engineering.

1. Introduction

The cracking of construction materials is one of the major weaknesses which influence the durability of structures. The effect of local failure is irreversible regardless of the direct reason for damage, compression or tension, and also regardless the formulation – stress or strain. Concrete fails usually under tension, but high compression may also provoke cracks in the direction of the load. As well as other materials, masonry also shows cracks as a result of loads and deformations.

In order to limit the negative effect of cracks, various methods of reinforcing structural members are used. Steel reinforcing bars or steel profiles in concrete are passive – stress in this material appears only under an acting external load. Prestressing tendons are used successfully as active reinforcement in members of long spans or in members under high loads. In recent years, in addition to prestressing steel, new materials are also used for similar purposes – as fiber reinforced composite materials and shape memory alloys (SMA).

Particular properties of the SMA materials (memory effect and super elasticity) are used in medicine, aviation and mechanisms. Wide research has been carried out in the last 20 years in the scope of civil engineering applications. The advantages of such solutions are related to high corrosion resistance and the damping effect, but the main reason for research is investigating the effect of provoking tension in material in a thermo-mechanical as opposed to a mechanical manner. The number of successful applications, where the appropriately prepared tendons made of shape memory alloys are used, is increasing. Such tendons are installed in the structural member and after the activation of the thermomechanical effect they start to act with the internal forces. This proves the important possibilities related to the use of such material in building practice. Based on the existing information, it is possible to estimate the boundary parameters for such applications.

In order to describe the potential benefits from such applications, the most important characteristic parameters for the SMA materials are reported below. A selection of the results known from both the bibliography and local tests, including a quantitative description, completes the work.

2. SMA materials

Alloys which demonstrate the shape memory effect are composed of various metals. The name SMA is most commonly associated with nickel-titanium alloys – these are used widely in medicine i.e. as implants and in aeronautics. Other alloys are composed of cuprum, cadmium, zinc, aluminum, iron or manganese. Extensive descriptions of various compositions were published by Otsuka & Wayman ([1]).

2.1. Shape memory effect

The shape memory effect is commonly understood as strain recovery. In fact, SMA material may represent large initial deformation which is further recovered in effect of

heating. The process is related to the transformation of the material between the austenite and martensite phases and governed by two key parameters: temperature and stress. The transformation process for a given alloy is formulated in the form of the transformation temperatures: A_s – temperature of the start of alloy transformation from the martensite to the austenite phase; A_f – temperature of the transformation finish from the martensite phase to the austenite phase; M_s – temperature of the start of alloy transformation from the austenite phase to the martensite phase; M_f – temperature of the transformation finish from the austenite phase to the martensite phase. Characteristic temperatures are usually measured for the given alloy at zero stress. Stress increase in the material results in the progressive increase of all transformation temperatures. The diagram shown in the Fig. 1 represents the fundamental formulation of the phase transformation.

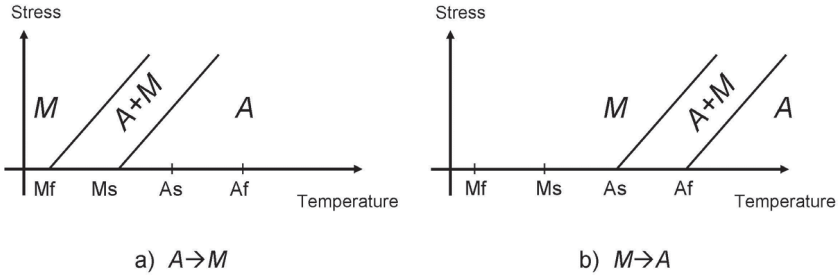

Fig. 1. Characteristic temperatures of the phase transformation for the shape memory alloys: a) – transformation from martensite to austenite, b) – transformation from austenite to martensite (description in text)

For any given alloy of two or more components, there are two principal parameters influencing the final properties of the material. The first of these is the proportion of different metals in the given alloy. Various results confirm that any variation of the proportions of a grade as small as 0.1% influences the transformation temperatures to a significant degree. The other is the alloy treatment after it melts. There are two technological solutions used: cold-working or hot-working processes. The influence of the working process on the mechanical parameters of the alloy is not negligible.

2.2. Mechanical and shape memory properties of SMA materials

Several mechanical properties are required to be estimated for the sake of the structural applications of the materials. As may be observed from the available data, NiTi alloy behaves in compression differently to tension (Otsuka & Wayman [1], Manach & Favier [2]).

Although the results were obtained for various materials, the general tendency is evident – the mean value of the modulus of elasticity in the martensite phase falls for tension values of around 34 GPa and for compression values of around 50 GPa. In the austenite phase, the mean values are 60GPa and 64GPa.

The yield limits for alloys under tension and compression present more important variations. In the martensite phase, under tension the mean yield limit is reported at 175 MPa,

while the limit for compression is at 158 MPa. For the austenite phase, the yield value for tension is at 450 MPa, and for compression it is at 675 MPa.

The differences between the ultimate strength levels for both phases are much lower. For martensite under tension, the mean value is 1400 MPa and under compression, it is 1960 MPa. For austenite in tension – 1350 MPa and in compression – 1500 MPa. This means that the plastic behaviour of one of the two metallurgic forms of the material is largely different from the other – the ultimate stress at rupture is related more uniformly to the composition of the alloy. Table 1 provides the above mentioned values together with their tolerances.

Although the variation of the reported data is related partly to the alloy composition, it is necessary to underline that even for the material coming from the same production with identical chemical composition but formed in two different diameters, the mechanical properties are different. This is related to the technology used to form the wire. For structural applications, this means that the tensile strength is generally profitable – a low modulus of elasticity will limit the influence of the SMA reinforcement on the cross-section rigidity, but in any case, material testing in the final shape is required to measure its real properties.

From the range of parameters describing the memory effect demonstrated by the material, the recovered pseudo elastic strain and maximum recovery stress are important. These two parameters remain dependent from each other. For the stress recovery predeformation must be applied to the material and further results depend on it. Recovered pseudo elastic strain is generally higher than it is for conventional steel and reaches a level of 80‰ in tension as well as 60‰ in compression. The maximum recovery stress of even 800MPa for both directions of stress is the major argument confirming the potential effectiveness of SMA alloys in construction.

Table 1

Mechanical and shape memory properties of NiTi alloys

Direction of stress	Mechanical and shape memory properties	Martensite	Austenite
Tension	Modulus of elasticity [GPa]	34±18	60±35
	Yield limit [MPa]	175±125	450±350
	Ultimate strength [MPa]	1400±600	1350±550
	Recovered pseudo-elastic strain [‰]	80	
	Maximum recovery stress [MPa]	800	
Compression	Modulus of elasticity [GPa]	50±30	64±34
	Yield limit [MPa]	158±33	675±125
	Ultimate strength [MPa]	1960±160	1500
	Recovered pseudo-elastic strain [‰]	60	
	Maximum recovery stress [MPa]	800	

The values of the mechanical properties given above and in Table 1 represent an important scatter reflecting, amongst other parameters, the influence of the precise alloy composition. It therefore seems necessary to establish the characteristic parameters of the given alloy before further analysis of its participation in the structural work carried out. In further research, it should be considered whether the mechanical and shape memory properties are regularly related to the alloy composition. Nevertheless, the values confirmed with the tests show the potential opportunities related to the use of SMA materials in practice. Jank et al [3] presented the existing successful applications.

3. Application temperatures

From the point of view of practical applications, the precise estimation of transformation temperatures is of fundamental importance. The successful and durable introduction of internal forces in structural members may be ensured only if service conditions do not provoke changes of the material phase. As can be observed from the available data, transfer temperatures vary in relation to other conditions even for the same alloy proportions. In the following figure (Fig. 2), exemplary values of the transformation temperatures estimated in tests are presented. For the eleven tested NiTi alloys, the diagram shows the range of the following phases: martensite (A); transformation from martensite to austenite (B); between martensite start and austenite start (C); transformation from martensite to austenite (E); austenite (F). The violet range (D) for alloy 1 is characteristic for the alloy, where the temperature of the martensite start is higher than the temperature of the austenite start. Comparisons of the alloy parameters were reported by Hesse et al. [4] (alloys 1 and 2), Strnadel et al. [5] (alloys 3, 4 and 5), Manach & Favier [2] (alloy 6), Delgadillo-Holtfort et al. [6] (alloy 7), Destrebecq [7] (alloy 8) and Debska [8] (alloys 9, 10 and 11).

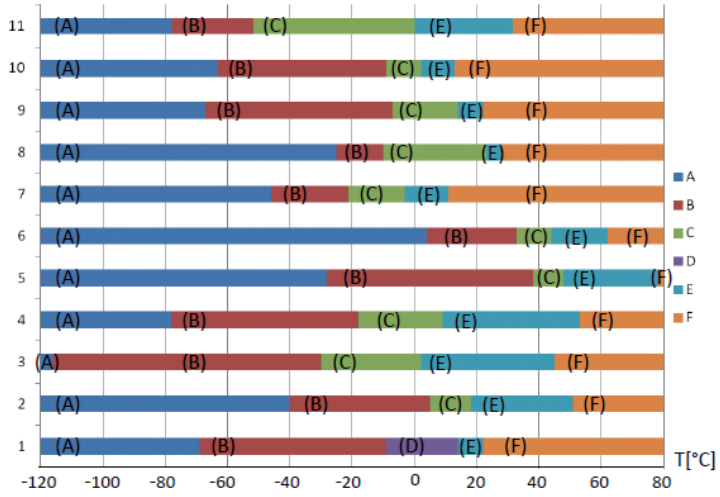

Fig. 2. Transformation temperatures for shape memory NiTi alloys (description in text)

An evident observation from the diagram is that depending on the alloy, the temperature of its potential use may vary substantially. On the other hand, for the given potential application, only a part of the available material will be suitable. For common temperatures during winter periods, which drop to –20°C, only some of the compared materials will not start the transformation from the austenite phase to the martensite phase, while the others will show a progressive decrease of the stress provoked by the shape memory effect.

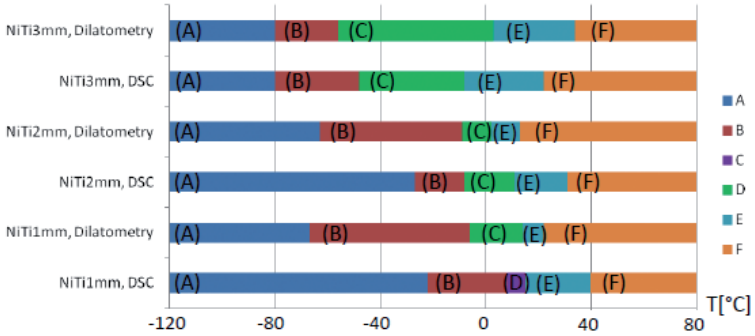

Fig. 3. Influence of the testing method on the estimation of the transformation temperatures (description in text)

An additional comment to the diagram in Fig. 2 refers to the reliability of the results of the transformation temperatures reported by the producers. Transition temperatures are estimated through the use of one of the two most popular procedures: differential scanning calorimetry DSC and dilatometry. The first of these methods is the more popular amongst producers, who supply the results of testing based on heat-flow scanning in the form of a diagram. Transformation temperatures are estimated using the intersection points of the tangent lines in the diagram. In the other method, material volume changes as the characteristic effects of phase transformation are observed. Both methods may give non-consistent results, as reported by Debska [8]. Fig. 3 shows a diagram built with use of the values based on the both methods. As may be observed in the diagram, transfer temperatures estimated using the dilatometry approach are higher. This is of importance for practical applications, where the transfer from austenite to martensitic in normal ambient conditions will eliminate the stress provoked by the shape memory effect. Shifting of the transformation temperatures for the alloy towards higher temperatures in effect of existing stress will additionally increase the risk of material transformation.

3. Stress-strain relationship

Beside the transformation process, the mechanical behaviour of the alloys is of interest due to their practical use. The stress-strain relationship built for the material will differ depending upon the phase at the beginning of the test. It is generally understood that the

whole constitutive relationship will be shown properly if the test is starting from the austenite phase. An increase of stress from zero level will initially trigger a semi-elastic response from the alloy, followed by plastification and a yield-plateau. After phase transformation, the modulus of elasticity increases; finally the material reaches another plastification stress level and at increasing stress shows plastic deformation followed by rupture. The typical shape of the stress-strain diagram for the shape memory alloy is shown in Fig. 4.

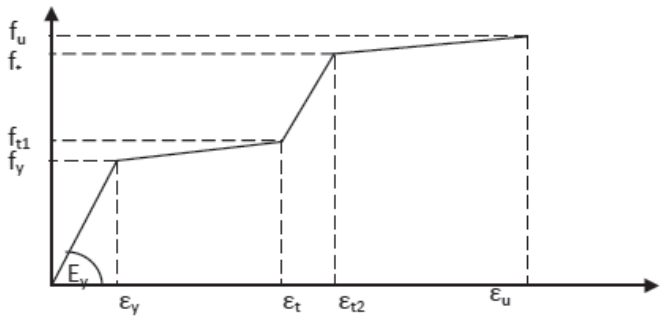

Fig. 4. Stress-strain relationship for SMA material

The Fig. 4 diagram follows the material behaviour under an increasing load starting from the austenitic phase. In the diagram, two sub-diagrams showing the behaviour for a metal are observed. Firstly, the material in the austenite phase shows a relatively high modulus of elasticity which drops after reaching the yield stress and strain, f_y and ε_y. After reaching a new limit of strain ε_t, phase transformation to martensitic material takes place and a stiffening effect represented by the higher inclination of the diagram line is observed. However, in this section sub-diagram the inclination of the line representing the modulus of elasticity is lower than in the first one. Finally, after reaching the second yield limit f_t, material stress increase slows down and ultimate stress f_u is reached.

From a practical point of view, this observation is important as the modulus for the martensitic phase is lower than the modulus for the austenite phase, while the modulus for the austenite phase is usually reported as the material characteristic value. In the conventional approach to the concrete members analysis, this means that the SMA reinforcement will be much less effective than passive reinforcement.

4. Conclusions

The mechanical characteristics of the shape memory materials depend on numerous parameters. From the point of view of practical use, it should be considered that:

– the mechanical parameters and transformation temperatures of the SMA alloys depend on the alloy composition and its treatment method during production;

– the application temperature should be in agreement with the transformation temperatures estimated for the given alloy with precision – for small diameters, the dilatometry method gives more reliable results;
– the temperature of the transformation should be corrected in order to account for the stress influence;
– structural applications should be analysed taking into account the whole stress-strain constitutive relationship and not only to a single value of the modulus of elasticity.

The promising properties of the SMA alloys require further research in order to establish more regular information on different aspects of its variation.

References

[1] Otsuka, K., Wayman, C.M., *Shape-memory materials*, Cambridge University Press, Cambridge 1999.
[2] Manach P.-Y., Favier, D., *Shear and tensile thermomechanical behaviour of near equiatomic NiTi alloy*, Materials Science and Engineering, No. 222, 1997, 45–57.
[3] Jank L., Czaderski C., Motavalli M., Ruth J., *Application of shape memory alloys in civil engineering structures – Overview, limits and new ideas*, Materials and Structures 38, 2005.
[4] Hesse T., Ghorashi M., Inman D.J., *Shape-memory-alloy in tension and compression and its application as clamping-force actuator in a bolted joint: part 1 – experimentation*, Journal of Intelligent Material Systems and Structures, No. 15, 2004, 577–587.
[5] Strnadel B., Ohashi S., Ohtsuka H., Ishihara T., Miyazaki S., *Cyclic stress-strain chatracteristics of Ni–Ti and Ti–Ni–Cu shape memory alloys*, Material Science and Engineering, No. 202, 1995, 148–156.
[6] Delgadillo-Holtfort I., Kaack M., Yohannes T., Pelzl J., Khalil-Allafi J., *Ultrasonic investigation of multistage martensitic transformations in aged Ni–rich Ni–Ti shape-memory-alloys*, Materials Science and Engineering, No. 378, 2004, 76–80.
[7] Destrebecq J.-F., Balandraud X., *Interaction between concrete cylinders and shape-memory wires in the achievement of active confinement*, Materials with complex behaviour, Advanced Structured Materials, Springer-Verlag Berlin Heidelberg 2010.
[8] Debska A., *Możliwość zastosowania materiałów z pamięcią kształtu do sprężania konstrukcji betonowych*, Thesis, Clermont-Ferrand 2014.

TECHNICAL TRANSACTIONS | CZASOPISMO TECHNICZNE
CIVIL ENGINEERING | BUDOWNICTWO
3-B/2015

PIOTR GWOŹDZIEWICZ*, ŁUKASZ JARNO **, JERZY PAMIN**

ACCOUNTING FOR TIME-DEPENDENT EFFECTS IN THE CONSTRUCTION STAGE FEM ANALYSIS OF COMPOSITE PRE-STRESSED BRIDGE GIRDERS

ZNACZENIE EFEKTÓW DŁUGOTRWAŁYCH W ANALIZIE ETAPOWANIA KONSTRUKCJI MES ZESPOLONYCH, SPRĘŻONYCH DŹWIGARÓW MOSTOWYCH

Abstract

In this paper, the results of the numerical analysis of pre-stressed concrete girders made of a high-strength concrete composite with a slab made of normal concrete are presented. A FEM analysis of the construction stage considering the influence of rheological effects on the behaviour of the structure was performed. Results of the analysis are presented in the work and are compared with the results of numerical analysis of the same elements, in which the time-dependent effects are not included. On the basis of these results, appropriate conclusions are proposed.

Keywords: *construction stages, finite elements method, prestressed concrete, rheology*

Streszczenie

W niniejszym artykule przedstawione zostały wyniki analizy numerycznej dźwigarów strunobetonowych wykonanych z betonu wysokiej wytrzymałości zespolonych z płytą pomostu wykonaną z betonu zwykłego. Przeprowadzono analizę etapowania budowy MES, uwzględniając wpływ efektów reologicznych na zachowanie się konstrukcji. Wyniki analizy przedstawione w pracy porównane zostały z wynikami analizy numerycznej tych samych elementów, w której efekty zależne od czasu nie zostały uwzględnione. Na podstawie otrzymanych wyników sformułowano odpowiednie wnioski.

Słowa kluczowe: *beton sprężony, etapowanie budowy, reologia, metoda elementów skończonych*

DOI: 10.4467/2353737XCT.15.164.4339

* Ph.D. Eng. Piotr Gwoździewicz, Institute of Materials and Civil Structures, Faculty of Civil Engineering, Cracow University of Technology.

** M.Sc. Eng. Łukasz Jarno, Ph.D. D.Sc. Jerzy Pamin, Institute for Computational Civil Engineering, Faculty of Civil Engineering, Cracow University of Technology.

1. Introduction

Nowadays, due to environmental issues and the forms of structures that architects design, there is a requirement for engineers to make greater efforts to analyse and design more sophisticated structural and material solutions. In the modern world of civil engineering, it is more often required to combine advanced concepts like composition, pre-stressing, high strength materials etc. with one another in order to meet high requirements for structures [1, 2]. Additionally, modern engineering pushes engineers to meet the requirements of durability and long-term serviceability in the structure. This is the reason why time dependent effects of concrete structures such as creep, shrinkage and the evolution of compression strength cannot be neglected and should be carefully considered at every stage of the design process.

The aim of this paper is to present a numerical model of a composite pre-stressed bridge girder. The prefabricated girder model is based on a slab model and two cases of construction stage analysis are considered in order to examine the influence of creep on the results. The model was calibrated and validated based on experimental studies carried out by Wonchang Choi (State University of North Carolina, Raleigh) [3], see Section 2. The basic parameters of the model such as geometry, strands configuration, boundary conditions and loads are described in Section 3. The results of the two analysis cases are shown in Section 4.

2. Experimental study

To evaluate the flexural behaviour of pre-stressed composite girders composed of high and normal strength concrete, nine twelve-meter long specimens were designed and tested. The concrete used for these girders was designed to have compressive strengths of 69, 97 and 127 MPa. All girders were designed based on the AASHTO LRFD codes, but some details were modified in order to prevent premature failure in shear or bond slip during flexural response. The tests were carried out for three girder types: first girder with 1.5 m wide NSC deck, second girder with 0.3 m cast deck and third girder without any deck cast on it. The deck was 200 mm thick and made from normal strength (28 MPa) concrete. The girders which were taken as a reference for the numerical approach were pre-stressed with sixteen straight 12.7 mm strands (1860 MPa low relaxation pre-stressing steel), material parameters of the pre-stressing strands were provided by the supplier with an average ultimate breaking strength of 194.6 kN. Fourteen strands were placed at the bottom flange and two were placed at the top. Each strand was tensioned up to 75% of its ultimate strength. All of the given results were divided into: material properties obtained from the experimental study; measured pre-stressing losses by using internal welded strain gauges; measured end slip used to determine transfer length; flexural response of the girders – flexural strength, cracking strength, load-deflection relationships, failure modes etc., for more details see [4].

For this kind of structure, taking into account the construction process (staging) and rheological behaviour of the material seems to be one of the most important aspects, especially when two different concretes (with different ages) are connected and are expected

to work together in one composite section. In this numerical approach, a FEM model is built and construction stage analysis is performed to evaluate the influence of the rheological behaviour of concrete during the staging process of the described structural member.

3. FEM numerical model

3.1. Geometry, material, loads and boundary conditions

The specimen is made of concrete with a compressive strength of 69 MPa and a modulus of elasticity of 36.9 GPa, represented in the computations by an elastic constitutive model. The girder is modelled using 8-node hexahedron solid elements with linear shape functions. The composite deck is made of concrete with 28 MPa compressive strength and 18.5 GPa modulus of elasticity. The rheological effects in the two different concretes are evaluated using CEB-FIP time-dependent material model [5]. The girder with a total length of 12.5 meters and distance between supports (span) of 12.2 meters is connected at the final stage to a slab with a 152.4 cm width and a 20.3 cm thickness. The connection of these two parts of composite girder for the preliminary test was assumed as rigid. The modelled girder has an 'I' shape cross-section with a 91.4 cm height, a 45.7 cm bottom flange width and a 30.5 cm top flange width (Fig. 1).

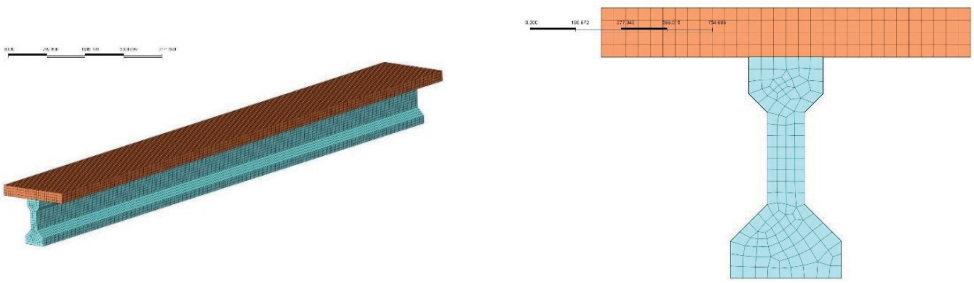

Fig. 1. Geometry of the modelled girder

Each tested girder contains Φ 4 mm stirrups with a spacing of 7.6 cm near the end blocks and 15.2 cm along the entire length of the girder. The longitudinal reinforcement is neglected due its negligible influence on the behaviour of the structure and lack of relevant data in the references. The stirrups are modelled as discrete bars embedded in the solid elements with full bond conditions between concrete and steel (Fig. 2).

The pre-stressing reinforcement of the girder contains sixteen straight strands, fourteen in the bottom flange and two in the top flange. Each particular strand is modelled separately using a bar in solid discrete reinforcement elements and a uniform pre-stressing force is applied. The girder is a simply supported beam. The supports with spacing of 12.2 meters were made of a steel plate above a neoprene pad. In the numerical approach, the supports were defined as rigid in a vertical direction which can have an influence on the results as the

model is stiffer than the real specimen. The load was applied to the girder with a MTS closed-loop actuator. The girder was loaded up to the yielding of pre-stressing strands and then to the point of failure. To examine the accuracy of the model, the cracking load obtained from experimental results is applied to the model as a pressure load according to the test set-up shown in Fig. 2. The total value of the load is 573.82 kN.

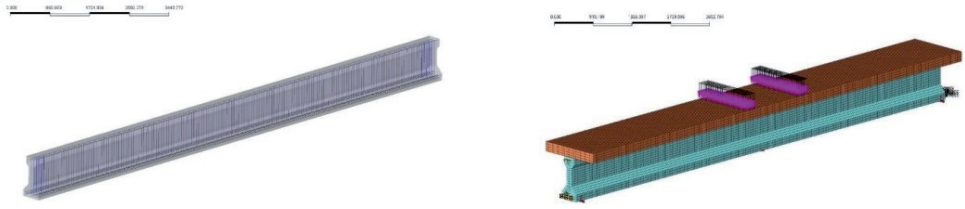

Fig. 2. Reinforcement, load and boundary conditions

3.2. Analysis cases

Construction stage analysis – the building process is divided into five stages: creation of the simply supported girder with reinforcement, pre-stressing of the girder, application of the wet concrete load, adding the newly cast slab to the composite girder, application of the external load. The staging analysis is performed with assumption of null time progress for a particular stage (stage duration time equals to zero), this means that no time-dependent effects are taken into account. This kind of analysis allows one to evaluate the influence of the building process divided in stages only in terms of the changing geometry and deformed shape from one stage to another.

Construction stage analysis with time-dependent effects – this type of analysis is performed to simulate the influence of the creep of concrete; however, the shrinkage phenomenon and compressive strength evolution in time are neglected in order to distinguish pure creep

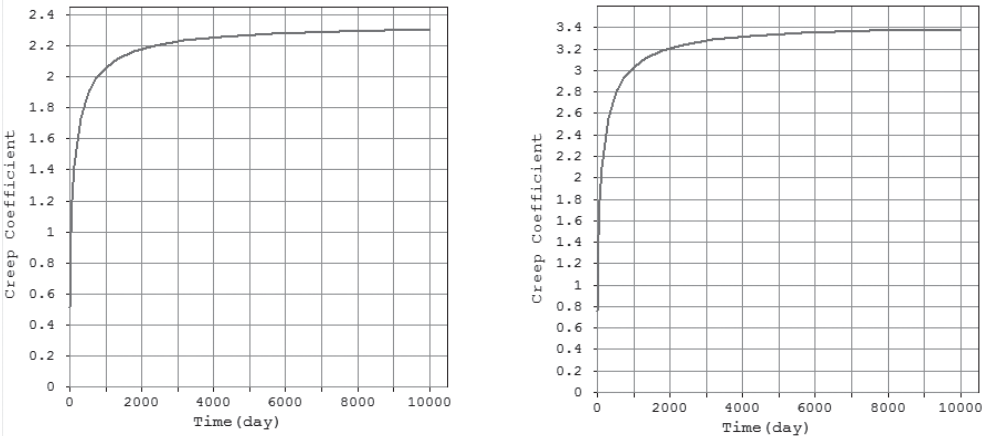

Fig. 3. HSC (a) and NSC (b) creep function

behaviour. Two different creep functions based on the CEB-FIP code recommendations [5] are introduced for HSC and NSC concretes (Fig. 3).

It is assumed that each stage has a seven-day duration and an additional sixth stage to reach the 10,000 days duration time of the whole process is introduced to show the long term behaviour.

4. Construction stage analysis results

The structure is completed in a number of construction stages. The configuration of the structure, loading, boundary conditions and physical properties of structural members change during the construction stages, especially when speaking about composite and additionally pre-stressed structures. If the structural system changes as the construction progresses, the real behaviour of the structure in the final stage may be different from that analysed without considering the staging. The analysis of the model is divided into 5 construction stages.

4.1. First stage – concrete girder with reinforcement

The first stage of constructing the modelled girder is treated as a 'virtual stage' to see the behaviour before pre-stressing. In reality, the strands are tensioned on the stressing bed and then concrete is cast – in the numerical simulation, it is not possible to model the strands first, but in the case of linear analysis, the Boltzmann superposition principle holds. In the first stage, only the self-weight load of the girder and steel stirrups is active. Fig. 4 shows the deflection of the girder with a maximum mid-span value of 2.5 mm.

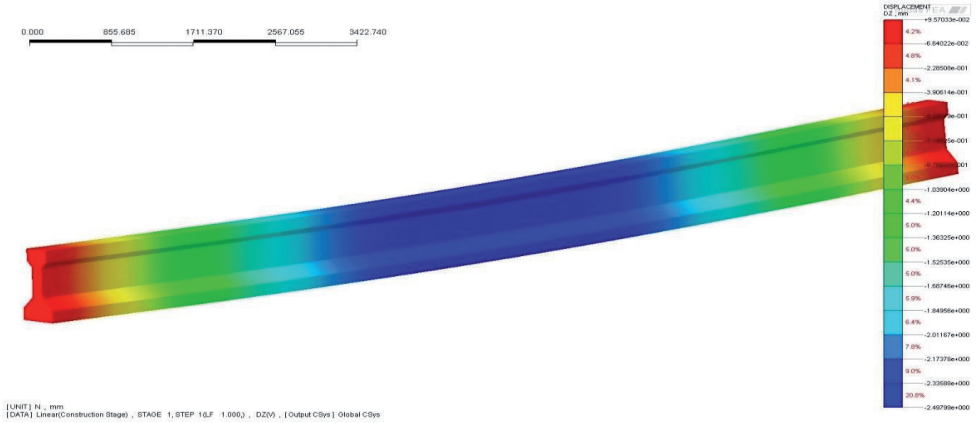

Fig. 4. Deflection of the girder in 'virtual' stage 1

In this stage, the maximum tension stress in the direction defined by the longitudinal axis of the girder is calculated as 2.38 MPa and the maximum compressive stress is 3.03 MPa.

4.2. Second stage – pre-stressing of the girder

In the second stage, pre-stressing is applied to the girder, a camber is observed. In Fig. 5, the camber is shown with a maximum negative deflection of almost –8 mm.

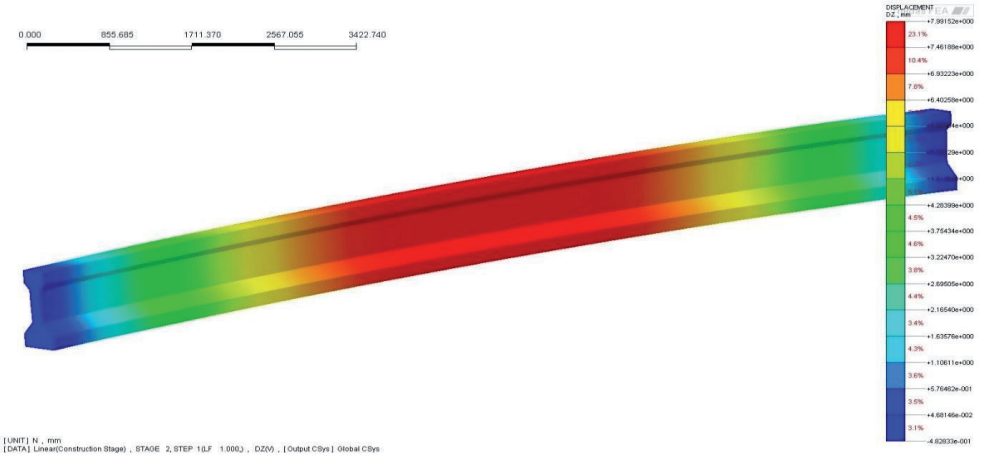

Fig. 5. Displacement due to pre-stressing

4.3. Third stage – casting the slab – wet concrete load

In the third stage, casting of the normal strength concrete deck is simulated. To represent wet concrete with 2316 kg/m^3 density, an equivalent uniform pressure load is applied to the top surface of the girder (Fig. 6).

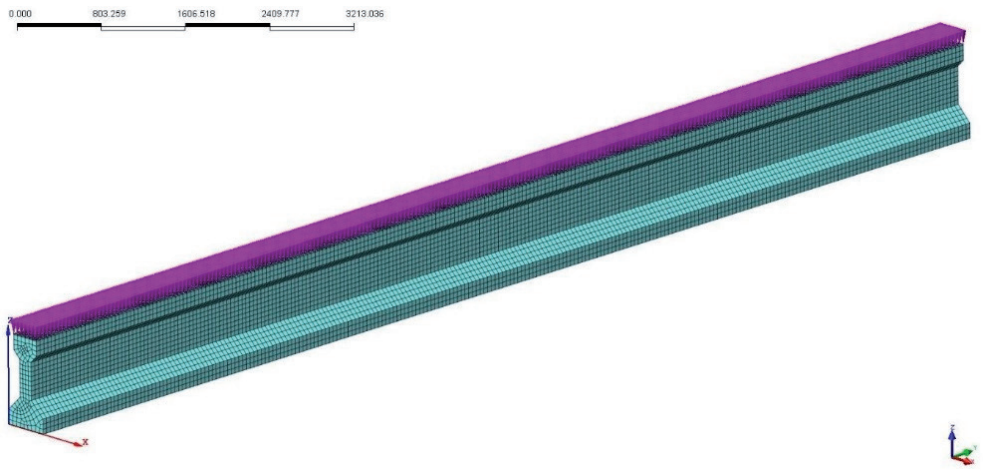

Fig. 6. Representation of wet-concrete load

In this stage, applying a wet concrete load decreases the maximum camber reached in stage two when the pre-stressing forces were applied from –7.99 mm to –5.48 mm (Fig. 7).

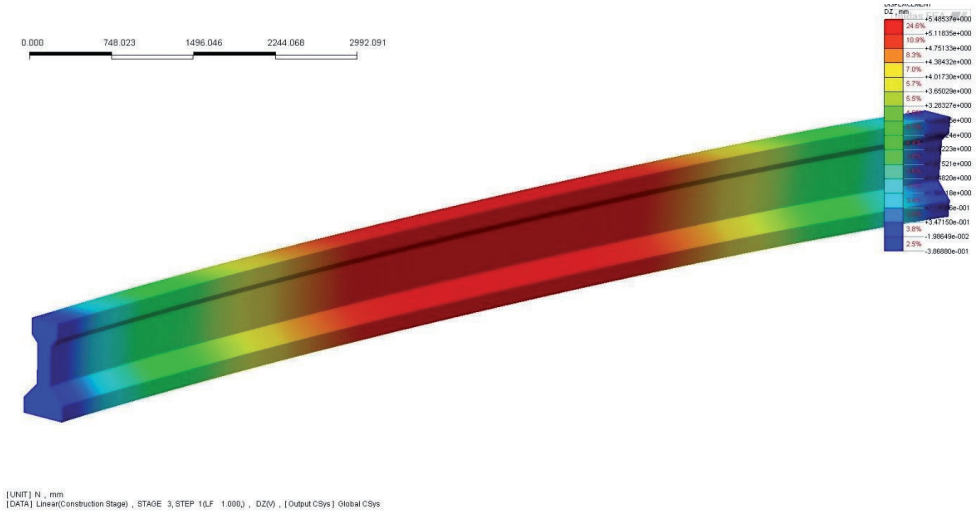

Fig. 7. Displacement after application of wet-concrete load

4.4. Fourth stage – composite girder

In the fourth stage, the cross-section of the girder becomes composite, the wet-concrete load in this stage is deactivated and the slab member becomes active. The cross-section of the girder consists of two parts – the girder and the slab with a rigid connection between them.

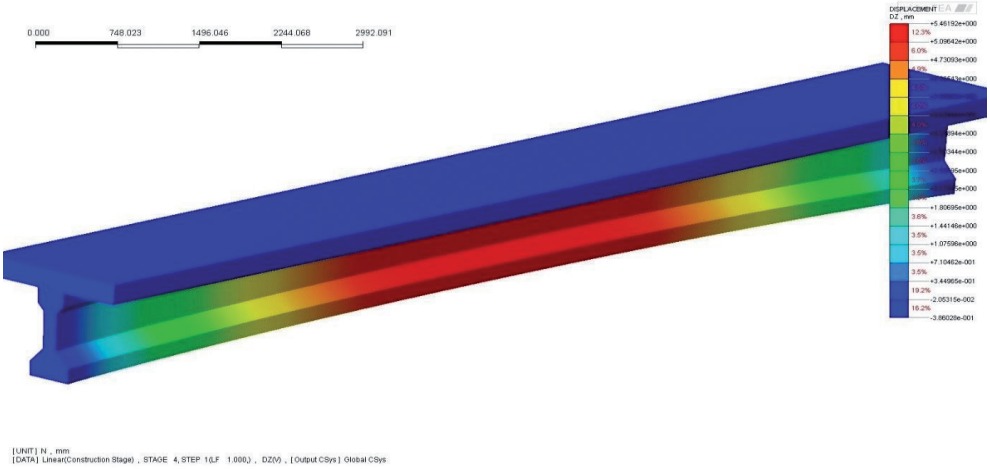

Fig. 8. Displacement of composite girder (due to a graphics malfunction, the curvature of the deck is not represented)

Comparing the results from stage 3 and 4, no significant differences are expected since the slab is connected to the girder with negative deflection. This is shown in Fig. 8. where the slab initial shape is not properly represented.

The maximum vertical displacement at the mid-span of the composite girder is –5.46 mm, this is almost the same as in stage 3, which was expected. The changes to self-weight due to evaporation of water during the hardening of concrete have been neglected.

4.5. Fifth stage – external load

In the last stage, the external load is applied, the value of the load is adopted according to the experimental results as described in [3]. The maximum displacement caused by the cracking load is 4.6 mm with L/250 [6] condition of 5 mm (Fig. 9). The maximum tension stress at the mid-span of the girder is calculated as 3.7 MPa which compares well with the tension strength of concrete used in the experiment described in [3].

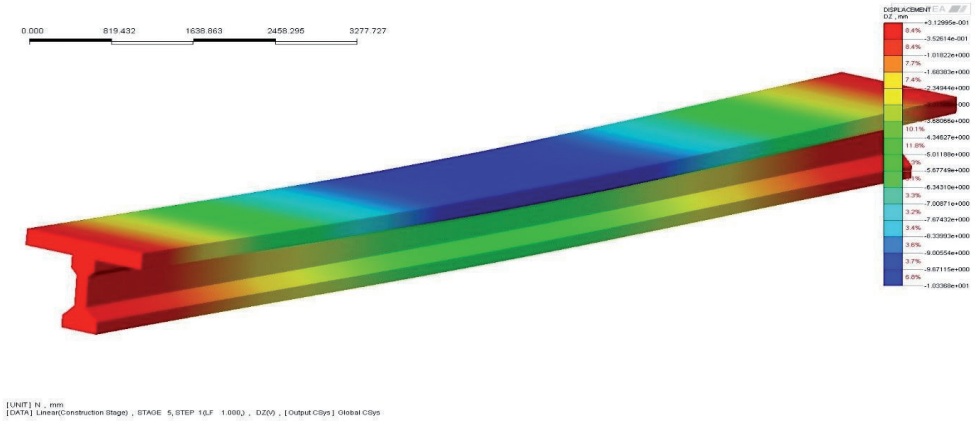

Fig. 9. Displacement after external cracking load application

5. Construction stage analysis with time-dependent effects

5.1. Third stage – casting the slab – wet concrete load

The first and the second stages do not change because there is no creep influence on the deformations and the stress distribution. The results from the construction stage analysis with or without taking the creep phenomenon into account are the same for these stages. In the third stage, after the pre-stressing and wet concrete load is applied, there is a mid-span deflection (camber) of –12.7 mm (Fig. 10) compared with –5.48 mm when creep is not taken into account. This difference occurs due to creep deformation occurring within 14 days of pre-stressing of the girder.

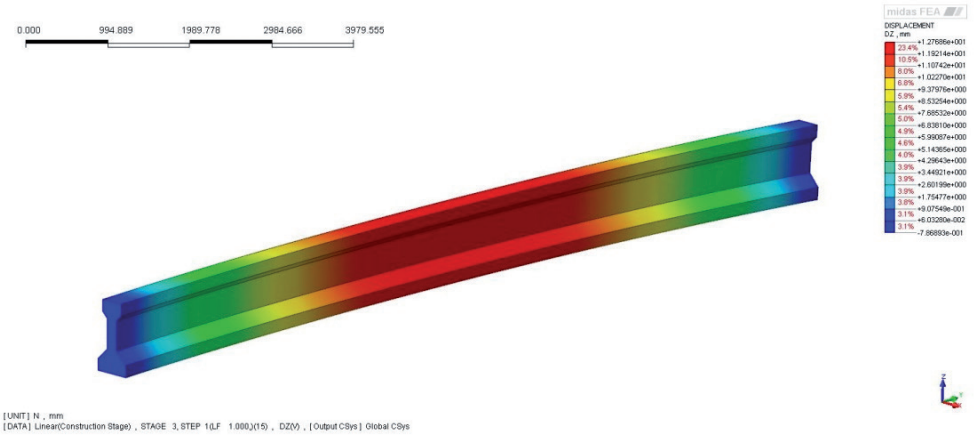

Fig. 10. Displacement due to wet-concrete load with time effects

5.2. Fourth stage – composite girder

In this stage, after forming the composite section, the negative mid-span deflection increased slightly from –12.7 mm to –13.2 mm (Fig. 11). The low increment of the deformation is due to creep of concrete which is limited by the self-weight load of the slab. The stresses in the girder in this stage are slightly lower compared to the third stage (the difference is about 0.5 to 1.0 MPa), this is because of the creep which results in a decrease of the pre-stressing force (Fig. 12).

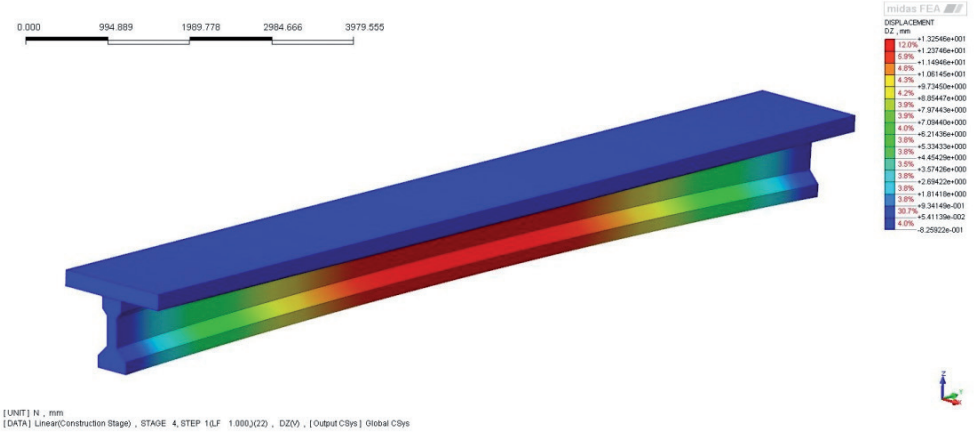

Fig. 11. Displacement of composite girder with the creep behaviour (due to graphics malfunction, the curvature of the deck is not represented)

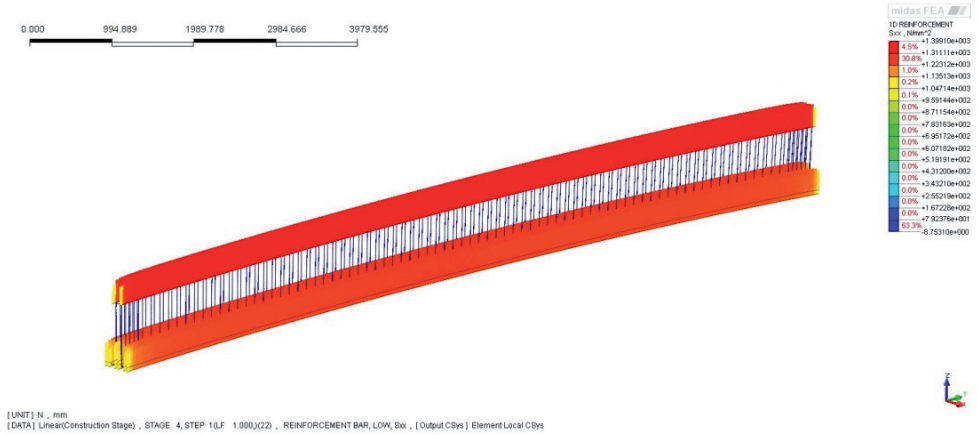

Fig. 12. Stress distribution along the pre-stressing strands

5.3. Fifth stage – external load

After the cracking load is applied, one can observe change in the girder deflection (camber) from –13.2 mm to –3.42 mm which means that the deflection of the composite girder is 9.6 mm (Fig. 13). The deflection of the slab is approximately the same as the deflection in the construction stage analysis without time dependent behaviour in the fifth stage. This is because the creep phenomenon for the NSC (slab) begins in the stage when the external load is applied to the slab. In a short time period, creep has a positive influence on the girder deflection which is smaller and positive. The maximum tensile stress at the mid-span on the bottom surface is now 4.28 MPa compared with 3.7 MPa when the creep is not taken into account.

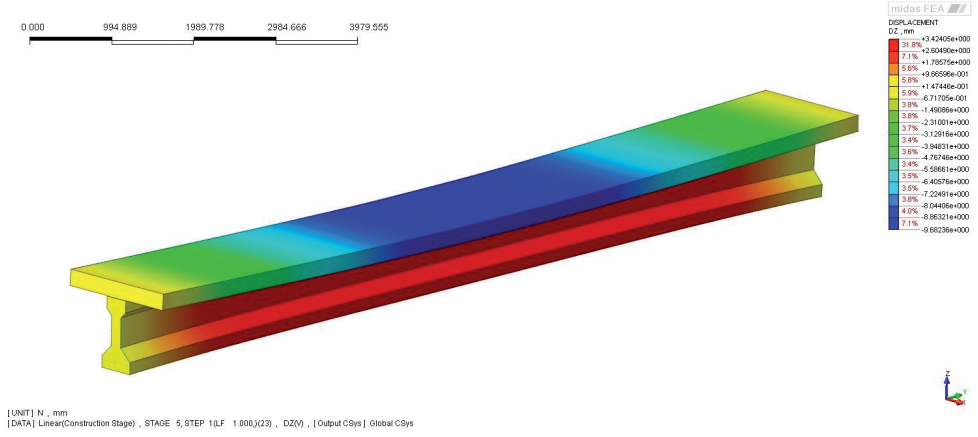

Fig. 13. Deflection of composite girder with creep

5.4. Sixth stage – long term behaviour (10,000 days)

Sixth stage is an additional stage which represents the long-time behaviour of the concrete and it lasts for 10,000 days. The deflection of the girder increases from negative –3.54 mm to positive 8.0 mm and from 9.6 mm to 21 mm for the slab (Fig. 14). The increase of the maximum tensile stress at the mid-span on the bottom surface of the girder due to creep is observed with a value of 7.68 MPa which exceeds the tensile strength of the concrete used.

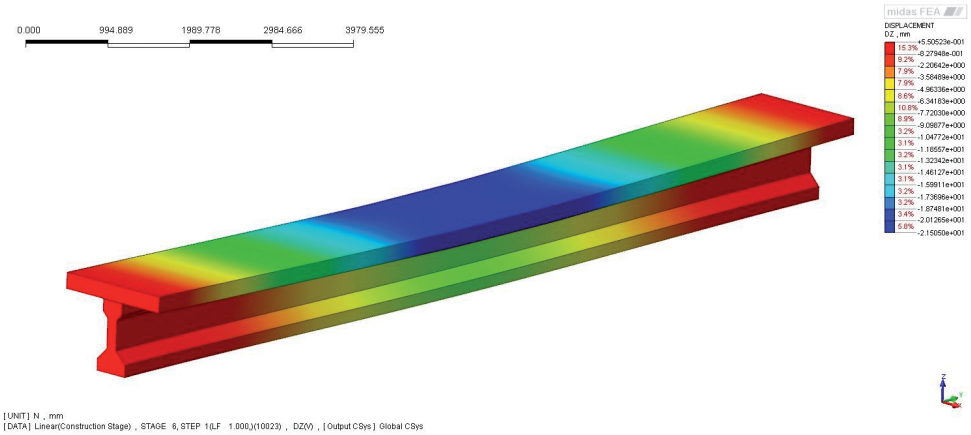

Fig. 14. Deflection of composite girder for long-term behaviour (10,000 days)

The longitudinal stress distribution along the pre-stressing strands after 10,000 days is shown in Fig. 15. The maximum stress in the strands is 1316 MPa and long-term loss of the pre-stressing force due to creep is observed (7% loss).

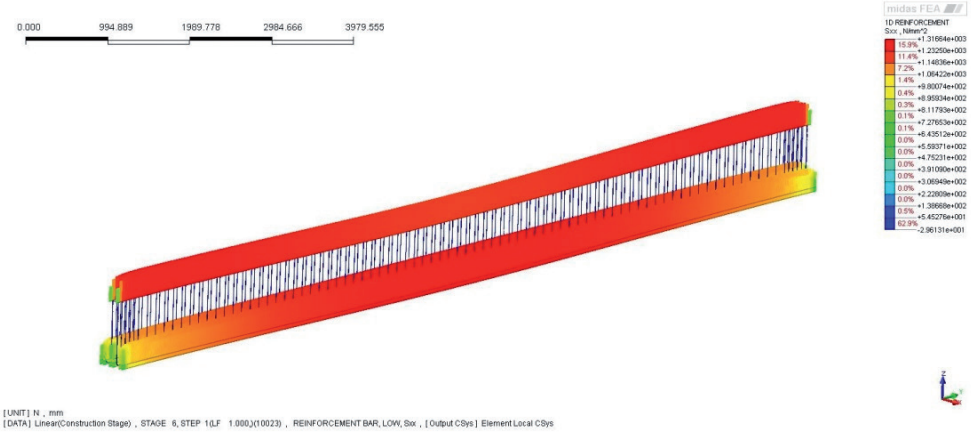

Fig. 15. Stress distribution along pre-stressing strands after 10,000 days

6. Conclusions

The study shows a significant influence of creep in the modelling of the bending behaviour of the concrete-concrete composite girder with construction stages taken into account. The conclusion can be inferred that in structures built in stages, such as composite and additionally pre-stressed, rheological effects cannot be ignored. Not taking into account the time-dependent effects causes a significant underestimation of the level of stress in the structure relating to long-term behaviour – this could even lead to exceeding the strength of the materials. Based on the literature review and experimental research performed by Choi [4], future work is proposed. The main purpose of the research is to implement a new concrete visco-elastic model to account for rheological effects. Using a generalised Maxwell spring-dashpot model [7], an incremental formulation of the linear viscoelasticity model for ageing materials was derived [8]. The model is based on the superposition principle for the visco-elastic behaviour of concrete under continuous loading and profits from the spectral form of the characteristic function for the material. In the further plans the model will be programmed in the 3D FEM software package. The results will be compared with existing models which are based on the CEB-FIP, ACI, AASHTO and EC recommendations for creep and shrinkage functions.

References

[1] Issa M., Salsa J., Shabila H., Alrousan R., *Composite behavior of precast concrete full-depth panels and prestressed girders*, PCI Journal, September-October 2006, Vol. 51, No. 5, 132–145.

[2] Mokhtarzadeh A., French C., *Bibliography on high strength concrete*, PCI Journal 2004, Vol. 38, 130–137.

[3] Choi W., Rizkalla S., Zia P., Mirmiran A., *Behavior and design of high-strength prestressed concrete girders*, PCI Journal. September-October 2008, Vol. 53, No. 5, 54–69.

[4] Choi W., *Flexural behavior of prestressed girder with high strength concrete*, Raleigh, North Carolina, A&T State University 2006, Ph.D. Dissertation.

[5] Model Code Model 2010, *Internation Federation for Structural Concrete (fib)*, Vol. 1, Lausanne 2010.

[6] Eurocode 2, Design of Concrete Structures. Part 1–1: General Rules and Rules for Buildings, Brussels 2004.

[7] Jarno Ł., Gwoździewicz P., Desterbecq J.-F., *Concrete members prestressed with shape memory alloys, Theoretical approach*, 7th International Conference Analytical models and new concepts in concrete and masonry structures, Proceedings, Kraków, Czerwiec 2011.

[8] Jarno L., *Shape memory alloys application in pre-stressed concrete structures*, Master thesis, Cracow University of Technology, 2010.

TECHNICAL TRANSACTIONS | CZASOPISMO TECHNICZNE
CIVIL ENGINEERING | BUDOWNICTWO
3-B/2015

MAŁGORZATA JANUS-MICHALSKA*, RAFAŁ ZAWIŁA**

COMPARATIVE STUDY OF THE LOAD-BEARING CAPACITY OF COMPOSITE LAMINATED CYLINDRICAL SHELLS

STUDIUM PORÓWNAWCZE NOŚNOŚCI WIELOWARSTWOWYCH CYLINDRYCZNYCH POWŁOK KOMPOZYTOWYCH

Abstract

This paper presents a comparison of pressure for composite laminated cylinders leading to progressive damage of subsequent plies. Laminates made of epoxy resin with glass fibre used in various ply stacking sequences are considered. Numerical calculations based on Mathcad author's code are performed. Results utilising last ply failure criterion are specified. The effects of subsequent ply angles on load capacity is investigated.

Keywords: *composite laminate, progressive damage, load-bearing capacity*

Streszczenie

Artykuł przedstawia porównanie wartości ciśnienia wewnętrznego dla kompozytowych zbiorników cylindrycznych prowadzącego do zniszczenia kolejnych warstw. Rozważono laminaty z żywic epoksydowych zbrojonych włóknami szklanymi o różnorakim ułożeniu warstw. Obliczenia numeryczne przeprowadzono w oparciu o autorskie procedury napisane w programie Mathcad. Wyznaczanie nośności opiera się na kryterium zniszczenia ostatniej warstwy. Na podstawie otrzymanych wyników zbadano wpływ kąta ułożenia kolejnych warstw na nośność.

Słowa kluczowe: *kompozyty wielowarstwowe, nośność, progresywne niszczenie warstw*

DOI: 10.4467/2353737XCT.15.165.4340

* Ph.D. Eng. Małgorzata Janus-Michalska, Institute of Structural Mechanics, Faculty of Civil Engineering, Cracow University of Technology.

** M.Sc. Eng. Rafał Zawiła, Graduate of Faculty of Civil Engineering, Cracow University of Technology.

1. Introduction

Composites are increasingly used in engineering structures due to their high strength and stiffness. To achieve improved strength and stiffness, composities are made of layers with unidirectional continuous fibers in the form of a laminate. The mechanics of laminates treated as special structures is formulated in a special convention and given in many books and manuals, for example by Milton [11], Laszlo & Kollar [9], Jones [8], German [5], Muc [12].

Composite laminates not only offer high levels of strength, but also maintain load-bearing capacity even in the presence of damage to individual plies. This property has been analysed by Craddock [2], Chang [3], German [6].

The wide use of laminates in a variety of engineering fields involves the use of special design rules. Some aspects of designing conditions can be developed and added to design procedures.

Laminates are a family of materials for which mechanical properties can be tailored. The matrix, the reinforcement material and the volume of reinforcement can be varied to achieve the required properties. The effect of the stacking layer sequence on damage tolerance was studied by Bezazi [1], Park et al. [14] and Tsau & Liu [16]. The influence of the stacking sequence on the stress distribution of laminates was described by Tsau & Liu [16]. Park [15] made an attempt to find the optimal stacking for various loads.

The present work is focused on tailoring the laminate structure by adjusting the angle of laminate plies for achieving the maximal load bearing capacity. Laminates made of epoxy resin with glass fibre are chosen as a material used for the cylinder structure of pressure tanks.

2. Classical theory of laminates

The elastic behaviour of laminates is described by the generalised Hooke's law [8, 9], which linearly relates the generalised forces to the generalised strains as written below:

$$\begin{pmatrix} \mathbf{N} \\ \mathbf{M} \end{pmatrix} = \begin{bmatrix} \mathbf{A} & \mathbf{B} \\ \mathbf{B} & \mathbf{D} \end{bmatrix} \begin{pmatrix} \boldsymbol{\mu}^0 \\ \boldsymbol{\kappa}^0 \end{pmatrix} \tag{1a}$$

where:

- $\mathbf{N}$ – in-plane forces,
- $\mathbf{M}$ – bending moments,
- $\boldsymbol{\varepsilon}^0$ – midplane strains,
- $\boldsymbol{\kappa}^0$ – midplane curvatures,
- $\mathbf{A}$ – membrane stiffnesses,
- $\mathbf{D}$ – bending stiffnesses,
- $\mathbf{B}$ – membrane-bending coupling stiffness,
- $\mathbf{A}, \mathbf{B}, \mathbf{D}$ – fourth order tensors.

Stiffness tensors are defined as weighted integrals of ply stiffnesses $\bar{\mathbf{Q}}$ over the plate thickness t and can be written as follows:

$$\mathbf{A} = \sum_{k=1}^{N} \left(\bar{\mathbf{Q}}\right)_k \left(z_k - z_{k-1}\right), \quad \mathbf{B} = \frac{1}{2} \sum_{k=1}^{N} \left(\bar{\mathbf{Q}}\right)_k \left(z_k^2 - z_{k-1}^2\right), \quad \mathbf{D} = \frac{1}{3} \sum_{k=1}^{N} \left(\bar{\mathbf{Q}}\right)_k \left(z_k^3 - z_{k-1}^3\right) \tag{1b}$$

where:

N – number of layers,

z_k – distances of layer from reference plane, as shown in Fig. 1.

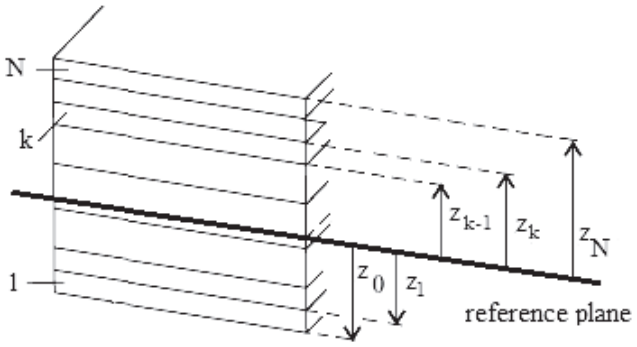

Fig. 1. Distances of layers from reference plane

Ply stiffnesses $\bar{\mathbf{Q}}$ in global system of coordinate can be obtained by transformation of stiffness tensor **Q** from local ply coordinate system associated with fiber direction, as can be seen in Fig. 2.

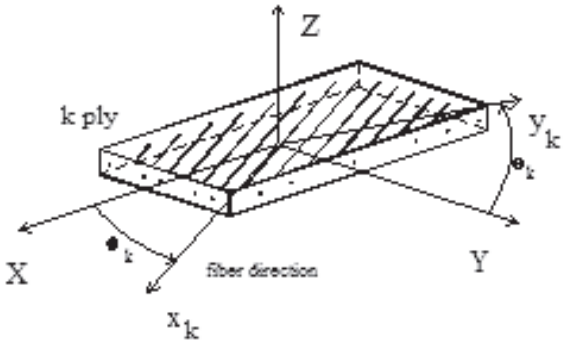

Fig. 2. Global (XYZ) and local ($x_k y_k z_k$) coordinate system

Constitutive equations given by the relationship $\boldsymbol{\sigma} = \mathbf{Q}\boldsymbol{\varepsilon}$ are set in the ply local system of coordinates.

For unidirectional ply, fibre reinforcement non-zero stiffness components are expressed by ply material constants as follows:

$$Q_{1111} = \frac{E_1}{1-\nu_{12}\nu_{21}}, \quad Q_{1122} = \frac{\nu_{12}E_2}{1-\nu_{12}\nu_{21}}, \quad Q_{2222} = \frac{E_2}{1-\nu_{12}\nu_{21}}, \quad Q_{1212} = G_{12} \tag{2}$$

3. Failure criteria

The engineering formula for practical design indicates the load at which laminate failure occurs. Many theories are proposed but none of them are sufficient for the description of the failure of the whole laminate. Failure criteria are formulated only for separate ply in the general form:

$$f\left(\sigma, X_1, ..., X_N\right) = 1 \tag{3}$$

where:

$\boldsymbol{\sigma}$ – state of stress,
$X_1, ..., X_N$ – set of strength parameters.

Three criteria are proposed:
maximum stress criterion

$$X_C < \sigma_1 < X_T, \quad Y_C < \sigma_2 < Y_T, \quad -S < \sigma_6 < S \tag{4a}$$

quadratic criteria, Tsai-Wu

$$\left(\frac{1}{X_T}-\frac{1}{X_C}\right)\sigma_1 + \left(\frac{1}{Y_T}-\frac{1}{Y_C}\right)\sigma_2 + \frac{1}{X_T}\frac{1}{X_C}\sigma_1^2 + \frac{1}{Y_T}\frac{1}{Y_C}\sigma_2^2 + \\ + \frac{1}{S^2}\sigma_6^2 - \sqrt{\left(\frac{1}{X_T}-\frac{1}{X_C}\right)\left(\frac{1}{X_T}-\frac{1}{X_C}\right)}\sigma_1\sigma_2 \le 1 \tag{4b}$$

and Azzi-Tsai-Hill

$$\frac{\sigma_1^2}{X^2} + \frac{\sigma_2^2}{Y^2} - \frac{\sigma_1\sigma_2}{XY} + \frac{\sigma_6^2}{S^2} \le 1 \tag{4c}$$

where:

$$X = \begin{cases} X_T - \text{tensile strength for } \sigma_1 > 0 \\ X_C - \text{compresssive strength for } \sigma_1 < 0 \end{cases}$$

$$Y = \begin{cases} Y_T - \text{transverse tensile strength for } \sigma_2 > 0 \\ Y_C - \text{transverse compressive strength for } \sigma_2 < 0 \end{cases}$$

S – transverse shear strength,

$\sigma_1, \sigma_2, \sigma_6$ – plane stress tensor components in Voigt notation.

The Azzi-Tsai-Hill criterion is a generalisation of the Huber-Mises-Hencky yield condition for orthotropy and is the most frequently used in with regard to engineering usage of laminates.

For quadratic criteria, it is useful to introduce material effort coeficient $\varphi = \varphi(\boldsymbol{\sigma}, X_1, ..., X_N)$ defined in such a way that the criterion is written as follows: $\varphi \leq 1$.

The given criteria specify the load for which the first ply failure occurs. When this condition is adopted as a failure of the whole laminate, we obtain the first ply failure criterion (FPF criterion). When we follow load changes until the last ply fails, the last ply failure criterion (LPF criterion) is obtained.

4. Last ply failure method and algorithm of strength analysis

With regard to the first ply failure, the whole laminate does not completely fail because unfailed plies carry load. If the applied load is increased, a series of ply failures occur which leads to total failure.For the last ply failure, the final load may be much higher than for the first ply failure. The conclusion is that the LPF method is less conservative than FPF (first ply failure). For our analysis, we use the LPF method with the algorithm of laminate stress analysis proposed by German & Mikulski [6] as shown in Fig. 3.

5. Cylindrical shell

The thin-walled circular cylinder made of 16 plies creating the symmetrical laminate shown in Fig. 4 is considered. Each ply has a thickness of 0.508 mm. Dimensions of the tank are as shown in Fig. 4. The laminate is made of epoxy resin and glass fibre with various ply stacking sequences. The tank is subjected to internal pressure.

The load-bearing capacity is defined as the maximal pressure that can be applied to the tank structure until subsequent ply failure occurs.

The elastic constants and the strength parameters for the individual plies are as follows:

$$E_1 = 137 \text{ GPa} \qquad E_2 = 10,40 \text{ GPa} \qquad \nu_{12} = 0.3$$

$$X_T = 1500 \text{ MPa} \qquad X_C = 1500 \text{ MPa} \qquad Y_T = 40 \text{ MPa} \qquad S = 68 \text{ MPa}$$

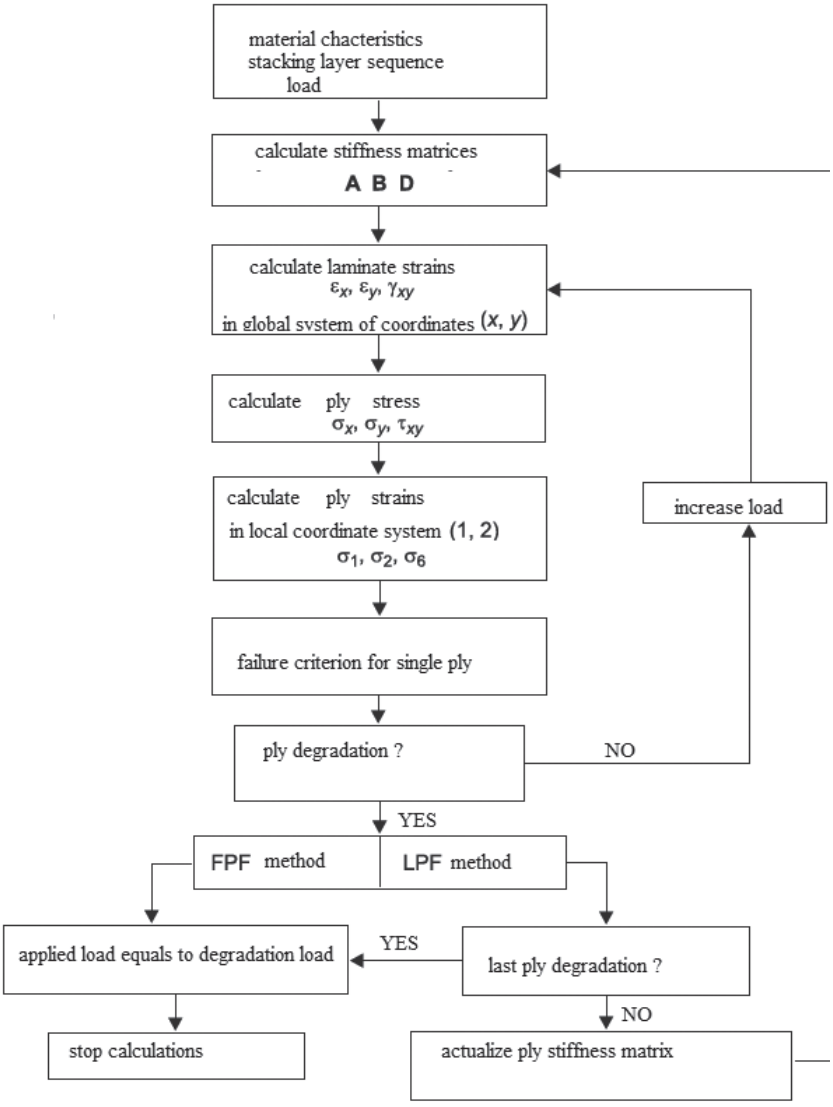

Fig. 3. Algorithm of strength analysis of composite laminate

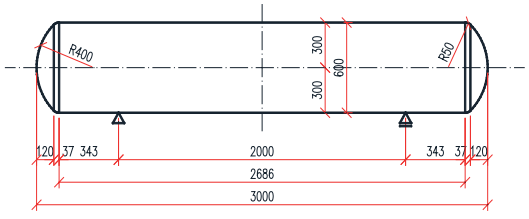

Fig. 4. Composite laminated cylindrical tank dimensions [mm]

6. Numerical analysis and results

Simulations were performed using the author's code written in Mathcad. The important new aspect of the work is the implementation of the algorithm presented in Fig. 3. The code is based on the analytical formulation of the problem. Numerical results are compatible with those obtained by the finite element method using ABAQUS code as presented in detail in the work by Zawiła [18].

It is worth emphasising that the load bearing capacity and its increase by the use of the last ply failure criterion compared with the use of the first ply criterion is difficult to predict by engineering intuition.

The most interesting results are presented below and collated in Table 1. The first step is defined for FPF. Subsequent steps are defined for the failure of the next plies until the last ply fails (LPF). For calculating the material effort for each individual ply, the Azzi-Tsai-Hill criterion is applied.

For each example, the laminate code, the load-bearing capacity in subsequent steps and the distribution of material effort coefficient over the laminate thickness is given.

Laminate code $[0, 0, 15, 15, 30, 30, 30, 30]_s$

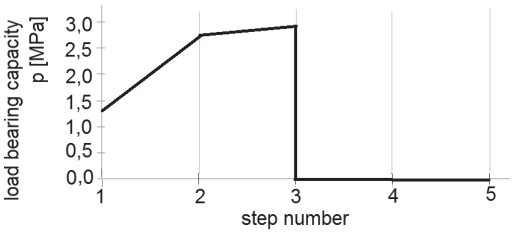

Fig. 5a. Load-bearing capacity in subsequent steps

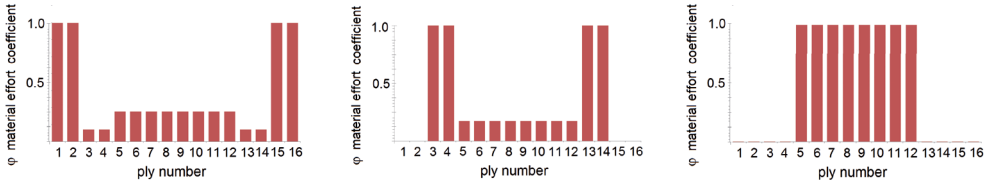

Fig. 5b. Stress distribution

Laminate code $[90, 90, 75, 75, 75, 60, 60, 60]_s$

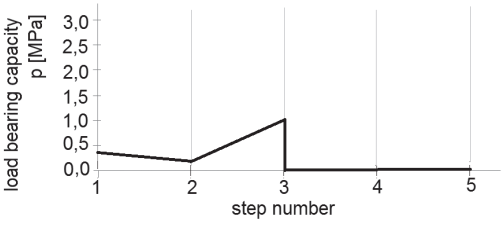

Fig. 6a. Load-bearing capacity in subsequent steps

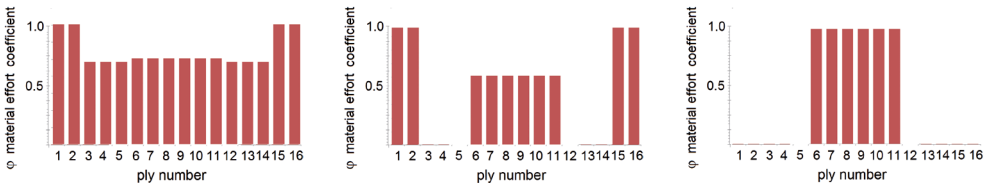

Fig. 6b. Stress distribution

Laminate code$[0, 0, 15, 15, 15, 30, 30, 30]_s$

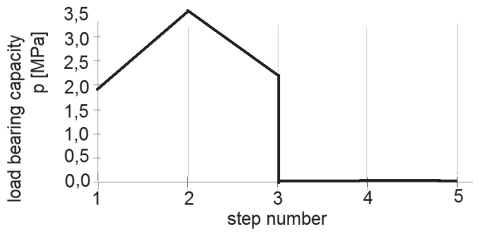

Fig. 7a. Load-bearing capacity in subsequent steps

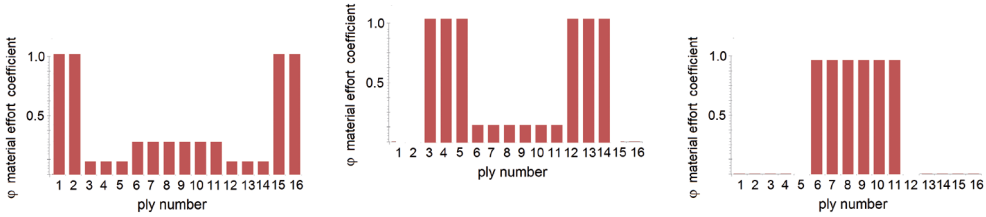

Fig. 7b. Stress distribution

Laminate code $[90, 90, 45, 45, 45, 45, 0, 0]_s$

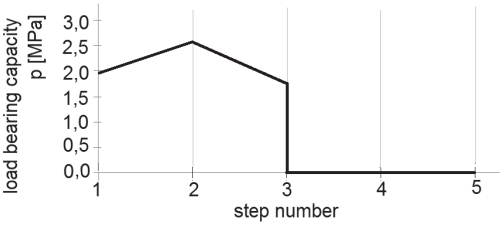

Fig. 8a. Load-bearing capacity in subsequent steps

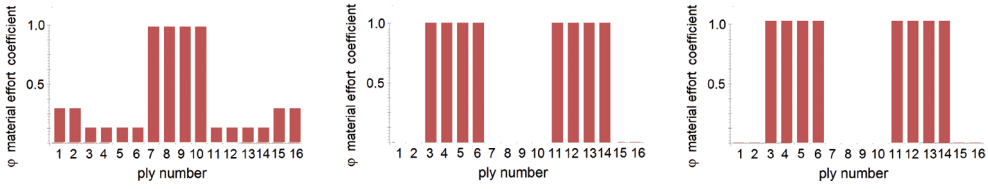

Fig. 8b. Stress distribution

Laminate code $[75, 75, 60, 60, 45, 45, 90, 90]_s$

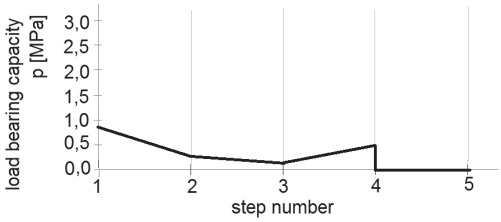

Fig. 9a. Load-bearing capacity in subsequent steps

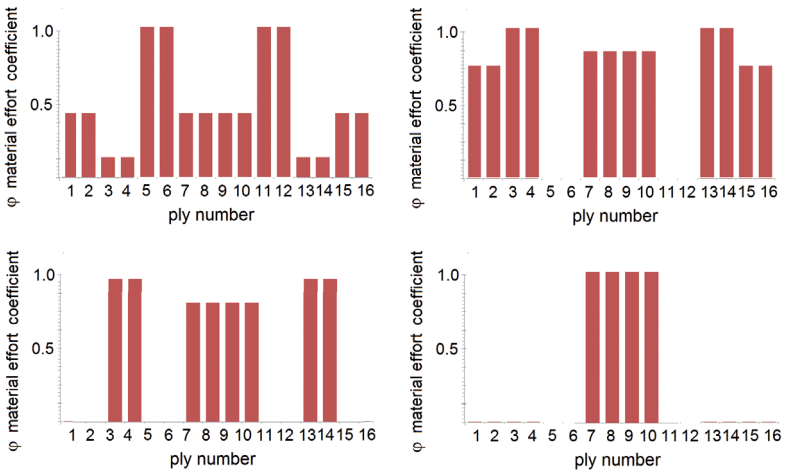

Fig. 9b. Stress distribution

Table 1

Load-bearing capacity p [MPa] for different ply stacking sequences

Laminate code	Step 1	Step 2	Step 3	Step 4	Step 5
$[0, 0, 15, 15, 30, 30, 30, 30]_s$	1.353	2.671	2.776	–	–
$[90, 90, 75, 75, 75, 60, 60, 60]_s$	0.443	0.173	1.000	–	–
$[0, 0, 15, 15, 15, 30, 30, 30]_s$	1.946	3.520	2.083	–	–
$[90, 90, 45, 45, 45, 45, 0, 0]_s$	1.906	2.500	1.776	–	–
$[75, 75, 60, 60, 45, 45, 90, 90]_s$	0.836	0.240	0.181	0.543	–
$[75, 75, 60, 60, 30, 30, 0, 0]_s$	2.136	1.093	0.786	0.571	–
$[75, 75, 15, 15, 45, 45, 90, 0]_s$	2.456	1.903	1.086	0.110	0.087
$[75, 75, 60, 60, 30, 30, 0, 0]_s$	2.136	1.903	0.786	0.507	–
$[75, 75, 60, 60, 30, 30, 15, 15]_s$	2.033	1.903	0.786	0.507	–
$[90, 90, 45, 45, 45, 0, 0, 0]_s$	2.616	2.060	0.543	–	–
$[90, 90, 75, 75, 15, 15, 0, 0]_s$	2.693	1.463	0.726	0.543	–

7. Conclusions

The study presented in this paper is focused upon the linear static behaviour and uses the author's Mathcad code based on classical theory of laminates. The effect of the ply angle on the load–bearing capacity of the laminate subjected to membrane forces is described. The presented results show that the last ply failure criterion allows to exploit material better than first ply criterion.

In some cases, the ply angle adjustment gives the significant possibility of raising the load-bearing capacity. It gives reserve of load from first failure to complete damage of composite. These examples as the most interenting are presented in details in Figures 5–9. Figures with index 'a' present the rise of load bearing capacity, figures with index 'b' present which ply fails is subsequent steps. In some cases, the ply angle arrangement does not give the possibility to raise the load-bearing capacity - this means that the maximal load for FPF is greater than the load for LPF – such examples are presented in Table 1.

In future work, we plan to include the design of the structure for the interaction of moments and membrane forces. Additionally, the extension of the method to complex loads will be considered.

References

[1] Bezazi A., El Mahi A., Berthelot J., Bezzazi B., *Analyse de l'endommagement des stratifiés en flexion 3-points. Influence de la séquence d'empilement*, XVème Congrès Français de Mécanique, Nancy, 3–7 Septembre, 2001.

[2] Craddock J.N., *Behaviour of composite laminates after first-ply failure*, Composite Structures, Vol. 3, 1985, 187–200.

[3] Chang R.R., *Experimental and theoretical analyses of first-ply failure of laminated composite pressure vessels*, Composite Structures, Vol. 49, 2000, 237–243.

[4] Decolon Ch., *Analysis of Composite Structures*, Hermes Penton Ltd., 2002.

[5] German J., *Podstawy mechaniki kompozytów włóknistych*, Wydawnictwo Politechniki Krakowskiej, Kraków 1996.

[6] German J., Mikulski Z., *Numeryczna symulacja stopniowego uszkadzania się laminatów kompozytowych*, Czasopismo Techniczne, 3-M/2010.

[7] Hebda M., *Zastosowanie energetycznego kryterium wytężeniowego do analizy wytrzymałościowej*, praca doktorska, Politechnika Krakowska, Kraków 2006.

[8] Jones R.M., *Mechanics of Composite Materials*, Taylor & Francis Inc., Philadelphia 1999.

[9] Laszlo P., Kollar G.S., *Mechanics of Composite Structures*, Springer, Cambridge University Press, Cambridge 2003.

[10] Lukkassen D., Meidell A., *Advanced Materials and Structures and their Fabrication Processes*, Book manuscript, Narvik University College, HiN, August 31, 2008.

[11] Milton G.W., *Theory of Composites*, Cambridge University Press, Cambridge 2004.

[12] Muc A., *Konstrukcje i materiały kompozytowe, problemy i zadania*, Politechnika Krakowska, Kraków 2011.

[13] Muc A., *Projektowanie kompozytowych zbiorników ciśnieniowych*, Politechnika Krakowska, Kraków 1999.
[14] Park J.H., Hwang J., Lee C., Hwang W., *Stacking sequence of composite laminates for maximum strength using genetic algorithms*, Composite Structures., **52**, Issue 2, 2001, 217–231.
[15] Shi C., Mo Y.L., *High-Performance Construction Materials*, World Scientific Publishing Co., Singapore 2008.
[16] Tsau L.R., Liu C.H., *A comparison between two optimisation methods on the stacking sequence of fibres-reinforced composite laminate*, Composite Structures, Vol. 55, Issue 3, 1995, 515–525.
[17] Verchery G., *Design rules for the laminate stiffness*, Mechanics of Composite Materials, Vol. 47, No. 1, March, 2011.
[18] Zawiła R., *Analiza zniszczenia ścianki zbiornika kompozytowego przy niszczeniu kolejnych jej warstw*, praca magisterska, Instytut Mechaniki Budowli, Wydział Inżynierii Lądowej, Politechnika Krakowska, Kraków 2014.

TECHNICAL TRANSACTIONS | CZASOPISMO TECHNICZNE
CIVIL ENGINEERING | BUDOWNICTWO
3-B/2015

SZYMON KAŹMIERCZAK*

SELECTED ISSUES OF PRESTRESSED CONCRETE CONTAINMENT TANKS FOR THE STORAGE OF LIQUEFIED GASES DESIGN IN ACCORDANCE WITH EN 14620

WYBRANE ZAGADNIENIA PROJEKTOWANIA ZBIORNIKÓW Z BETONU SPRĘŻONEGO DO MAGAZYNOWANIA SKROPLONYCH GAZÓW W UJĘCIU EN 14620

Abstract

In 2014, a new tank for the storage of liquefied ammonia (capacity 22 000 m^3) was built for the chemical industry company 'Grupa Azoty S.A.'. The LNG terminal in Świnoujście, where two large capacity containers (160 000 m^3 each) were built, is almost finished (2015). In both cases, prestressed concrete was used to build a secondary (outer) containment tank.This paper is devoted to general concepts and design considerations for secondary cylindrical, concrete containers for the storage of refrigerated, liquefied gases with temperatures between 0°C and –165°C, according to EN 14620.

Keywords: *prestressed concrete, cylindrical storage tanks, liquefied gases, low temperature*

Streszczenie

W 2014 roku przedsiębiorstwo przemysłu chemicznego Grupa Azoty S.A. oddało do użytku nowy zbiornik do magazynowania skroplonego amoniaku o pojemności 22 tys. m^3. Prace związane z budową terminala LNG w Świnoujściu, gdzie powstały dwa zbiorniki o dużej pojemności (160 tys. m^3 każdy), są niemal ukończone (2015). W obu wymienionych przypadkach konstrukcję zbiornika zewnętrznego wykonano z betonu sprężonego. Artykuł przedstawia ogólne koncepcje i zasady projektowania zewnętrznych walcowych zbiorników z betonu do magazynowania skroplonych gazów o temperaturach pomiędzy 0°C i –165°C, według normy EN 14620.

Słowa kluczowe: *beton sprężony, zbiorniki cylindryczne, skroplone gazy, niska temperatura*

DOI: 10.4467/2353737XCT.15.166.4341

* Ph.D. Eng., Szymon Kaźmierczak, Institute of Building Materials and Structures, Faculty of Civil Engineering, Cracow University of Technology.

1. Introduction

The current version of standard EN 14620[1] specifies the recommendations for materials, design rules, construction details and installation principles for above ground containment tanks for the storage of liquefied, refrigerated gases.

Liquefied gas has to be stored at a temperature equal to its atmospheric boiling point (Table 1).The correct temperature level in combination with a small overpressure (≤ 500 mbar) is necessary in order to achieve equilibrium between liquid and vapour phases inside the storage tank.

Table 1

Physical properties of pure gases [1.1]

Name	Chemical formula	Mol. mass [g/mol]	Boiling point [°C]	Latent heat of vapour at boiling point [kJ/kg]	Liquid density at boiling point [kg/m^3]	Gas density at boiling point [kg/m^3·10^{-8}]	Vol. of gas liberated by 1 m^3 of liquid (exp. to 15 [°C] at 1 [bar]) [m^3]
N-Butan	C_4H_{10}	58 123	–0.5	385	601	270	239
Izo-Butan	C_4H_{10}	58 123	–11.7	366	593	282	236
Amoniak	NH_3	17 030	–33.3	1367	682	905	910
Butadien	C_4H_6	54 091	–4.5	417	650	255	279
Propan	C_3H_8	44 096	–42.0	425	582	242	311
Propylen	C_3H_6	42 080	–47.7	437	613	236	388
Etan	C_2H_6	30 069	–88.6	487	546	205	432
Etylen	C_2H_4	28 054	–103.7	482	567	208	482
Metan	CH_4	16 043	–161.5	509	422	181	630
Note 1: Commercial butane is a mixture in N-Butane and isobutane with a small content of propane and pentane. Note 2: Commercial propane is propane with a small content of ethane and butane.							

2. Concepts of the tank construction

Cylindrical tanks for the storage of liquefied gases are designed on the grounds of four general concepts. Taking into account risk assessment, a certain type of tank construction should be selected:

– **Single containment tank** (Fig. 1a) – in this solution, there is only one (*primary*) self-supporting, steel cylindrical tank to store the liquid product. This primary containment tank may be surrounded by an outer steel tank designed as a vapour barrier or as protection for thermal insulation. Due to the risk of leakage, a single containment tank should be surrounded by a bund wall.

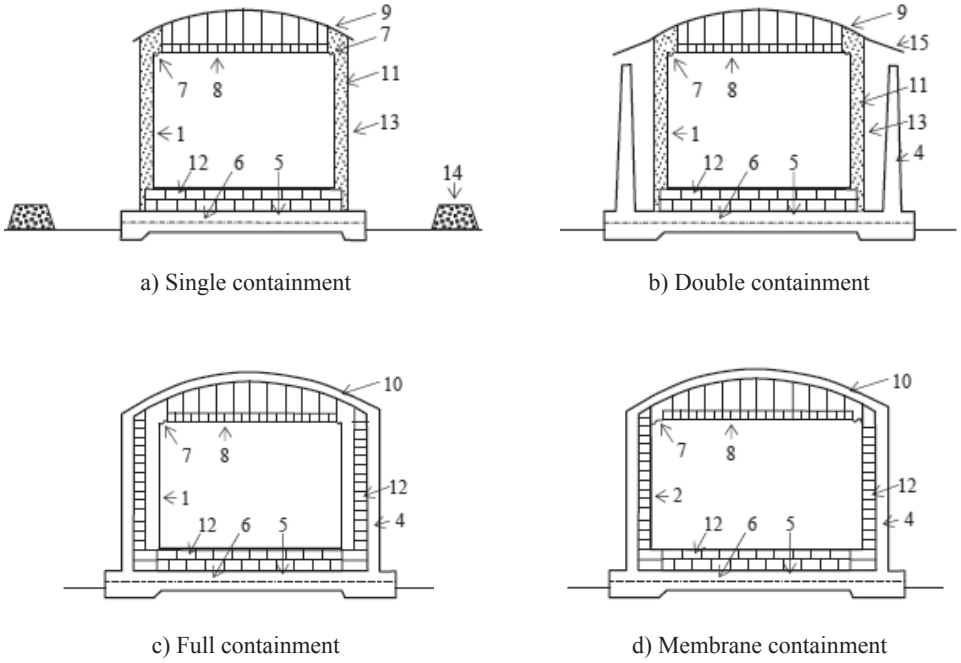

Key:
1. Primary container (steel)
2. Primary container (membrane)
3. Secondary container (steel)
4. Secondary container (prestressed concrete)
5. Foundation
6. Foundation heating system
7. Flexible insulating seal
8. Suspended roof (insulated)
9. Steel roof
10. Concrete roof
11. Loose fill insulation
12. External insulation
13. Outer shell (not capable of containing liquid)
14. Bund wall
15. Cover (rain shield)

Fig. 1. Examples of containment tanks: a) single, b) double, c) full, d) membrane [1.1]

– **Double containment tank** (Fig. 1b) – consists of an inner, primary container (liquid and product vapour barrier) and an outer, secondary containment tank (only liquid barrier in case of leakage from a primary tank). This outer (steel or prestressed concrete) tank should ensure the containment of the whole volume of liquid stored inside the primary tank. The annular space, between both containers, should not be greater than 6.0 m and needs to be protected by a steel shield against rain, snow, dirt etc.
– **Full containment tank** (Fig. 1c) – the primary (inner) and the secondary (outer) container form one integrated tank. Contrary to the ‘double containment tank’ the secondary containment (steel or prestressed concrete) tank should be equipped with a dome roof. Both containers are designed to contain liquid. In cases where the primary tank is open at the top, the product vapours are contained in the outer tank. The annular space between the primary and the secondary containers should not exceed 2.0 m.

– **Membrane tank** (Fig. 1d) – consists of a thin steel membrane and load-bearing thermal insulation working together with a concrete container equipped with a dome roof. In the case of membrane leakage, the secondary concrete tank should be able to hold liquid and the product vapours.

3. Liquid tightness

The prestressed concrete secondary tank should ensure liquid and/or vapour tightness. Liquid leakage through concrete can be prevented in two ways [1.3]:

– Liners (steel plates) or reinforced/unreinforced polymer coatings may be used as a liquid (or vapour) barrier applied on the internal surface of the concrete. If concrete cracking occurs, the liner/coating should prove to be capable of 'bridging'a gap equal to 120% of the calculated crack width.
– A minimum compression zone in the concrete cross-section: x_{min} = 100 mm.

The selection of the type of wall to base connection is an important aspect of liquid tightness. It could be designed as: a sliding joint, pinned joint and fixed joint (Fig. 2). The last connection type is preferred for liquid tightness, but in the case of LNG tanks, it has to be thermally protected due to the risk of cracking in the case of leakage from the primary tank.

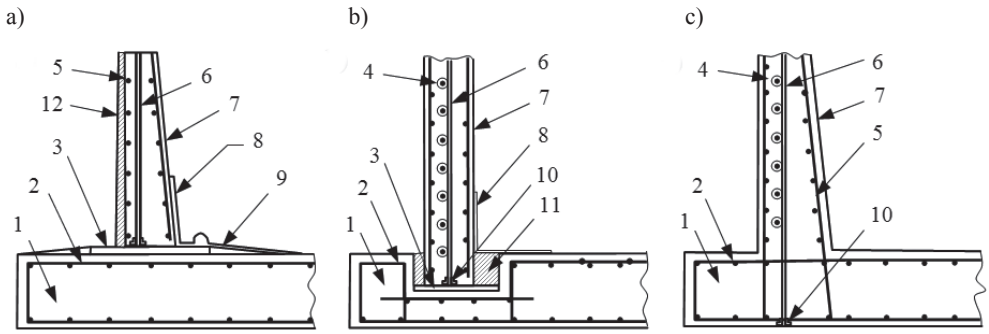

Key:
1) tank base
2) base reinforcement
3) bearing plate
4) circumferential prestress
5) wall reinforcement
6) vertical prestress
7) prestressed wall
8) stainless/nickel stell seal
9) radial strap
10) prestressing anchorage
11) grout
12) wire wound circumferential prestress with shotcrete layer

Fig. 2. Typical connections between the presteressed tank wall and the base: a) sliding joint, b) pinned joint, c) fixed joint [1.3]

4. Load cases

Typical load cases for the prestressed concrete outer tank in all phases of its operational life according to BS 7777-3 [5] are presented in Table 2. In the case of the design values of actions, the effects of actions, material properties, geometric data and design resistance, the reference should be made to EN 1992-1-1 [3]. Recommended values of partial factors for accidental actionsare shown in table 3. There is lack of reference to EN 1991-4 [6] in the range of load combinations or the values of partial load factors.

Table 2

Design situations for prestressed concrete secondary containment [5]

Loading conditions	Normal loads										Emergency loads							
	Construction		Test		Cool down		Operation		Maintenance		Leakage		Blast		Earthquake		Fire	
	W	B	W	B	W	B	W	B	W	B	W	B	W	B	W	B	W	B
Dead weight of concrete	+	+	+	+	+	+	+	+	+	+	+	+	+	+	+	+	+	+
Dead weight of steel tank		+		+		+		+		+		+		+		+		+
Live load	(+)	+					+	+		+								
Pressure				+		+		+		+	+	+	+	+	+	+	+	+
Wind load	+		+		+		+		+		+		(+)		(+)		+	
Prestressing	+	(+)	+	(+)	+	(+)	+	(+)	+	(+)	+	(+)	+	(+)	+	(+)	+	(+)
Shrinkage	+	+	+	+	+	+	+	+	+	+	+	+	+	+	+	+	+	+
Creep	+	+	+	+	+	+	+	+	+	+								
Temperature					(+)	+	(+)	+			+	+		+		+	+	+
Leakage											+	+						
Blast													+	(+)				
Earthquake															+	+		
Fire																	+	
+ applicable, (+) not always applicable, W – tank wall, B – tank base																		

Table 3

Partial load factors for accidental actions [1.3]

Load combinations	Load factors					
	Dead		Imposed		Abnormal	Wind
	Adverse	Beneficial	Adverse	Beneficial	–	–
Normal actions + one accidental action	1.05	1.0	1.05	0	1.0	0.3
Accidental actions: earthquake (SSE), blast overpressure, external impact, fire or leakage from inner tank*						

* In the case of leakage from the primary container it shall be assumed that the secondary container is filled gradually and can contain the whole liquid from the inner tank.

Table 4

Hydrostatic tests [1.5]

Contents	Single containment	Double containment	Full containment	Membrane tank
Ammonia, butane, propane, propylene	Tank (type I–II steels) FH	Inner tank (type I–II steels): FH	Inner tank (type I–IIsteels): FH	–
		Outer tank (type I–IIsteels): FH	Outer tank (type I–IIsteels): FH	–
		Outer tank (prestressed concrete): notest	Outer tank (prestressed concrete): no test	Outer tank (prestressed concrete): PH
Ethane, ethylene, LNG	Tank (type IV steel) PH	Inner tank (type IV steel): PH	Inner tank (type IV steel): PH	–
		Outer tank (type IV steel): PH	Outer tank (type IV steel): PH	–
		Outer tank (prestressed concrete): no test	Outer tank (prestressed concrete): no test	Outer tank (prestressed concrete): PH
FH[1)] – Full height hydrostatic test; PH[2)] – Partial height hydrostatic test				

1) Full height (FH) hydrostatic test – the inner tank should be filled to the maximum design liquid level.
2) Partial height (PH) hydrostatic test – the inner tank should be filled to a level equalling 1.25 times the height of the maximum design liquid level multiplied by the density of the specified product to be stored.

In both cases, the same quantity of water should be used for the testing of the outer tank.

5. Hydrostatic tests

Hydrostatic tests should be carried out to prove that the tank is well designed and constructed to contain the product with no leakage and that its foundation is able to support the tank contents. In the case of the prestressed concrete outer tank, this type of testing is not required (Table 4) – one exception is the membrane tank, which should be hydrostatically tested before the insulation membrane is installed.

6. Material properties under cryogenic conditions

Concrete is well suited for the storage of cryogenic liquids because the majority of its properties improve substantially as temperature is lowered into the cryogenic range (Table 5). In the case of the prestressed concrete tanks, concrete of at least the class C40/50 should be used.

Table 5

Ranges of 'normal' and 'low'temperatures for concrete and steel

Standard	Concrete		Prestressed steel		Normal steel	
	Normal	Low	Normal	Low	Normal	Low
MC2010 [7,8]	0°C ≤ T ≤ +80°C	T <0°C	–40°C ≤ T ≤ +40°C	T <–40°C	–40°C ≤ T ≤ +40°C	T <–40°C
PN-EN 1992-1-1 [3]	0°C ≤ T ≤ +80°C	T <0°C	–40°C ≤ T ≤ +100°C	T <–40°C	–40°C ≤ T ≤ +100°C	T <–40°C
PN-EN 1992-3 [4]	–25°C ≤ T ≤ +20°C	T < –25°C	–40°C ≤ T ≤ +100°C	T <–40°C	–40°C ≤ T ≤ +100°C	T <–40°C
PN-EN 14620-3 [1]	T ≥ –20°C	T < –20°C	≥ –50°C	T <–50°C	T ≥ –20°C	T <–20°C

6.1. Concrete compressive strength

The compressive strength of the concrete increases with cryogenic temperatures [7]. The influence of the low temperature and moisture content on the concrete compressive strength gain Δf_{cm} (Fig. 3) can be estimated fromformula (1):

MC2010
$$\Delta f_{cm}(T, mc) = 12mc\left[1-\left(\frac{T+170}{170}\right)^2\right] \text{ if } 0°C \geq T \geq -170°C \quad (1)$$

where:

T – the temperature [°C];
mc – the percentage of moisture content by mass.

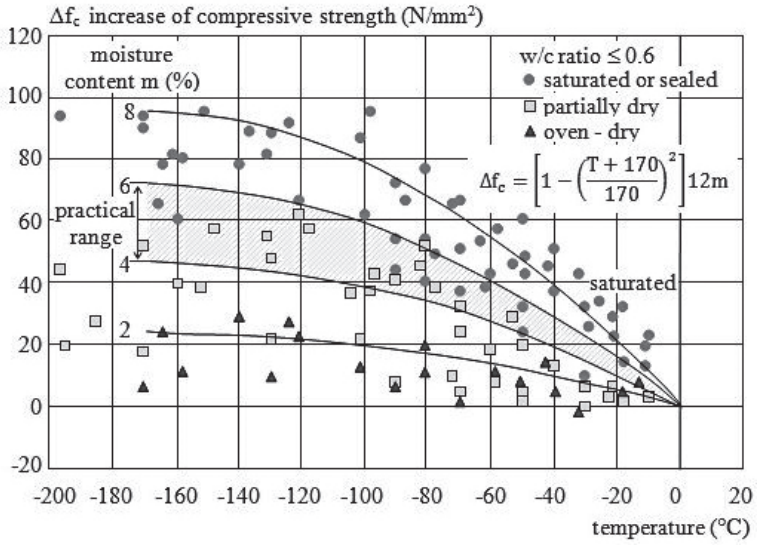

Fig. 3. Increase of compressive strength Δf_{cm} as a function of temperature and moisture content (Van der Veen, 1987) [9]

In practice, the following values of *m* may be assumed:
- 2% (general indoor);
- 4% (general outdoor);
- 6% (exposed to rain).

6.2. Compressive stress – strain relation for concrete

The influence of temperature on the stress-strain relationship (Fig. 4) can be expressed by equation (2):

MC2010

$$\sigma_c(t) = f_c(T, mc) \cdot \left[1 - \left(1 - \frac{\varepsilon_c(T)}{\varepsilon_{f_c}(T)} \right)^n \right] \tag{2}$$

where:

$\sigma_c(t)$ and $\varepsilon_c(T)$ – are stress and strain at a given point of the stress – strain curve,
$\varepsilon_{fc}(T)$ – is the strain at ultimate strain,
n – exponent n:

$$n = \begin{cases} 2 & \text{for} \quad T = 0°\text{C} \\ 1 + \dfrac{T + 170}{170} & \text{for} \quad -17°\text{C} < T < 0°\text{C} \\ 1 & \text{for} \quad T = -170°\text{C} \end{cases} \tag{3}$$

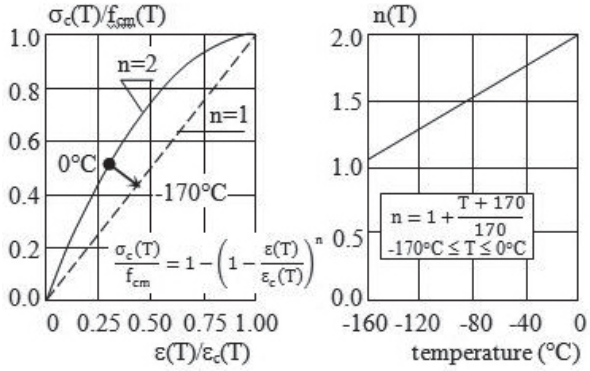

Fig. 4. Relative stress – strain relationship for concrete [9]

The ultimate strain $\varepsilon_{fc}(T)$ may be estimated as:

$$\varepsilon_{f_c}(T) = \varepsilon_{f_c}(T = 20°\text{C}) + \kappa \cdot \Delta\varepsilon_{f_c}^{\max}(T = -60°\text{C}) \tag{4}$$

where:
– concrete strain at 'normal'temperature: $\varepsilon_{fc}(T = 20°\text{C}) = 0.2\%$
– coefficient κ:

$$\kappa = \begin{cases} 1 - \left(\dfrac{T + 60}{60}\right) & \text{if} \quad T > -60°\text{C} \\ \dfrac{T + 170}{110} & \text{if} \quad -170°\text{C} < T \le -60°\text{C} \end{cases} \tag{5}$$

– maximum increase in strain experienced at –60°C:

$$\Delta\varepsilon_{f_c}^{\max} = \begin{cases} 0.1\% & \text{for Portland cement-based concretes} \\ 0.15\% & \text{for blast furnace cement-based concretes} \end{cases}$$

6.3. Concrete splitting tensile strength

The splitting tensile strength $f_{c,spli}$ can be calculated according to the expression:

MC 2010
$$f_{c,spli}(T, mc) = C \cdot f_c(T, mc)^{0.67} \tag{6}$$

The value of coefficient Cvaries between 0.3 (air-dry concrete) and 0.56 (water saturated concrete).

A similar equation for tensile strength f_{ctx} is recommended in PN-EN 1992-3 [4]:

EC2-3
$$f_{ctx} = \alpha \cdot f_{ckT}{}^{2/3} \tag{7}$$

The values of coefficient α are shown in Table 6.

Table 6

The coefficient α [4]

Tensile strength	Water saturated concrete	Dry concrete
f_{ctm}	0.47	0.30
$f_{ctk\,0.05}$	0.27	0.21
$f_{ctk\,0.95}$	0.95	0.39

6.4. Concrete modulus of elasticity

The modulus of elasticity E_c increases with decreasing temperature.According to EC2-3 [4], the influence of the moisture content on the modulus of elasticity gain ΔE_c can be estimated as:

EC2-3
$$\Delta E_c\left(T = -25°\mathrm{C}\right) \approx \begin{cases} +2\ \mathrm{GPa} & \text{for dry concrete} \\ +8\ \mathrm{GPa} & \text{for water saturated concrete} \end{cases}$$

For concrete exposed to temperature T = –165°C, the modulus of elasticity increases significantly [8]:

MC 2010
$$E_c\left(T = -165°\mathrm{C}\right) \approx \begin{cases} 1.15 \times E_c\left(T = 20°\mathrm{C}\right) & \text{for dry concrete} \\ 1.5 \times E_c\left(T = 20°\mathrm{C}\right) & \text{for sealed concrete} \\ 1.8 \times E_c\left(T = 20°\mathrm{C}\right) & \text{for water saturated concrete} \end{cases}$$

6.5. Coefficient of thermal expansion

The coefficient of thermal expansion α_T decreases with reductions in temperature. The value of coefficient α_T strongly depends on the content of free moisture in concrete (Fig. 5). In the case of water saturated concrete, expansion behaviour (negative value of coefficient α_T) should be expected. For dry concrete, the coefficient of thermal expansion decreases by approximately 10% [8].

a)

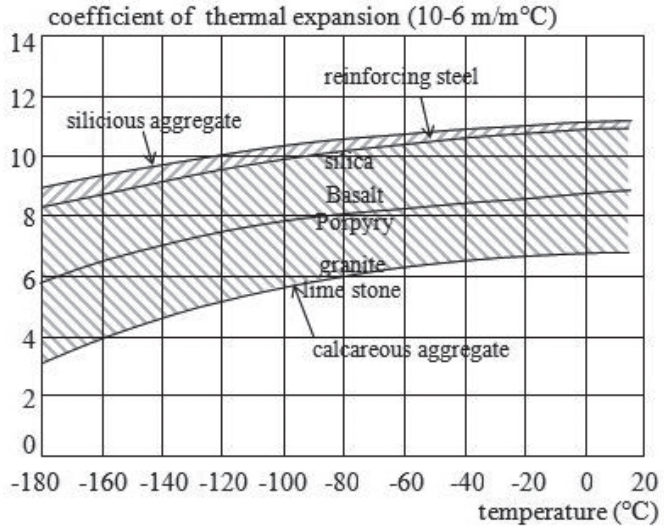

b

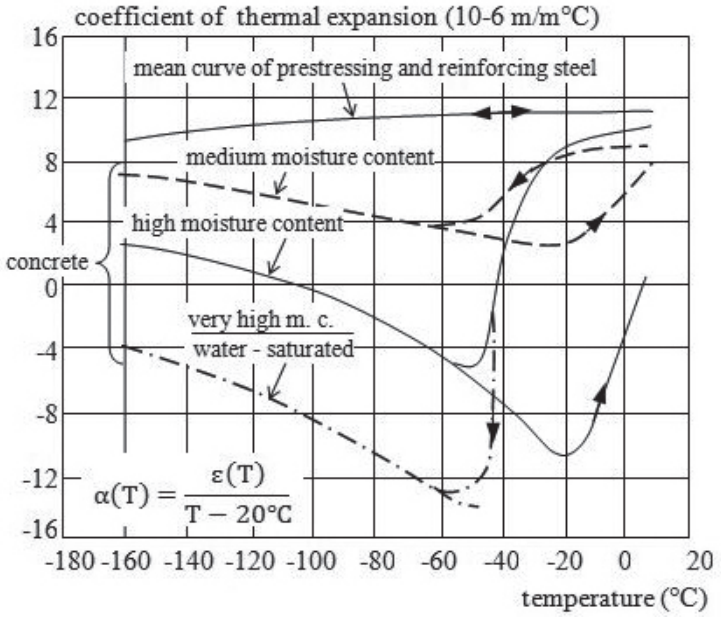

Fig. 5. Effect of a) type of aggregates, and b) moisture content, on the value of the coefficient of thermal expansion α_T [9]

6.6. Behaviour of normal and prestressed steel under cryogenic conditions

Generally, in the case of normal steel, the values of tensile strength, yield strength and the modulus of elasticity increase if the temperature decreases. The total elongation [in %] at maximum force increases initially but below –150°C, it decreases rapidly [10]. Tests on prestressing steel wires and strands showed that 0.1% proof stress and ultimate strength was higher than at room temperature and an elongation at maximum load was over 2% at temperature T = –196°C [11]. In both cases, normal and prestressing steel stress-strain diagrams are suitable for behaviour assessment at cryogenic temperature [8]. If the designed temperature is lower than –50°C, then the prestressing system (strands and anchorages) should be tested in assumed cryogenic conditions. A tensile test on notched and un-notched reinforcing steel bars should be conducted if the designed temperature is lower than –20°C [1.3].

7. Tank foundation design

Two types of foundation may be designed to prevent the ground freezing:
– shallow foundation (concrete slab on ground);
– pile foundation (elevated concrete foundation, Fig. 6).

The temperature of the concrete slab foundation should not drop below 0°C at any point. In the case of shallow foundation, a concrete slab heating system must be designed. An effective way to avoid the ground freezing is the existence of an air gap under the foundation. In this solution, the base slab is heated by natural air convection and an additional heating system for the tank foundation is not necessary.

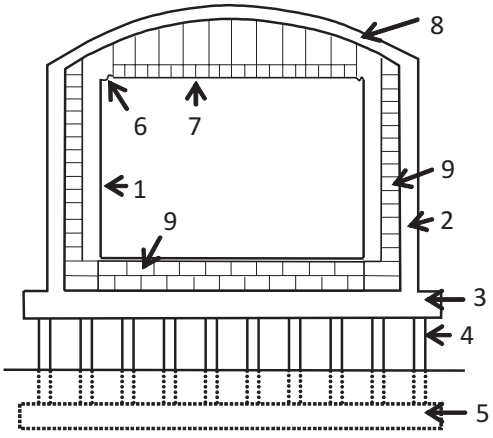

Key:
1. Primary container (steel)
2. Secondary container (prestressed concrete)
3. Elevated foundation – upper concrete slab
4. Concrete column
5. Shallow foundation concrete slab
6. Flexible insulating seal
7. Suspended roof (insulated)
8. Concrete roof
9. Thermal insulation

Fig. 6. Geometry of the cryogenic tank with pile foundation (according to EN 1473[12])

8. Summary

This paper presented some general concepts of prestressed concrete containment tank constructions, load cases or combinations and material properties under cryogenic conditions according to EN 14620 and fib Model Code 2010. It concentrated on the main differences in the design aspects of concrete tanks in the case of 'normal' and 'low' temperature.

References

[1] EN 14620:2010 Design and manufacture of site built, vertical, cylindrical, flat-bottomed steel tanks for the storage of refrigerated, liquefied gases with operating temperatures between 0°C and –165°C.
[1.1] Part 1: General;
[1.2] Part 2: Metallic components;
[1.3] Part 3: Concrete components;
[1.4] Part 4: Insulation components;
[1.5] Part 5: Testing, dryling, purging and cool-down;
[3] EN 1992-1-1:2008 Eurocode 2: Design of concrete structures – Part 1-1: General rules and rules for buildings .
[4] EN 1992-3:2008 Eurocode 2: Design of concrete structures – Part 3: Liquid retaining and containment structures.
[5] BS 777-3:1993 Flat-bottomed, vertical, cylindrical storage tanks for low temperature service.
Part 3: Recommendations for the design and construction of prestressed and reinforced concrete tanks and tank foundations, and for the design and installation of tank insulation, tank liners and tank coatings.
[6] EN 1991-4:2008 Eurocode 1 – Actions on structures – Part 4: Silos and tanks.
[7] fib Model Code 2010, Bulletin 55, First complete draft – Volume 1, March 2010.
[8] fib Model Code 2010, Bulletin 56, First complete draft – Volume 2, April 2010.
[9] Van der Veen J.C., *Properties of concrete at very low temperatures. A survey of the literature*, Report No. 25–87–2. Delft University of Technology, 1987.
[10] FIP Special Report SR 88/2: Information on the behaviour at very low temperatures of ribbed steels, June 1988.
[11] FIP State of the Art Report: Cryogenic behaviour of materials for prestressing concrete, 1982.
[12] EN 1473:2007 Installation and equipment for liquefied natural gas –Design of onshore installations.

TECHNICAL TRANSACTIONS | CZASOPISMO TECHNICZNE
CIVIL ENGINEERING | BUDOWNICTWO
3-B/2015

MARCIN MIDRO*, ŁUKASZ ŚLAGA*

TECHNICAL CONDITION ASSESSMENT AND CONSTRUCTION SOLUTION OF RC DIGESTION CHAMBER STRENGTHENING

OCENA STANU TECHNICZNEGO ORAZ SPOSOBY WZMOCNIENIA ŻELBETOWEJ POWŁOKI STOŻKOWEJ KOMORY FERMENTACYJNEJ

Abstract

This paper presents the technical condition assessment of a RC digestion dome chamber after fourteen years of exploitation. The authors conducted experimental investigations, i.e. tests of concrete compressive strength using a scleroscope, concrete chemical analysis in the laboratory and detections of reinforcement. On the basis of the obtained results and cracks morphology, static-strength calculations were conducted. The results of the FEM numerical analysis indicated deficiencies in the bearing capacity of the dome. The widths of the calculated cracks exceeded allowable values. The authors proposed two alternative methods of chamber strengthening: pouring additional RC dome cover or post-tensioning the dome with external unbonded tendons.

Keywords: *digestion chamber, tank dome, tank strengthening, unbonded tendons*

Streszczenie

W artykule przedstawiono analizę stanu technicznego powłoki stożkowej przekrywającej zamkniętą komorę fermentacyjną po 15 latach eksploatacji. Podstawą do określenia nośności i obliczeń numerycznych były badania sklerometryczne, analiza chemiczna betonu, inwentaryzacja zbrojenia oraz powstałych rys. Wyniki analizy wykazały niedobór nośności w przekrojach charakterystycznych kopuły i przekroczenie dopuszczalnych wartości rozwarcia rys. Na tej podstawie zaproponowano dwa alternatywne sposoby naprawy uszkodzeń oraz wzmocnienia kopuły: wersję żelbetową z dodatkowym zewnętrznym płaczem oraz wersję sprężoną cięgnami zewnętrznymi bez przyczepności.

Słowa kluczowe: *cięgna bez przyczepności, powłoka stożkowa, wydzielona komora fermentacyjna, wzmocnienie zbiornika*

DOI: 10.4467/2353737XCT.15.167.4342

* M.Sc. Eng. Marcin Midro, M.Sc. Eng. Łukasz Ślaga, Institute of Building Materials and Structures, Faculty of Civil Engineering, Cracow University of Technology.

1. Introduction

The basic requirement for liquid storage tanks is their tightness [1, 2]. The serviceability limit state of tanks is believed to be critical in terms of the elements dimensions (thicknesses), the quality of materials (including the concrete class and special properties e.g. water-tightness) and the amount of required reinforcement [13]. Tank designers should take into account the possibility of water-tightness loss during all stages of erection (e.g. early age cracking [8]) and operation of the structure (tank overflow, thermal loads in summer/winter season). Thus, the design process seems to be more complicated due to the additional requirements for construction materials and the technology of construction.

In most cases, the loss of water-tightness of any of the components in the reservoir means disruption in the operation of the tank. This is aimed at the protection of water purity in the water supply tanks and the prevention of polluting the environment with sewage or industrial waste water. On the other hand, any pause in plant operation leads to additional costs. The intensive development of new methods and materials for protection and repair, results in the need to formulate new standards for these kinds of works and products. Ten fundamental and sixty-five additional standards were proposed in the series of European standards EN 1504.

The article presents two alternative solutions for dome repair in the separated digester tank. The tank was out of use following eleven years of service due to numerous leaks in the conical shell. The first repair method considers the injection of cracks and pouring additional RC coat on the existing dome. In the alternative solution, the authors proposed the post-tensioning of the existing dome with external unbonded tendons. This method was implemented for the first time in Poland by the Chair of Prestressed Structures and the Laboratory of Building Materials and Structures at the Cracow University of Technology for strengthening the conical dome and the conical bed of the tanks. For each method, a simplified cost repair analysis has been prepared.

2. State of emergency

The analysed digestion chamber tank (Fig. 1) was erected in the time period between September 1997 and May 1999. The tank has been in use for more than eleven years. The flood in May 2010 resulted in long-term facility downtime (over two years), causing sludge sedimentation and clogged pipelines. In July 2012, the renovation work began which involved the mechanical removal of the old coatings by abrasive blasting (sandblasting) from the walls and the dome and the laying of a new two-component epoxy resin without any additional sealing. The contractors did not prepare the technical condition assessment of the dome surface before placing the resin coating. The repair works lasted until the end of August 2012. In October 2012, the engineers decided to fill the tank with the water at a rate of 10 m^3/h for a period of around eight hours per day. In November 2012, the first leaks on the dome surface were noticed and the administrator was forced to stop the process of tank filling. After a partial outcrop of the dome external surface, numerous cracks were discovered. The two widest cracks were oriented in a circumferential direction. Smaller cracks were located in a radial direction.

Fig. 1. The view of the two digestion chamber tanks (analysed tank on the right)

3. Tank description

The analysed digestion chamber was made using traditional technology as a monolithic, reinforced concrete cylindrical tank with an inner radius of 7.5 m and a wall thickness of 0.60 m. The bottom of the tank is a conical shell with a thickness of 0.60 m. The connection of the conical bottom plate to the cylindrical tank wall is monolithic. The tank wall is monolithically connected with a conical dome (0.25 m thick). The dome is completed with an internal RC cylindrical shell with a thickness of 0.25 m. The inner diameter of the internal shell is 4.30 m. The covering slab has a ring-shaped design. The tank geometry is presented in Fig. 2.

The wall and the dome of the tank is made of water resistant and frost resistant concrete B30 F150 W8, which corresponds to today's class C25/30 F150 W8. The concrete mixture was made with crushed basalt aggregate and Portland cement with additives corresponding to the current grade CEM II 32.5N. The nominal cement content was 350 kg/m^3 and the water-cement ratio was 0.4.

The tank wall, with a total height of 11.00 m, was erected in five sections of concreting. Each section involved concreting a two-meter high wall segment. The last 1.00 m wall segment was concreted with the conical shell. During concreting, a set of cubic samples (0.15 m × 0.15 m × 0.15 m) was prepared. On the basis of site documentation, the average cubic concrete compressive strength was 46.0 MPa; 50.2 MPa; 51.5 MPa; 43.7 MPa and 46.2 MPa (in each concreting section). Thus, the elements met the requirements of the assumed concrete class.

The dome reinforcement was made of steel grade A-III (34GS). The dome was reinforced with #10 mm bars in circumferential and radial directions. The bar spacing was 0.07–0.1 m in a circumferential direction and 0.20 m in a radial direction (on the inner and outer surfaces of the dome). The nominal concrete cover was assumed to be 40 mm.

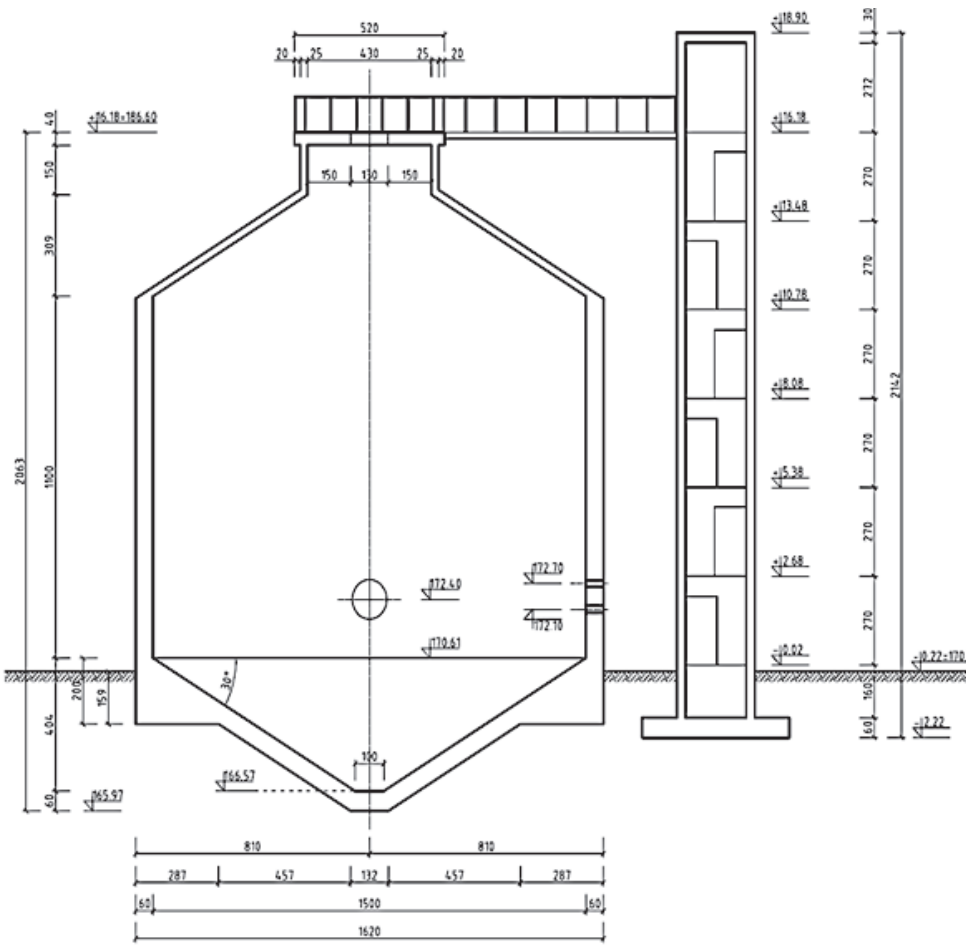

Fig. 2. The vertical cross-section of the tank

4. Experimental investigations

In order to determine the causes of the emergency state and propose the method for the restoration of the tank's chamber, an experimental test program was prepared [4, 7, 12]. The experimental studies consisted of a site investigation, sampling, and laboratory tests in the laboratory of building materials and structures at Cracow University of Technology. The experimental investigations included: an inventory of cracks; non-destructive testing methods to assess concrete strength; verification of reinforcement quantity, diameter and position; chemical analysis of the dome's concrete.

4.1. Crack morphology

The morphology and the widths of the cracks on the outer surface of the dome are presented in Fig. 3. The on-site inspections revealed that there were two main circumferential and forty smaller radial cracks. The first circumferential crack was located at the connection of the cylindrical wall with the dome and the second was at a distance of about 2.40 m from the edge of the cylindrical wall. The width of the circumferential cracks varied from 0.3 to 0.6 mm (for one crack) and from 1.4 to 2.5 mm (for the other crack). The radial cracks widths ranged from 0.2 mm to 1.1 mm. During the on-site investigation, it was found that there were prior attempts to seal the cracks before installing the insulating layer.

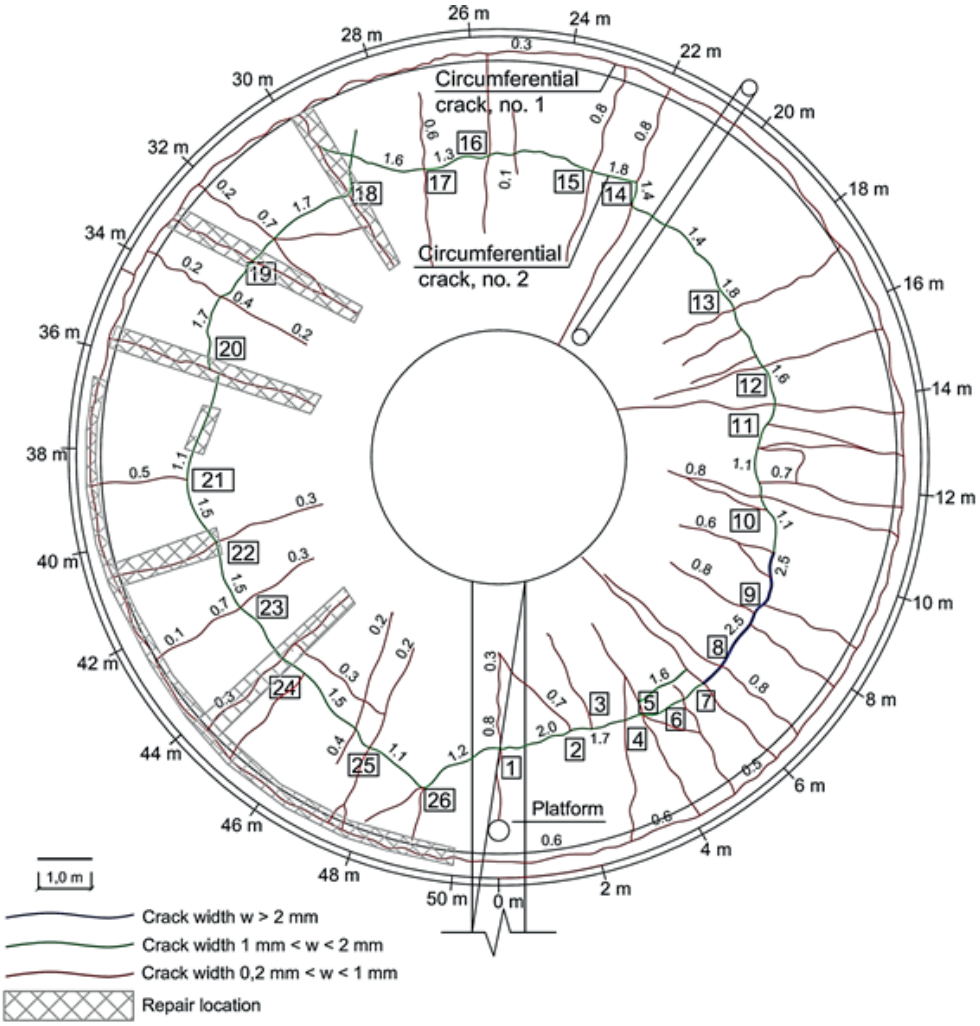

Fig. 3. The view of crack morphology on the outer surface of the tank's dome

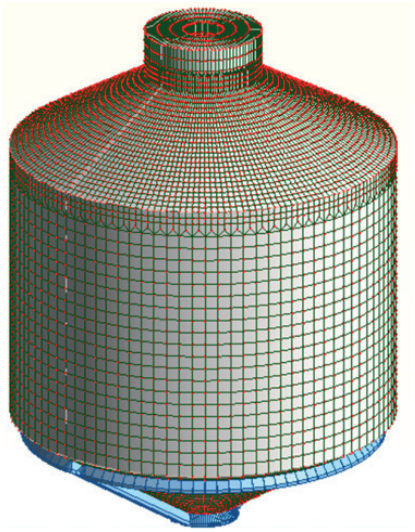

Fig. 4. The FEM model of the tank

In order to investigate the behaviour of the digestion chamber dome, a FEM model of the tank was prepared (Fig. 4). In the calculations, all possible, relevant loadings during erection and operation were taken into consideration. The digestion chamber dome was analysed: at the different stages of loading (empty, full tank, temporary overflow in the emergency situation); for different thermal loads (winter and summer season) and for different thermal isolation thicknesses.

The distribution of radial stresses on the dome's inner and outer surfaces under operation and emergency (tank overflow) loading are shown in Fig. 5. The distribution of circumferential stresses on the dome's inner and outer surfaces under operation and accidental loading are shown in Fig. 6.

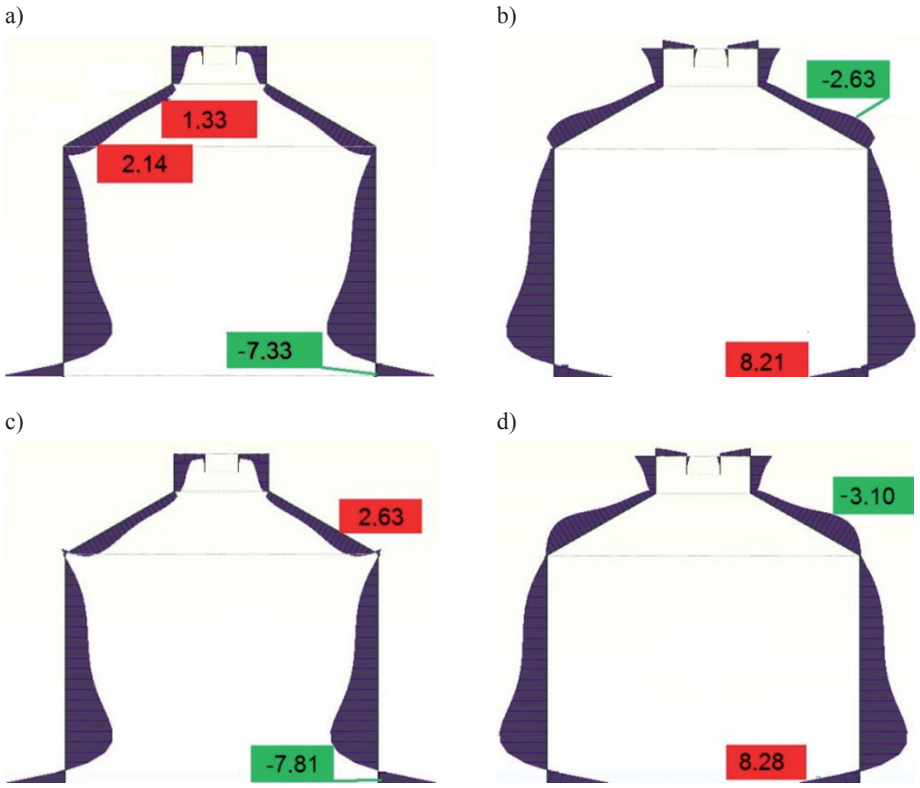

Fig. 5. The distribution of radial stresses: a), b) on the inner and outer surface during operation; c), d) on the inner and outer surface in the accidental (tank overflow) situation

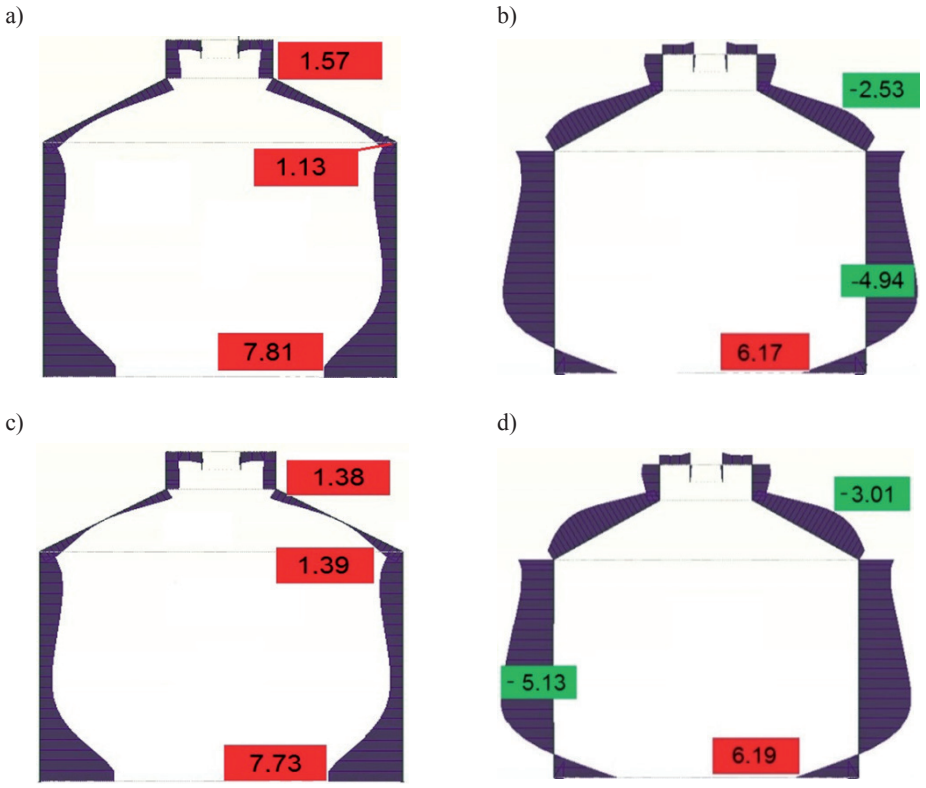

Fig. 6. The distribution of circumferential stresses: a), b) on the inner and outer surface during operation; c), d) on the inner and outer surface in the emergency (tank overflow) situation

The maximum tensile stresses in a radial direction on the outer surface of the dome were σ_r = 3.10MPa and σ_r = 2.63MPa during operation and emergency situation. In both situations, maximum tensile stresses occurred approximately 2.4 m from the outer edge of the tank wall and exceed the tensile strength of the concrete (f_{ctm} = 2.6 MPa for C25/30). In a circumferential direction, only loads acting in the emergency situation caused an excess of stresses: σ_ϕ = 3.01 MPa over the medium concrete tensile strength.

On the basis of the obtained results, it was found that the first circumferential crack (at the connection of the cylindrical wall with the conical dome) was caused by a rapid change in the shell stiffness. It is recommended to design a transitional element between the wall and the dome. Probably the second circumferential crack was developed in the winter during the first year of operation, in the line of the maximum stresses produced by hydrostatic pressure and temperature gradient. And then, the stresses at the second circumferential crack exceed the medium axial tensile concrete strength. Moreover, crack width calculations in accordance with Eurocode 2 [1, 2] resulted in a value of 0.235 mm. The crack width of 0.235 mm satisfies the serviceability limit state of normal reinforced concrete structures but does not meet crack width criteria for waterproof structures. The rapid propagation of circumferential cracks and

the formation of radial cracks occurred as a result of hydrostatic pressure in the emergency state during the flood in May 2010 (clogged pipelines and tank overflow).

4.2. Concrete compressive tests using a scleroscope

Concrete compressive strength was estimated based on a series of tests conducted at twelve measuring points. The obtained results were corrected, taking into account the age of concrete, surface moisture conditions and the angle of the sclerometer during the tests. The average compressive strength determined on cube samples of 150 mm × 150 mm × 150 mm was $f_{cm.cube}$ = 31.98 MPa with a standard deviation of s = 3.56 MPa and a variation coefficient of ν = 6.68%.

4.3. Reinforcement detection

The authors used a ferrodetector to determine the position of the steel rebars, their diameter and the thickness of concrete cover. Tests were conducted at 17 measuring points and proved that the diameter of reinforcement and the spacing of rebars met the design assumptions. The thickness of the concrete cover varied from 51 mm to 77 mm.

The authors speculate that at the erection state, the contractors did not use stabilising rods for the upper and lower reinforcement mesh. The increased concrete cover thickness resulted in a decrease of the internal forces arm and a reduction in the load-bearing capacity.

4.4. Chemical analysis

The obtained results of chemical analysis showed a similar pH value in five out of six samples and varied from 11.30 to 12.00. The pH values of the water extract were higher than the minimum (pH = 10.80) which provides the protective properties of reinforcing. The pH of the specimen sampled directly from a circumferential crack area was below the limit. The results are shown in Table 1.

Table 1

The results of concrete chemical analysis

No.	Depth of concrete cover [outer layer, 0–10 mm]	pH value	Cl^- [% weight of cement]
1	K-K 1/A	11.75	0.17
2	K-K 2/A	11.30	0.23
3	K-K 3/A	11.55	0.22
4	K-K 4/A	12.00	0.27
5	K-K 5/A	11.70	0.26
6	K-K 6/A	9.95	0.33

Contamination of chloride ions in the dome cover does not exceed the limit value, which is 0.4% of the weight of the binder for reinforced concrete structures [3].

The chemical analysis of the outer concrete layer of the dome (0÷10 mm) shows that despite the existence of the thermal insulation layer (50 mm thick expanded polystyrene), the process of carbonation in the area of the first circumferential crack proceeded in a similar way as for the exposed concrete surface (RH = 40%÷60%). Thus, the insulation layer has not been properly air sealed.

5. Strengthening of the dome

On the basis of numerical analysis, two alternative methods of tank dome repair were proposed.

5.1. Additional RC shell

The first solution of repairing the dome considers pouring an additional RC dome cover. This method proposes to seal existing cracks with epoxy injection resin – this would be applied to all cracks. The additional RC shell (Fig. 7–8) is designed of concrete class C30/37 W10. The extra cover is reinforced by a single reinforcement mesh (Fig. 7–8). The designed reinforcement meets the requirements of both the ultimate limit state and the minimum reinforcement ratio due to crack width control. The contact between the new concrete shell and the dome is provided by rebars anchored in the existing dome in a direction perpendicular

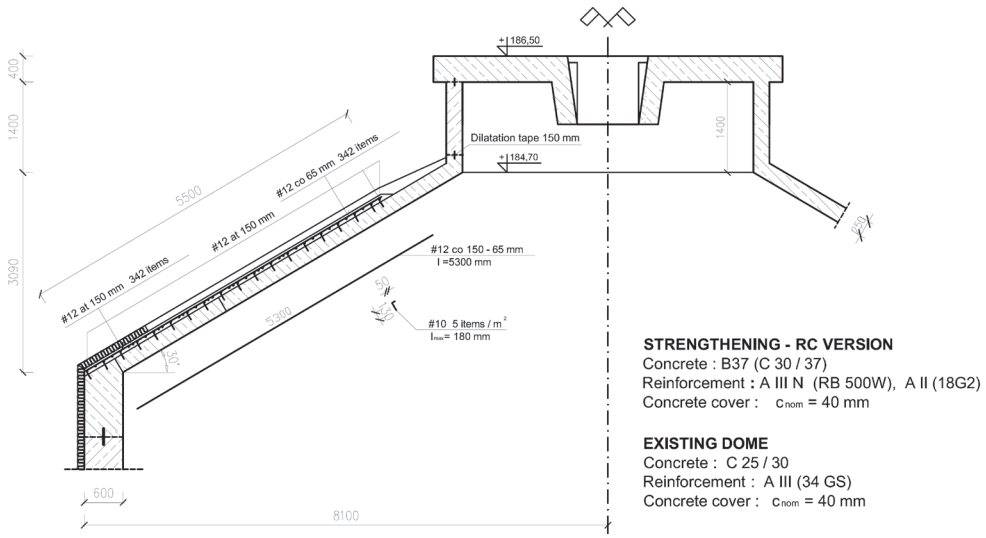

Fig. 7. Cross-section of composite shell

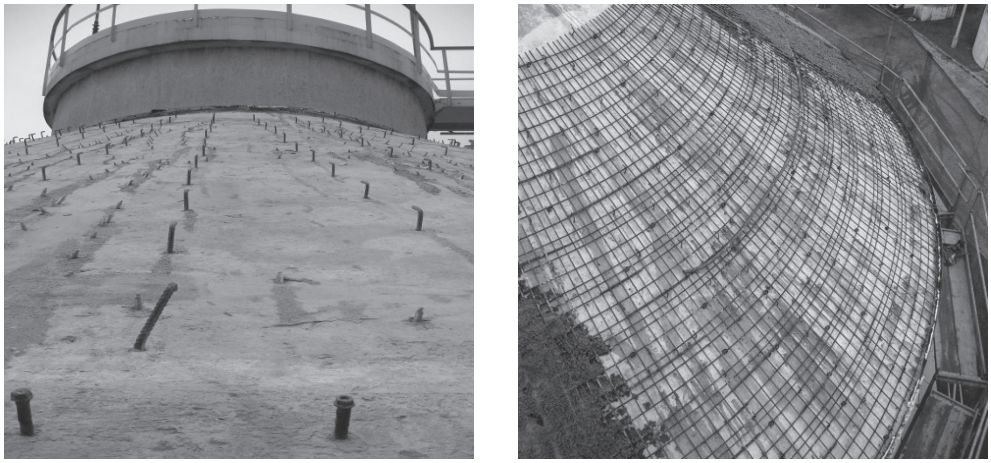

Fig. 8. Strengthening of the dome during concreting (RC version)

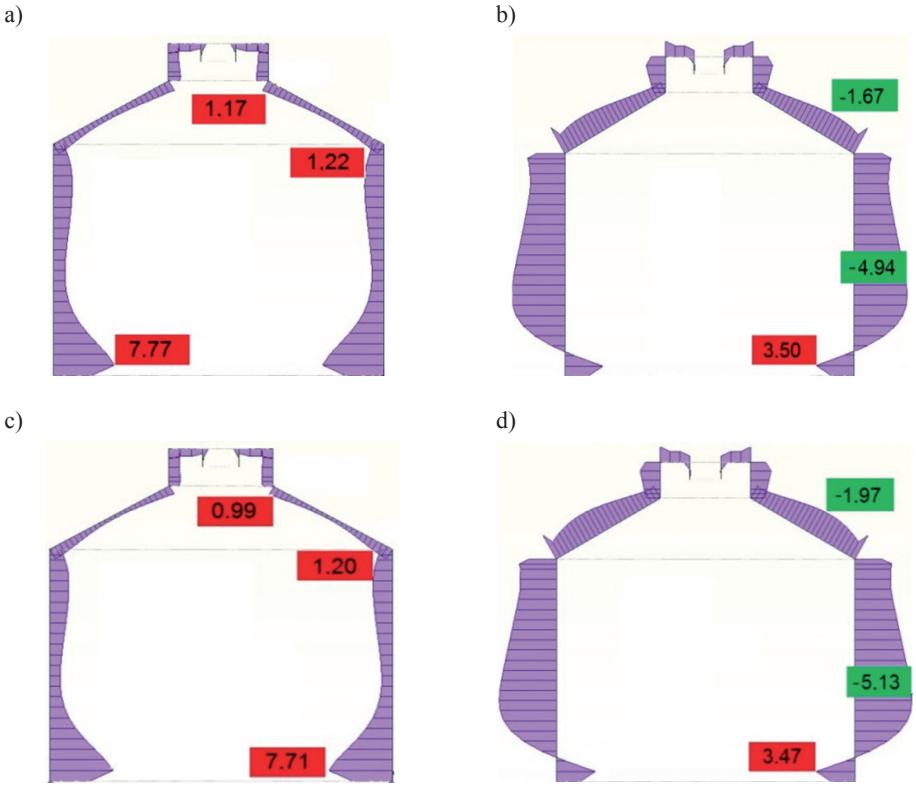

Fig. 9. The distribution of radial stresses in composite cross-section: a), b) on the inner and outer surfaces during operation; c), d) on the inner and outer surfaces in the emergency situation

to its surface. Due to the limited additional shell thickness (100 mm) and rough surface of the existing dome, it would be impossible to pour a normal concrete mixture into the mold and compact it. On the other hand, the use of self-compacting concrete requires a high bearing capacity and sealed formwork due to increased mixture pressure; therefore, it was decided to use a normal concrete mixture of consistency K2 to be applied without surface formwork. Only at the outer edge of the tank wall was a ring formwork used to prevent the concrete mixture from slipping down.

In order to investigate the behaviour of the composite cross-section consisting of a RC dome (250 mm thick) and additional RC shell (+100 mm thick) static calculations have been prepared. The distribution of the radial stresses in the composite cross-section of the dome's inner and outer surfaces under operation and emergency (tank overflow) loading are shown in Fig. 9. The distribution of the circumferential stresses in the composite cross-section on the inner and outer dome's surface under operation and emergency loading are shown in Fig. 10.

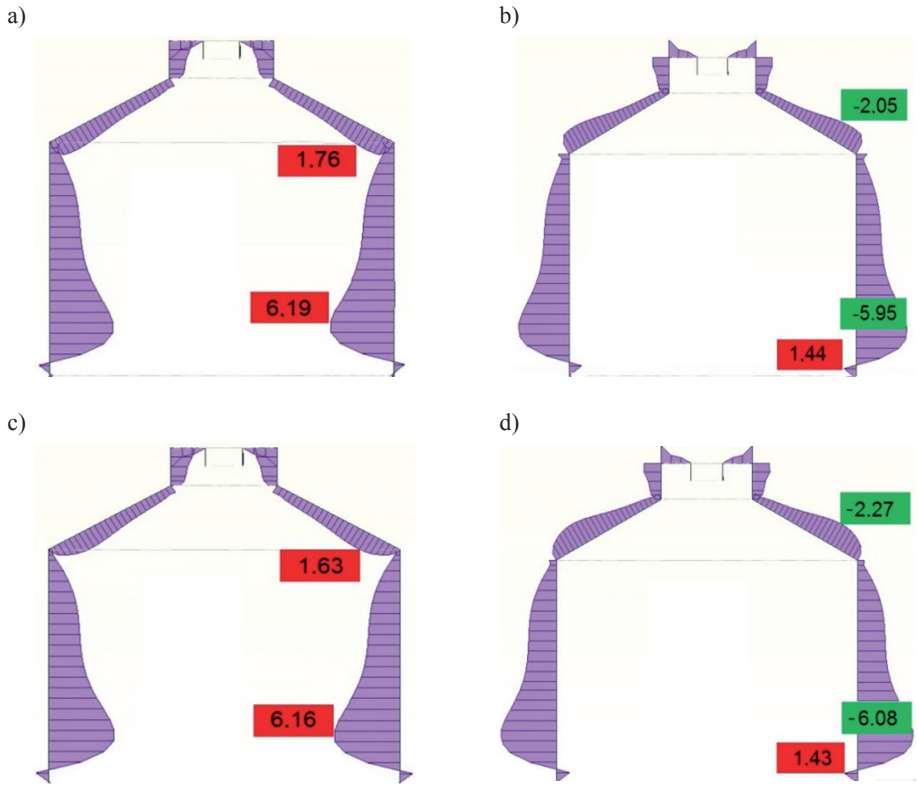

Fig. 10. The distribution of circumferential stresses in composite cross-section: a), b) on the inner and outer surfaces during operation; c), d) on the inner and outer surfaces in the emergency situation

The maximum tensile stresses on the outer surface of the composite cross-section in a radial direction were σ_r = 1.67 MPa (during operation) and σ_r = 1.97 MPa (in emergency situation). In a circumferential direction, the maximum stresses were σ_ϕ = 2.05 MPa and σ_ϕ = 2.27 MPa respectively during operation and the emergency situation. The stresses in the concrete composite shell do not exceed the mean value of concrete tensile strength (f_{ctm} = 2.9 MPa for the concrete class C30/37). Moreover, pouring an additional RC dome cover does not result in a significant increase of tensile forces in the circumferential ring around the tank's dome.

5.2. Post-tensioning of the dome

The second repair method considers the use of steel deviators and external unbonded tendons for post-tensioning of the tank's dome [9–12, 14]. This would provide compressive stresses in the tank's dome cross-sections. It is proposed to seal the forty smaller existing radial cracks with polypropylene injection resin and the two main circumferential cracks with epoxy resins. After injecting and filling the tank, the first tightness test should be carried out.

The static-strength analyses included: selection of the tendons and dimensioning additional elements-deviators, calculations of prestressing force and losses, verification of efficiency in terms of Serviceability Limit State and Ultimate Limit State.

Due to the necessity of limiting post-tensioning force losses, the authors decided to use unbonded steel tendons 7ϕ5. It was found that the RC tank's dome should be prestressed in a circumferential direction with a tendon length of up to 32 m. Tendons with a nominal diameter of 15.7 mm and cross-section area A_{p1} = 150 mm^2 (Y1860S7, f_{pk} = 1860 N/mm^2) were installed in plastic ducts. In order to ensure the durability of the tendons and minimize contact stresses, a four-layer protection system has been introduced. The system consists of: a petroleum grease; a leak-tight, corrosion-resistant plastic duct; mortar grout (between the duct and the plastic pipe); plastic pipe.

The required post-tensioning force was estimated on the basis of static-strength analyses conducted during the assessment of the technical condition. It was required to use circumferential tendons, each tendon post-tensioned with the force of 220kN. The prestressing force was introduced to the FEM model [5, 6] as an equivalent concentrated load consisting of horizontal and vertical components (slope of the dome α = 30°). The calculations also take into account the cam of prestressing force (average moment M_{Pmt} about 12.4 kNm).

The stress state analyses concerned:

– initial situation – empty tank in the winter season,
– operation situation – filled tank in the winter season,
– emergency situation – tank overflow.

The post-tensioning forces should provide compressive stresses in the dome during all operation stages (full and empty tank). Only in the emergency situation are tensile stresses allowed to occur, but their value should not exceed the medium tensile strength of concrete ($\sigma_t \leq f_{ctm}$). The calculated post-tensioning force after immediate losses was 197 kN and after long-term losses, it was 186 kN. Spacing between the tendons conform to tensile force distribution (Fig. 11) and vary along the conical dome.

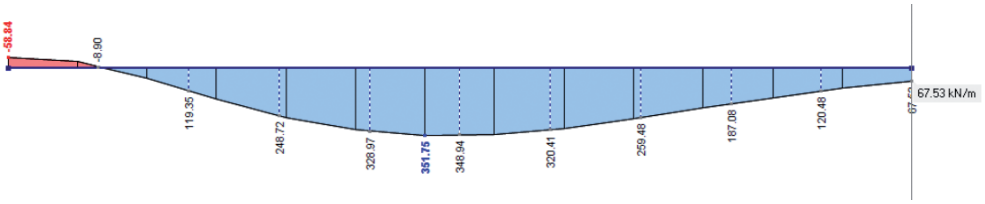

Fig. 11. Circumferential tensile forces due to hydrostatic pressure in the emergency situation

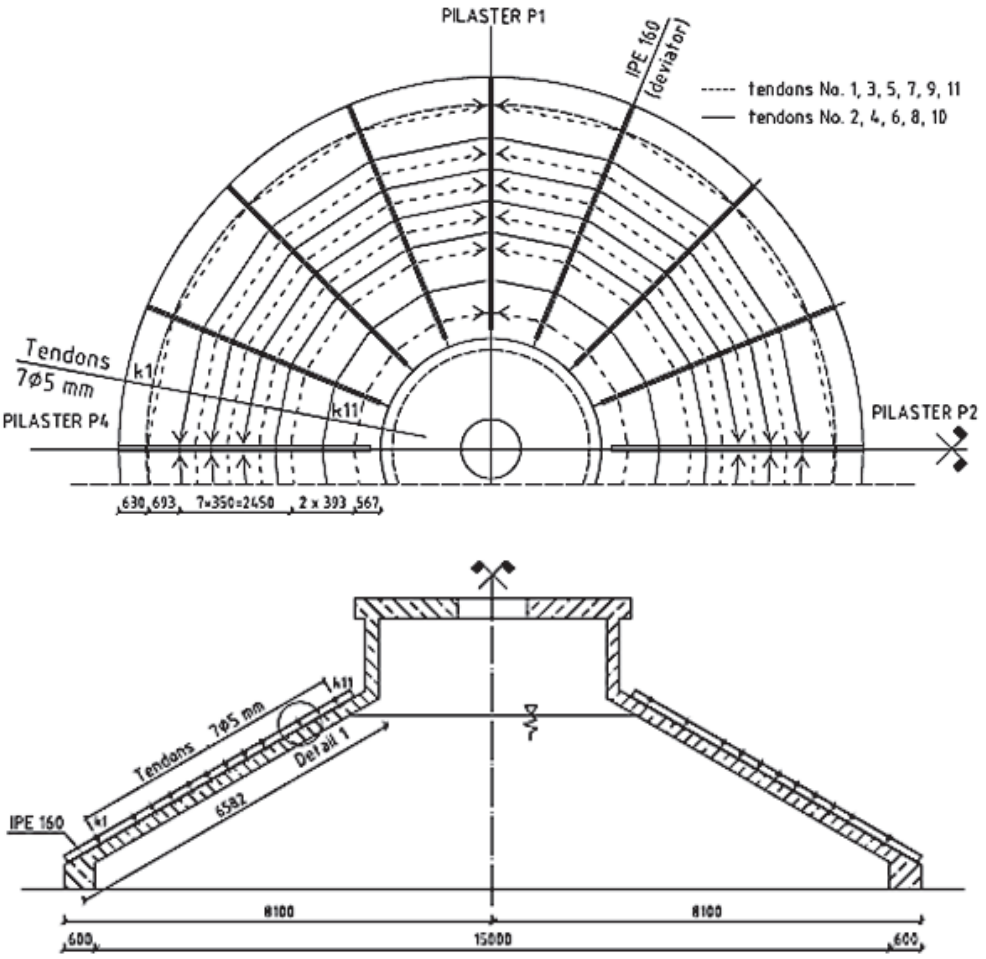

Fig. 12. Arrangement of deviators, pilaster and the tendons

In order to transfer the prestressing force to the dome's cross-section, steel deviators were designed. The deviators were made of 16 steel profiles IPE 160 and four box-section beams. The elements attached to the reinforced concrete dome using anchors. The dome has been

divided into 16 parts, each with a cone angle of 22.5°. Four box-section beams were used as pilasters for the anchoring of tendons. The beams were designed symmetrically every 90°. Due to increased losses of prestressing force in two peripheral tendons, each circuit has been divided into 2 sections anchored in four pilasters. The rest of the circuits consisted of only one section anchored in two pilasters.

All tendons are stressed from one side only using a hydraulic jack and are fastened by wedge grips at the live end, as shown in Fig. 13, and swage type anchorages at the dead end. Spacing between the tendons varies from 400 mm in the area of maximum circumferential tensile stresses to 800 mm in the edge zones (Fig. 12). In the places provided for the location of tendons, the web of the profile has been cut and the additional components consisting of teflon coated curved steel sheets have been installed (Fig. 14).

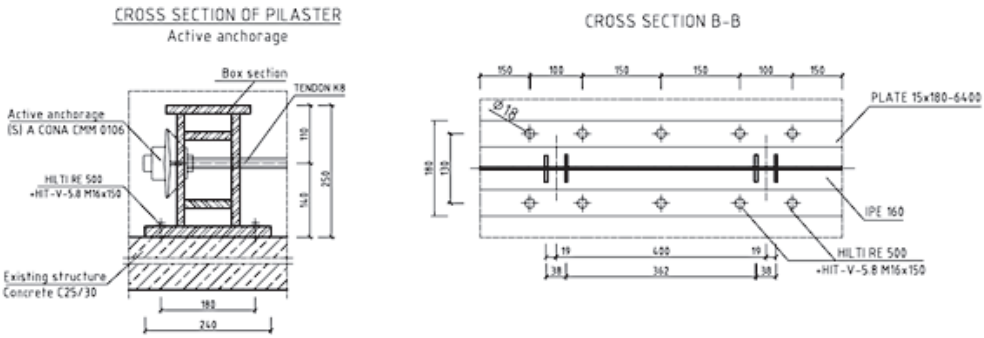

Fig. 13. The detail of the anchorage design solution

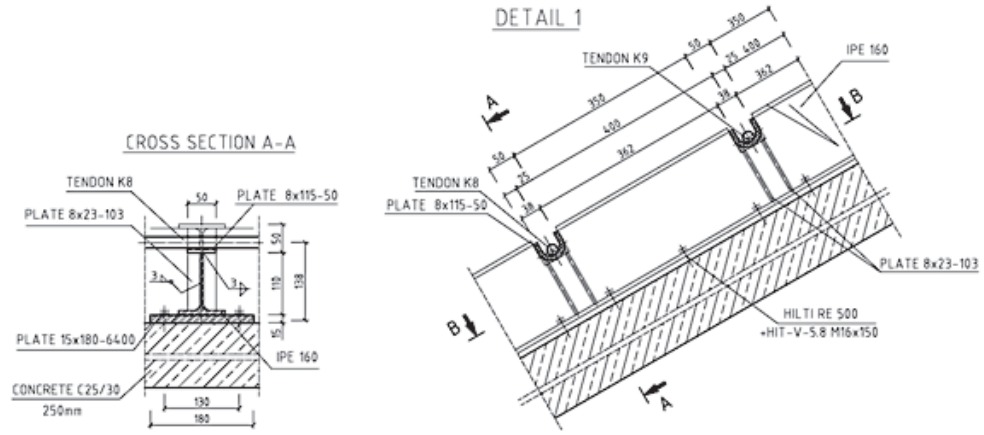

Fig. 14. The detail of the steel deviator

It has been found that the maximum tensile stresses occur in the emergency situation (during tank overflow) in the centreline on the outer surface of the dome and are equal to $\sigma_{ct} = -2.02$ MPa (in a radial direction). Tensile stresses in other parts of the dome vary from

–0.10 MPa to –1.45 MPa in the initial situation and from –0.32 MPa to –1.86 MPa during the tank's operation. The maximum compressive stresses are σ_{cc} = = 3.74 MPa (in a circumferential direction).

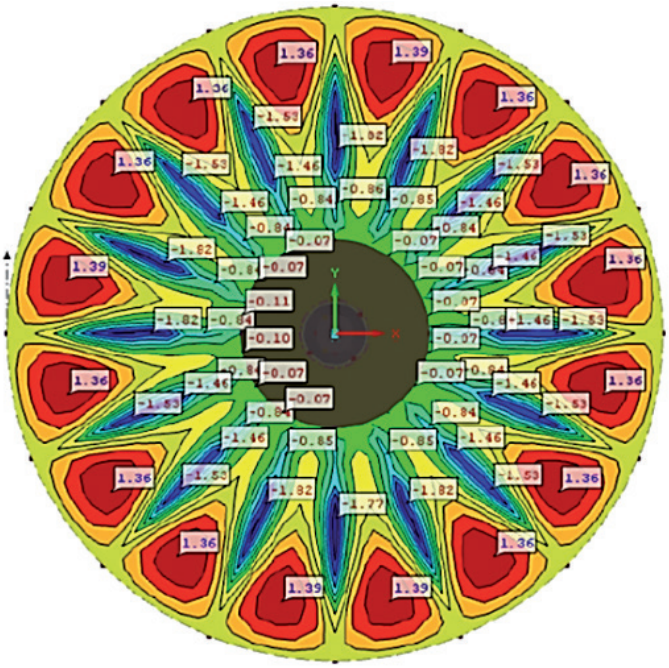

Fig. 15. The distributions of circumferential stresses on the outer surface of the tank's dome in the emergency situation

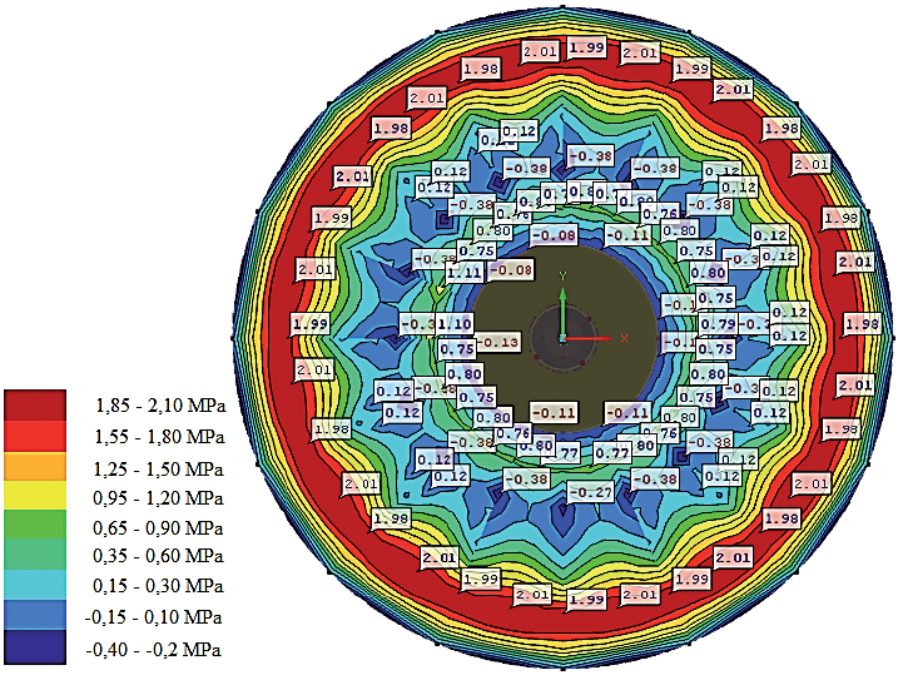

Fig. 16. The distributions of radial stresses on the outer surface of the tank's dome in the emergency situation

The distributions of circumferential and radial stresses on the outer surface of the tank's dome in the emergency situation are shown in Fig. 15 and Fig. 16.

The tensile stresses are lower than the medium concrete tensile strength. Therefore, reopening of the cracks is unlikely.

6. Conclusions

The assessment of the technical condition of the existing structure revealed an underestimation of the required reinforcement at the design stage. The reinforcement ratio did not meet the requirements of minimum reinforcement according to EC2. Moreover, an insufficient thermal insulation layer created additional stresses in the dome cross-section. The proper strategy of thermal insulation in terms of its thickness and materials plays a vital role in the static-strength behaviour of the tanks subjected to temperature gradients. In order to improve the thermal properties of the partition, thermal insulation layer was increased to 120 mm for both versions of the repair.

Maintaining tightness throughout the life of the structure is a problematic task in the case of pouring an additional RC shell due to the occurrence of tensile stresses in the cross-section. In the post-tensioned dome, prestressing forces produce compressive stresses in the dome cross-section. On the other hand, the additional shell method is simpler in terms of contractors' qualifications and the required equipment. However, concreting can take place only under favourable weather conditions (absence of rainfall and air temperature similar to the temperature of the tank – elimination of thermal stresses at the connection surface). This is an important factor because it determines the period of the tank's downtime – this has significant financial implications for the investor.

In both versions, special attention should be paid to proper sealing execution. This is particularly important in the case of pouring an additional RC shell. Thus, the works related to the sealing of the structure must be completed with tank tightness testing.

References

[1] EN 1992-1-1:2008, Eurocode 2: Design of concrete structures. Part 1-1: General rules and rules for buildings.
[2] EN 1992-3:2006, Eurocode 2: Design of concrete structures. Part 3: Liquid retaining and containment structures.
[3] EN 206-1:2000, Concrete. Specification, performance, production and conformity.
[4] Drobiec Ł., Jasiński R., Piekarczyk A., *Diagnostyka konstrukcji żelbetowych*, *Metodologia, badania polowe, badania laboratoryjne betonu i stali*, Tom 1, PWN, Warszawa 2010.
[5] Kot M., *Design for dome strengthening of separated digester tank*, MA thesis, Cracow University of Technology, Cracow, 2015, 126 (in Polish).
[6] RFEM 5.02, Program FEM, Dlubal Software GmbH, 2013.

[7] Seruga A., Seruga T., Midro M., *Modernizacja Wydzielonych Komór Fermentacyjnych po czterdziestu pięciu latach eksploatacji*, Czasopismo Techniczne, 2-B/2011.
[8] Seruga A., Zych M., *Research on Thermal Cracking of a Rectangular RC Tank Wall under Construction*, I: Case Study, Journal of Performance of Constructed Facilities, 10.1061/(ASCE) CF.1943-5509.0000704, 04014198, Dec 2014.
[9] Libura S., *Sprężanie konstrukcji kołowo-symetrycznych cięgnami bezprzyczepnościowymi*, X Międzynarodowa Konferencja Żelbetowe i Sprężone Zbiorniki na Materiały Sypkie, Kraków 1995, 341–348.
[10] Dyduch K., Płachecki M., Sieńko R., *Wzmocnienie żelbetowej komory fermentacyjnej i odbudowa jej przekrycia stożkowego po wybuchu*, Inżynieria i Budownictwo, 12/2013, 642–654.
[11] Fuzier J.P., Berger K., Zakrzewski S., *Niskotarciowy system sprężania zewnętrznego w naprawie i wznoszeniu konstrukcji o przekroju kołowym*, X Międzynarodowa Konferencja Żelbetowe i Sprężone Zbiorniki na Materiały Sypkie, Kraków 1995, 205–215.
[12] Runkiewicz L., Lewiński P., *Diagnostyka, wzmacnianie i monitorowanie żelbetowych i sprężonych zbiorników na materiały sypkie i ciecze*, Przegląd Budowlany, 10/2014, 23–32.
[13] Halicka A., Franczak D., *Projektowanie zbiorników żelbetowych. Zbiorniki na ciecze*. PWN, Warszawa 2013.
[14] Gwoździewicz P., Miernik T., Smaga A., *Trwałość wzmocnień żelbetowych zbiorników cylindrycznych metodą sprężania cięgnami*, XIII Konferencja Żelbetowe i Sprężone Zbiorniki na Materiały Sypkie i Ciecze, Wrocław–Szklarska Poręba 2007.

TECHNICAL TRANSACTIONS | CZASOPISMO TECHNICZNE
CIVIL ENGINEERING | BUDOWNICTWO
3-B/2015

MICHAŁ MUSIAŁ*

YOUNG'S MODULUS TEST IN TWO DIRECTIONS ON THE BASIS OF EIGENFREQUENCIES IN CONCRETE BEAMS

BADANIE MODUŁU YOUNGA W DWÓCH KIERUNKACH NA PODSTAWIE CZĘSTOTLIWOŚCI WŁASNYCH BELEK BETONOWYCH

Abstract

This paper covers the experimental studies of Young's modulus of concrete on the basis of eigenfrequencies. Experiments were performed on beam elements measuring 1050 × 200 × 100 mm, using operational modal analysis (OMA). Two types of concrete with different mixtures were tested. The dynamic Young's modules were calculated on the basis on the resonant frequencies measured in two directions. The values obtained were compared with static Young's modules determined on concrete cylinders in axial compression testing.

Keywords: *concrete, eigenfrequency, OMA, Young's modulus*

Streszczenie

W artykule zrelacjonowano badania eksperymentalne modułu Younga betonu na podstawie częstotliwości własnych. Eksperymenty przeprowadzono na elementach belkowych o wymiarach 1050 × 200 × 100 mm z wykorzystaniem operacyjnej analizy modalnej (OMA). Przebadano dwa betony o różnych recepturach. Dynamiczne moduły Younga obliczono na podstawie pomierzonych w dwóch kierunkach częstotliwości własnych. Uzyskane wartości porównano ze statycznymi modułami Younga określonymi na betonowych walcach w próbie osiowego ściskania.

Słowa kluczowe: *beton, częstotliwość własna, OMA, moduł Younga*

DOI: 10.4467/2353737XCT.15.168.4343

* Ph.D. Eng. Michał Musiał, Faculty of Civil Engineering, Wroclaw University of Technology.

1. Introduction

Young's modulus is a key deformability parameter of concrete – its value may be determined in accordance with different procedures. Normally, this involves a static load test to the point of destruction in accordance with the appropriate program and determining the value of Young's modulus for the corresponding load range (e.g. [2, 4]). Due to the high popularity of non-destructive methods [5], attempts are made to use them in testing. One of the most popular methods for the indirect determination of Young's modulus is an eigenfrequency test of the element.

There have been multiple publications concerning the described method. Furthermore, it has been regulated by a relevant standard [1]. Usually, the conducted tests compare the values obtained in the classic static axial load compression test E_{cm} with values calculated on the basis of the eigenfrequency E_d. Selected results of the conducted tests prove that these values may differ. These differences may reach 10% [6, 7]; however, in some of the experiments [10, 11], they are larger and reach approx. 30%. Mostly, the dynamic Young's modulus is a greater value. Nevertheless, results of tests are available where the trend was reversed.

So far, tests have been performed on different test elements. While in the case of the static Young's modules, these are mainly cylinders, in the case of the dynamic modulus, the tests were conducted on cylinders [7, 10] as well as on beam elements of different proportions [6, 11]. Moreover, as it turns out, the factors that affect the results of the measurements are the presence and intensity of longitudinal reinforcement in the element [6, 7]. One of the methodological differences in the existing studies was the test stand. Some of the tests were performed on simply supported beams [6], while others on the elements resting on elastic sleepers or suspended on elastic ropes [8]. A different approach was placing the element in a press and applying the axial load with varying intensity [7] – it was found that the intensity of the load can also affect the measurement results.

Our own analyses reported in this paper are the continuation of the test tasks undertaken in the literature listed above. Their goal is to systematise the existing observations and formulate guidelines for the examination of Young's modulus of concrete using the eigenfrequency measurements.

2. Laboratory tests

2.1. Test elements

Tests were performed on two series of beam elements measuring 1050 mm × 200 mm × × 100 mm. Three elements were contained in each series. The series were made from different concrete mixtures – these concrete mixtures are summarised in Table 1.

In each of the series, six additional cylinders each with a nominal diameter of 113 mm and a height of 350 mm were created. Three of the cylinders were designed to determine the mean compressive strength f_{cm}, and the other three were designed to determine the mean static Young's modulus E_{cm} for both series (concrete mixtures). The concrete was compacted using a vibrating table. All of the elements were prepared in the laboratory. Fig. 1 shows the

steel moulds with the concrete mixture immediately after vibrating. Beams and cylinders were stored for 28 days in standardised curing conditions. After 28 days, all of the elements were stored under the same conditions.

Table 1

Concrete mixtures

Ingredient	B1 series	B2 series
Cement 42.5 R [kg/m^3]	300	350
Sand 02 [kg/m^3]	639	639
Aggregate 28 [kg/m^3]	639	639
Aggregate 816 [kg/m^3]	639	639
Water [kg/m^3]	143	143
W/C [–]	0.48	0.41
Plasticizer [kg/m^3]	–	3.15

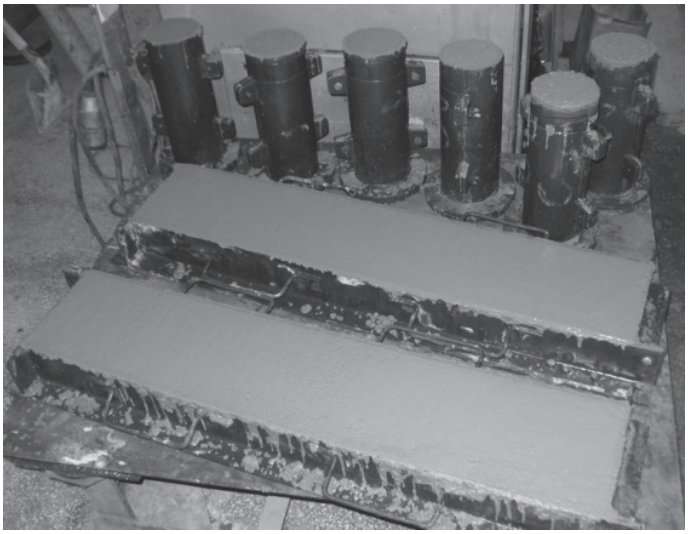

Fig. 1. Execution of test elements

2.2. Strength and deformability properties

Strength and deformability properties were determined on cylinders on the eve of testing the beams. On the three cylinders, the mean compressive strength f_{cm} for both concrete mixtures was determined. The other cylinders (three in each series) were used to determine the mean static Young's modulus E_{cm}.

Young's modulus was determined according to the internal procedure worked out in the Accredited Laboratory of the Department of Civil Engineering of Wroclaw University of

Technology. The cylinders were loaded in the strength press in accordance with a program set out in Fig. 2. The initial cycles were aimed at stabilising the deformation. Young's modulus was determined as a secant during the last cycle in the range of $0.1f_{cm} - 0.3f_{cm}$. Compression strength values for the load program were taken on the basis of the previously examined cylinders.

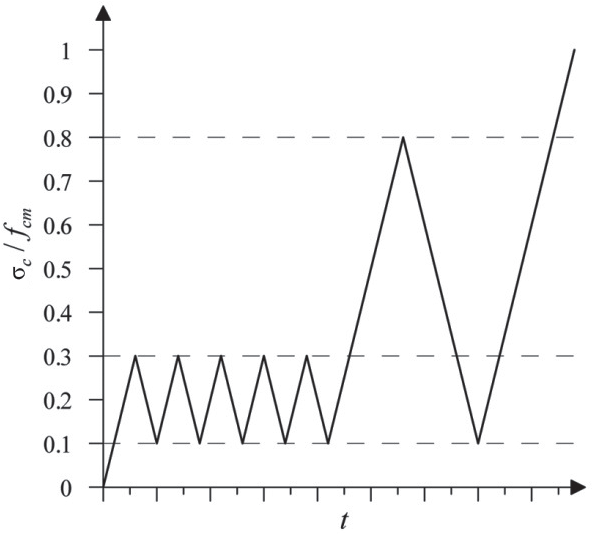

Fig. 2. The load program for determining the static Young's modulus

Fig. 3. Young's modulus testing

Deformation was measured using electrical resistance strain gauges with a 50 mm measuring base. On each specimen, three strain gauges were attached evenly and distributed around the circumference at half height. The specimen placed in the press is shown in Fig. 3. In Figures 4 and 5 are sample diagrams showing an example of deformation recorded for the specimens from the two measurement series.

The results of the compressive strength measurement and Young's modules are summarised in Table 2, the values were averaged for each series. For the mean compressive strength, six specimens were used – three specimens tested to determine the load program and three specimens destroyed after testing Young's modulus.

Measurements were performed using the B&K Pulse system. On each beam, 8 piezoelectric accelerometers were placed at a spacing of 150 mm – these recorded the response of the test element to random force generated by the environment.

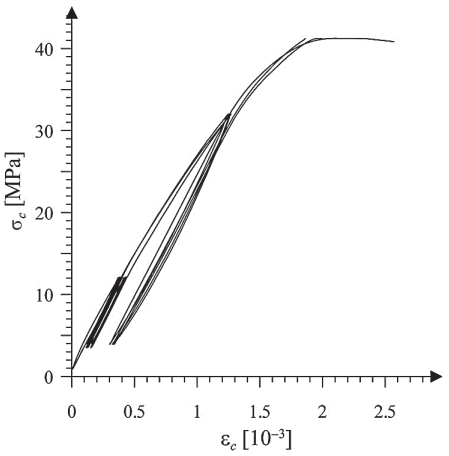

Fig. 4. Deformation for the B1 series specimen

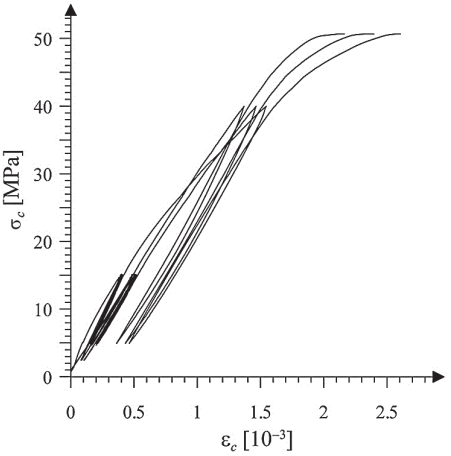

Fig. 5. Deformation for the B2 series specimen

Table 2

Concrete properties

Series	Mean compressive strength f_{cm} [MPa]	Mean Young's modulus E_{cm} [GPa]
B1	38.17	29.59
B2	50.05	32.50

The Operational Modal Analysis (OMA) [3] used in the experiment allowed the determination of the dynamic characteristics of the system (modal damping, frequency and eigenforms) without the need to record excitation as in the experimental modal analysis (EMA). The described method is also widely used in studies on real engineering structures in the natural scale [12].

2.3. The measurement of eigenfrequencies

Because of the simplicity of the implementation of the experiment, it was decided to conduct measurements on beams suspended on elastic ropes. The numerical model of the suspended beam is a simple bar without kinematic boundary conditions. This testing method provides a very accurate reflection of the theoretical model in laboratory conditions. The author's experience in this field [9] shows that the construction of another test bench (e.g. a simply supported beam) posed considerable difficulties. Effective setting of the appropriate boundary conditions in the laboratory model is problematic. At high eigenfrequencies and small vibration amplitudes during the measurements, locking the displacements at points of support is virtually impossible. The accuracy of the applied model is evidenced by the recorded eigenforms, where differences between the theoretical and measured values do not exceed 5%. Examples of the primary eigenforms recorded for the B1 series together with the theoretical forms are shown in Fig. 6.

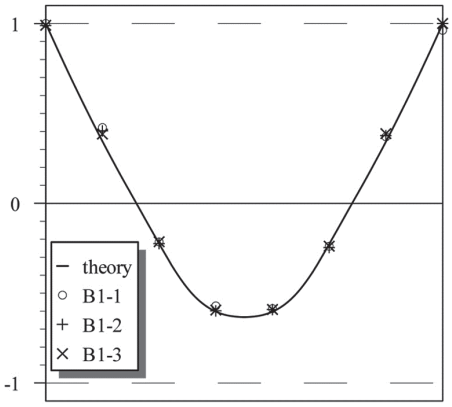

Fig. 6. B1 series primary eigenforms

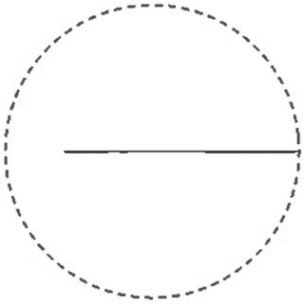

Fig. 7. Sample Nyquist's graph for the B1-1 beam

Nyquist's graphs are an additional confirmation of the good quality of the identification of the eigenforms. A sample graph is shown in Fig. 7. The circle shows the greatest amplitude, while the segments are the amplitudes of individual points (1 to 8) including the phases. If all the points oscillate in the consistent or opposite phase, the obtained segments are collinear. If there are inaccuracies, the sections 'scatter'.

Tests were conducted in 60-second cycles. Elements were tested in two positions. First, the elements were positioned so that they obtained a greater moment of inertia (Fig. 8). They were then rotated by 90° (Fig. 9). The measurement results are summarised in Table 3. The results were given for individual beams and the mean values were given for the B1 and B2 series.

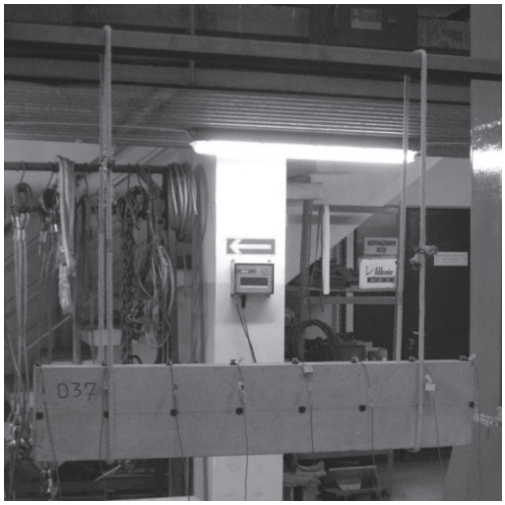

Fig. 8. B2-1 beam in position 1

Fig. 9. B2-1 beam in position 2

Table 3

The measured eigenfrequencies

Position of the beam	Eigenfrequency [Hz]							
	B1-1	B1-2	B1-3	**B1**	B2-1	B2-2	B2-3	**B2**
Vertical	671	687	669	**676**	672	690	680	**681**
Horizontal	365	373	370	**369**	372	372	364	**369**

When measuring the eigenfrequency of the beams in the vertical position, higher values were obtained for the B2 series. As expected, this is a consequence of the higher Young's modulus. On the other hand, this regularity was not found in case of testing the beams in the horizontal position. The obtained mean values of the eigenfrequencies, as tested in this position, are approximately equal to each other.

2.4. Dynamic Young's modulus

To determine the dynamic Young's modulus E_d, the relationship (1) taken from the elementary dynamics of the building was applied. In the illustrated form, this relationship allows us to calculate the frequencies of the bar with continuous weight distribution.

$$f_i = \gamma_i \cdot \sqrt{\frac{E_d \cdot I}{m \cdot l^4}} \tag{1}$$

where:

f_i – i^{th} natural frequency (in tests $i = 1$),
γ_i – coefficient for the i^{th} eigenform depending on the element's scheme,
I – moment of inertia of the cross-section,
m – rod's mass per unit length,
l – total length of the bar.

The coefficient γ_1 needs to be discussed – for the simple bar model, this is approx. 3.56. This value, however, applies to a one-dimensional element. Typically, a beam having a ratio of $l/h \geq 10$ is considered to be a one-dimensional element. Due to the proportions of the tested beams (in particular, in the vertical position, where $l/h = 5.25$) coefficients were calculated using the finite element method for three-dimensional volume structures. The values of the coefficients with corresponding eigenforms are shown in Fig. 10. The results of the calculations of the dynamic Young's modules are summarised in Table 4. For comparison, the values of the static Young's modulus for both concrete mixtures are given.

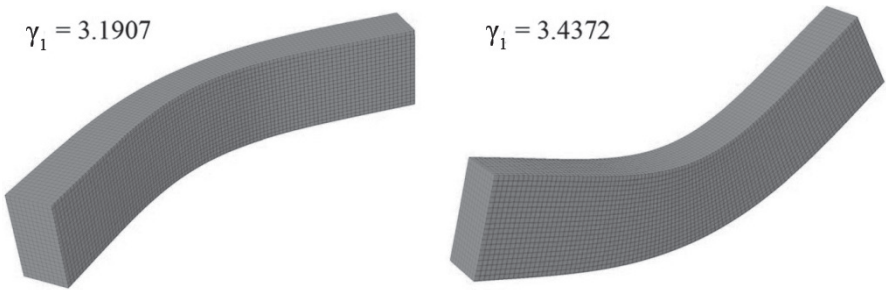

Fig. 10. Eigenforms and their corresponding coefficients

Table 4

Results of measurements and calculations

Beam/Series		B1-1	B1-2	B1-3	**B1**	B2-1	B2-2	B2-3	**B2**
E_{cm} [GPa]		29.59				32.50			
E_d [GPa]	Vertical position	35.62	37.33	35.50	**36.15**	35.10	37.67	37.71	**36.83**
	Horizontal position	36.15	37.87	37.37	**37.13**	37.20	37.31	36.63	**37.05**

2.5. Comparison of the results

Based on the tests, it was found that the dynamic Young's modulus was slightly higher in the case of the test performed in the horizontal position. The beam operated then in the direction of concrete casting. As mentioned above, these differences are insignificant and do not exceed 3%. This observation applies to both test series and is purely qualitative; its quantitative impact on the issues of structural engineering is, however, negligible.

It has been found that the higher static Young's modulus in the B2 series is not reflected in the dynamic Young's modulus. When tested in the vertical position for the B2 series, the value of the dynamic Young's modulus only increased by less than 2%. This difference, when tested in the horizontal position, was even lower – almost negligible.

The mean values of the dynamic Young's modules for both testing directions were 36.64 and 36.94 GPa, respectively, for the B1 and B2 series. On the basis of these values, the relationship E_d/E_{cm}, which is the most widely used indicator in the literature that allows the evaluation of the difference between the analysed values, was determined. It amounted to 1.24 and 1.14.

3. Conclusions

Based on the conducted tests, it can be concluded that the implemented test stand fully reflects the adopted theoretical model of the free bar. When conducting dynamic analyses, the recording of the eigenforms that allow its verification seems necessary.

In the dynamic testing, similar values of Young's modulus were obtained regardless of the direction of the vibration of the analysed sections. The applied method can be used for testing concrete homogeneity.

Despite various mixtures that allow the obtaining of concrete with different static Young's modules, the examined dynamic Young's modules were similar. It was found that in the case of the B1 series, the dynamic Young's modulus was 24% higher than the static modulus, and by 14% for the B2 series. On the basis of the tested elements, it can therefore be concluded that this difference depends on the concrete compressive strength and it decreases with the increase of the strength. This observation, however, should be confirmed in further studies for other concretes.

Higher values of the dynamic Young's modules are caused, for example, by the fact that the investigated beams are minimally stressed – only under their own weight. The static Young's modules were determined for the effort of 10–30%, after six load-unload cycles.

The sensitivity of the Young's modulus calculated according to the transformed equation (1) is extremely important to the accuracy of the frequency measurement. For example, if the eigenfrequency is measured with a 10% error, the Young's modulus will be encumbered with an error of approx. 20%. In the case of the inverse analysis, this problem is not so important, because a 10% error in the case of the Young's modulus translates into only a 5% error of the calculated frequency – this should be kept in mind when planning tests with the use of the described technology.

The author wishes to thank Mr. Jacek Grosel, PhD of the Faculty of Civil Engineering of Wroclaw University of Technology for his assistance in carrying out laboratory tests and his extremely valuable guidance.

References

[1] ASTM C215 – 14, Standard Test Method for Fundamental, Longitudinal, and Torsional Resonant Frequencies of concrete Specimens, ASTM Standard.

[2] ASTM C469/C469M – 14, Standard Test Method for Static Modulus of Elasticity and Poisson's Ratio of Concrete in Compression, ASTM Standard.

[3] Batel M., *Operational Modal Analysis – Another Way of Doing Modal Testing*, Sound and Vibration, August, 2002, 22–27.

[4] EN 12390-13:2014, Testing Hardened Concrete – Part 13: Determination of Secant Modulus of Elasticity in Compression.

[5] Hoła J., Schabowicz K., *State-of-the-art non-destructive methods for diagnostic testing of building structures – anticipated development trends*, Archives of Civil and Mechanical Engineering, Vol. 10(3), 2010, 5–18.

[6] Jerath S., Shibani M.M., *Dynamic Modulus for Reinforced Concrete Beams*, Journal of Structural Engineering, Vol. 110(6), 1984, 1405–1410.

[7] Malaikah A., Al-Saif K., Al-Zaid R., *Prediction of the Dynamic Modulus of Elasticity of Concrete Under Different Loading Conditions*, International Conference On Concrete Engineering and Technology, Kuala Lumpur, 19–21 April 2004, 32–39.

[8] Musiał M., *Static and dynamic stiffness of reinforced concrete beams*, Archives of Civil and Mechanical Engineering, Vol. 12(2), 2012, 186–191.

[9] Musiał M., Grosel J., *Identyfikacja schematu stanowiska badawczego z wykorzystaniem operacyjnej analizy modalnej*, Materiały Budowlane, 3, 2013, 42–44.

[10] Newtson C.M., Johnson G.P., Enomoto B.T., *Fundamental Frequency Testing of Reinforced Concrete Beams*, Journal of Performance of Constructed Facilities, Vol. 20(2), 2006, 196–200.

[11] Plachy T., Padevet P., Polak M., *Comparison of Two Experimental Techniques for Determination of Young's Modulus of Concrete Specimens*, Recent Advances in Applied and Theoretical Mechanics, Puerto De La Cruz, 14–16 December 2009, 68–71.

[12] Wójcicki Z., Grosel J., Sawicki W., *Eksperymentalne badania dynamiczne budowli*, DWE, Wrocław 2015.

TECHNICAL TRANSACTIONS | CZASOPISMO TECHNICZNE
CIVIL ENGINEERING | BUDOWNICTWO
3-B/2015

WOJCIECH POLITALSKI*

NUMERICAL ANALYSIS OF THREE-SPAN SLAB POST-TENSIONED WITH UNBONDED TENDONS AT ULTIMATE

ANALIZA NUMERYCZNA TRÓJPRZĘSŁOWEJ PŁYTY SPRĘŻONEJ CIĘGNAMI BEZ PRZYCZEPNOŚCI W STANIE GRANICZNYM NOŚNOŚCI

Abstract

The design of multi-span structures post-tensioned with unbonded tendons may differ from the assigned one for reinforced structures or structures post-tensioned with bonded tendons. In some cases Ultimate Limit State can be reached by different loading patterns to which we got used to i.e. load cases which result in maximum values of bending moments in spans and at supports. This behaviour is related to the lack of bond between concrete and strands and the assumption that the force in tendons has a uniform value between anchorages.

Keywords: *design process, stress increase in unbonded tendons, multi-span members*

Streszczenie

Projektowanie konstrukcji wieloprzęsłowych sprężonych cięgnami bez przyczepności może się różnić od tego, które jest wykorzystywane w konstrukcjach żelbetowych bądź sprężonych cięgnami z przyczepnością. W niektórych przypadkach Stan Graniczny Nośności może zostać osiągnięty przez inne schematy obciążenia do których jesteśmy przyzwyczajeni, tj. przypadki obciążeń, w których otrzymujemy maksymalne wartości momentów zginających w przęsłach i nad podporami. To zjawisko jest związane z brakiem przyczepności pomiędzy betonem i zbrojeniem sprężającym oraz założeniem, że siła w cięgnie przyjmuje jednorodną wartość pomiędzy zakotwieniami.

Słowa kluczowe: *projektowanie, przyrost naprężeń w cięgnach, elementy wieloprzęsłowe*

DOI: 10.4467/2353737XCT.15.169.4344

* Ph.D. Eng. Wojciech Politalski, Institute of Building Materials and Structures, Faculty of Civil Engineering, Cracow University of Technology.

1. Introduction

Codes recommendations [1–3] treat unbonded tendons stress increase in continuous members in a superficial way. The ACI Code design equations for calculating stress increase do not make distinctions between simply supported and continuous members. The opportunity to achieve lower values of stress increase in multi-span members compared to simply supported elements in the case of loading which does not act at all spans simultaneously is disregarded by EC 2. Even though such a possibility is mentioned in Polish Code no detailed provisions are given.

Due to the abovementioned situation, strategies for solving the problem of stress increment in multi-span unbonded members are sought and can be successfully found in theories proposed by various authors [4–7]. The proposed equations assigned for continuous members account for expansions of equations derived firstly for simply supported members. Hence the fact that the loading pattern factor for simply supported beams is equal to 1.

Numerous items of data relating to the testing of simply supported members can be found in literature. Due to the fact that the conducting research on multi-span structures is much more complicated, only a few examples can be found in publications. Numerical analysis based on tests conducted by Burns et al. [8] was carried out. The received results were compared with analytical calculations obtained using various theories regarding the loading pattern factor which were derived by Naaman and Harajli [4–7].

2. Experimental test by Burns et al.

Elements Slab A and Slab B tested by Burns et al. [8] were three-span slabs. The length of each span was the same and was equal to 6.1 m. The cross-section height was 140 mm. In fact members were half-scale models. In order to obtain proper scaling for self-weight, live-loading and prestress, the span length, cross-section height and effective depth were reduced to 50% and the cross-section width and self-weight were increased up to 200%. Slab A and Slab B differ in their ordinary and prestressing reinforcement ratios. They were designed in such a way that the sum q_0 of the ordinary reinforcement index q_s and the prestressing reinforcement index q_e for each member was the same. The indices are defined as follows: $q_s = (\rho_s \cdot f_y)/f_c'$ and $q_e = (\rho_p \cdot f_{pe})/f_c'$. Geometric and materials' characteristics are presented in Table 1. View and cross-sections are shown in Fig. 1. The lengths of reinforcing bars in spans and at supports are not given – the only information provided for this is that they were too short. The main crack which determined the location of the crucial cross-section at ultimate was localised near to the end of ordinary reinforcement.

Utilised loading patterns are gathered in Table 2. Combinations 108–110 and 208–210 led to the slabs' failure. It can be observed that in almost all of over mentioned combinations, except full loading in one or two spans there is acting percentage of loading in other spans.

Table 1

Geometry and materials' characteristics of half-scale members tested by Burns et al.

Members' name	Span lenght leff	Cross-section's dimensions [mm]				Concrete	Prestressing reinforcement					Ordinary reinforcement				Steel
						f_c	wires	A_p	q_e	f_{py}	f_{pu}	bars	A_{s1}	f_y	q_s	q_0
	[m]	h	dp	ds	b	[MPa]	[n × Ø]	[mm²]	[–]	[MPa]	[MPa]	[n × Ø]	[mm²]	[MPa]	[–]	[–]
Slab A	3 × 3.05	70	57	57	1397	32.4	4 × ϕ6.3	127	0.048	1469	1655	4 #2	127	448	0.022	0.070
Slab B						35.5	3 × ϕ6.3	95	0.034			7 #2	222		0.035	0.069

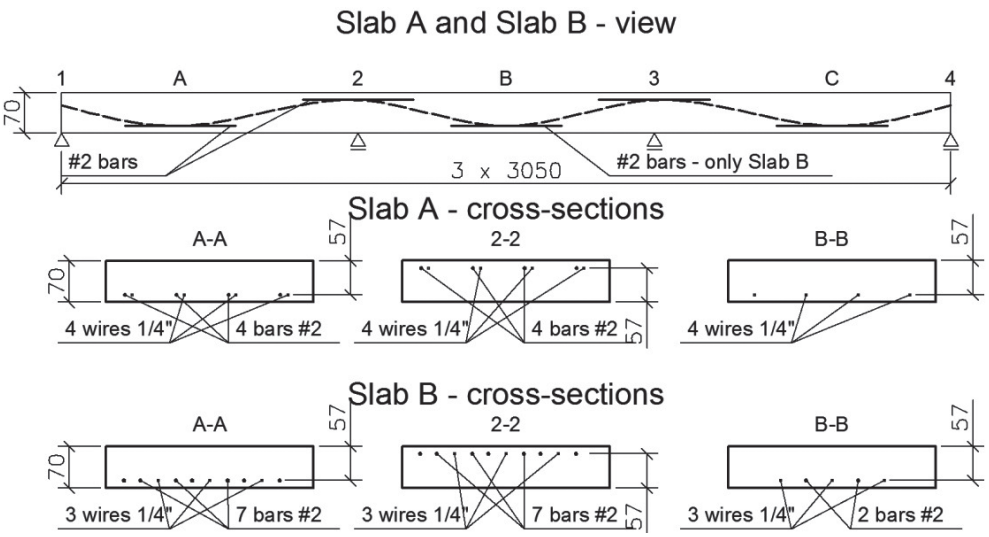

Fig. 1. View and cross-sections of members tested by Burns et al.

Table 2

Loading patterns of three-span members tested by Burns et al.

Loading pattern	Slab A – loading [kN/m²]			Loading pattern	Slab B – loading [kN/m²]		
	span A	span B	span C		span A	span B	span C
101	2.4	2.4	2.4	201	1.7	1.7	1.7
102	2.4	0.0	2.4	202	2.4	2.4	2.4
103	0.0	2.4	2.4	203	2.4	2.4	0.0
104	5.0	2.4	5.0	204	4.8	0.0	4.8
105	4.9	4.9	2.4	205	4.8	4.8	4.8
106	5.0	0.0	5.0	206	5.5	5.5	5.5
107	5.5	5.5	5.5	207	5.5	5.5	1.3
108	6.5	1.3	6.5	208	5.7	1.3	5.7
109	7.4	7.4	1.3	209	1.3	6.9	6.9
110	0.0	7.2	0.0	210	1.3	7.6	1.3

3. Numerical analysis – assumptions

Numerical analysis was conducted using FEM DIANA [9]. A total Strain Fixed crack model for concrete was used. The tensile stress-strain relationship is described by brittle cracking behaviour (Fig. 2a), the compressive stress-strain relationship is described by a multilinear diagram (Fig. 2b).

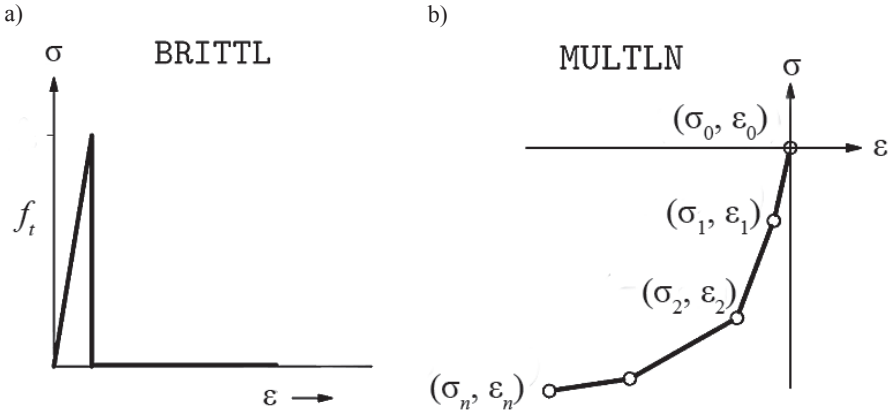

Fig. 2. Total Strain Fixed crack model for concrete a) in tension b) in compression

Initially, the target of the numerical analysis was a comparison of its results with the findings of experimental tests conducted by Burns et al. This intention was relinquished due to the following reasons:

- a limited amount of data relating to materials' properties and a lack of information regarding the Young modulus and tensile strength of concrete,
- preliminary failure of structure connected with lengths of reinforcing bars at supports that were too short,
- member failure was caused by not "basic" load patterns i.e. combination where except maximum loadings in spans partial loading in other spans was also acting.

Due to these facts the following assumptions were made:

- the concrete Young modulus of elasticity was calculated according to equation (1):

$$E_{ci} = 4700 \cdot \sqrt{f_c'} \tag{1}$$

- the brittle cracking models of concrete in tension shown in Fig. 3a were used,
- Hognestadt compressive behaviour of concrete calculated in accordance with equation (2), with values given in Table 3 as shown in figure 3b were used:

$$\sigma = f_c' \cdot \left[2\frac{\varepsilon}{\varepsilon_0} - \left(\frac{\varepsilon}{\varepsilon_0} \right)^2 \right] \quad 0 \le \varepsilon \le \varepsilon_0; \quad \sigma = f_c' \cdot \left[1 - 0.15 \cdot \left(\frac{\varepsilon - \varepsilon_0}{\varepsilon_{cu} - \varepsilon_0} \right) \right] \quad \varepsilon_0 \le \varepsilon \le \varepsilon_{cu} \tag{2}$$

Table 3

Stress-strain relationship for concrete in compression

	Multilinear diagram values of σ(ε) relationship for concrete in compression – Slab A												
Strain [‰]	0	0.24	0.48	0.73	0.97	1.21	1.45	1.70	1.94	2.18	2.42	3.00	3.01
Stress [MPa]	0	6.2	11.7	16.5	20.7	24.3	27.2	29.5	31.1	32.1	32.4	27.5	0.1
	Multilinear diagram values of σ(ε) relationship for concrete in compression – Slab B												
Strain [‰]	0	0.25	0.51	0.76	1.01	1.27	1.52	1.77	2.03	2.28	2.54	3.00	3.01
Stress [MPa]	0	6.7	12.8	18.1	22.7	26.6	29.8	32.3	34.1	35.1	35.5	30.2	0.1

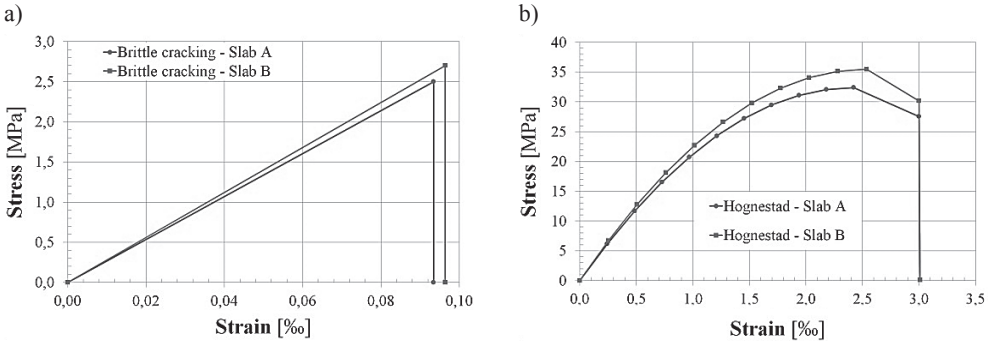

Fig. 3. Assumed models for concrete a) in tension b) in compression

– 'embedded reinforcement' was used for reinforcement modeling. With a bond for ordinary reinforcement and without a bond for prestressing reinforcement,
– the strain-stress relationship for ordinary reinforcement was taken after EPSH model presented in report [10] dealing with determining of yield strength. This curve (Fig. 4a) consists of three parts: linear elastic, ideal plastic and material hardening described by parabola eq. (3):

$$f_s = f_u - (f_u - f_y) \cdot \left(\frac{\varepsilon_{su} - \varepsilon}{\varepsilon_{su} - \varepsilon_{sh}} \right) \tag{3}$$

– a bilinear stress-strain relationship (linear elastic and material hardening) was used for prestressing reinforcement (Fig. 4b). Assumed 0.1% proof-stress of prestressing steel (yield strength value) equal to 1742 MPa,
– new loading patterns were introduced:
  ○ 100 and 200 for single-span slabs (A and B respectively) which serve as a comparative members,
  ○ 111–115 and 211–215 for three-span slab (A and B respectively) which are basic combinations for three-span slab i.e. maximum uniformly distributed loadings act simultaneously in single, both or all spans (Table 5). No partial loading in other spans is allowed.

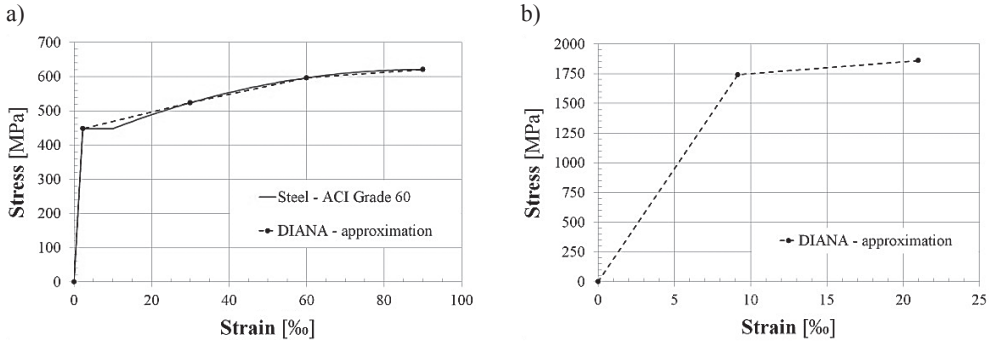

Fig. 4. Assumed models for: a) ordinary reinforcement, b) prestressing wires

Table 4

Concrete, reinforcement and wires characteristics in numerical analysis

	Concrete					Ordinary reinforcement				Prestressing reinforcement			
	f_c' [MPa]	E_{ci} [GPa]	ε_0 [‰]	ε_{cu} [‰]	f_{ct} [MPa]	n × ϕ	A_s [mm²]	f_y [MPa]	f_u [MPa]	n × ϕ	A_p [mm²]	$f_{p0.1k}$ [MPa]	f_{pu} [MPa]
Slab A	32.4	26.8	2.42	3.0	2.5	4 #2	127	448	621	4 × 1/4”	127	1742	1860
Slab B	35.5	28.0	2.54	3.0	2.7	7 #2	222			3 × 1/1”	95		

Table 5

Definition of loading patterns used in numerical analysis

	Loading pattern – Slab A						Loading pattern – Slab B					
Span loading according to Fig. 1	100	111	112	113	114	115	200	211	212	213	214	215
	–	A	B	A & B	A & C	A, B & C	–	A	B	A & B	A & C	A, B & C

Quadrilateral, 8 nodes plane stress elements were used for meshing (Fig. 5). For each slab 3 different geometrical models were created as shown in Fig. 6:

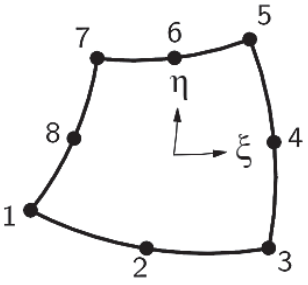

Fig. 5. CQ16M element

- single-span model treated as a comparative member (load patterns 100 and 200),
- three-span model (load patterns 111–114 and 211–215),
- one and semi-span model (left external span and half of internal span – load patterns 115 and 215). This model was created due to problems with achieving convergence for a three-span model in high levels of loading. This was caused by forming 4 plastic hinges – 2 at internal supports and 2 in external spans.

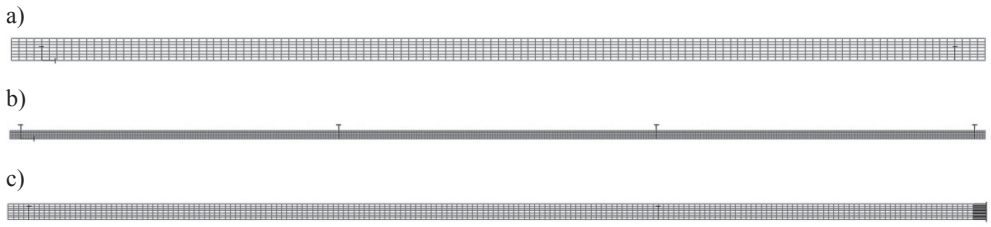

Fig. 6. Meshing for: a) single-span, b) three-span, c) one and semi-span model

4. Numerical analysis – results

Because the majority of considerations about stress increment in unbonded tendons is connected with plastic hinge length, stress values in ordinary reinforcement (bottom A_{s1} and top A_{s2}) are shown in Figures 7–18. Discontinuities visible in these diagrams are connected with a crack pattern. Stresses in reinforcement are greater in cross-sections where cracking occurs and are smaller in those where cracking is not present. Stress values are given in [MPa] and the length of slab (measured from left external support) in [mm].

The most important results from numerical analysis are displayed in Table 6. These are as follows:

- effective prestress f_{pe},
- value of uniformly distributed loading, corresponding stresses f_{ps} and stress increase Δf_{ps} in unbonded tendons at plasticize of top and bottom reinforcement and at failure,
- maximum values of stresses in the bottom and the top reinforcements (σ_{s1} and σ_{s2}) and maximum compressive strains in concrete at failure ε_c.

Observation of the above charts (Fig. 7–18) and results presented in Table 6 leads to the following conclusions regarding failure mechanism in researched members:

- plastifying of ordinary reinforcement appears earlier in Slab A (combination 100) than in Slab B (combination 200). Such behavior is connected with an ordinary reinforcement ratio which is larger in the second member. Due to the correct crack pattern, the stress increase in unbonded tendons can reach yield strength in both slabs. As a result of the greater value of prestressing reinforcement in first member, it is able to resist larger external loading at failure than the second one,
- the loading of only one external span (combinations 111 and 211) leads to simultaneously plastifying of ordinary reinforcement in the loaded span and internal support. Due to the same reasons as above plastifying of ordinary steel occurs earlier in Slab A than Slab B. Load increase results in failure of the member at internal support caused by the crushing of concrete. Behaviour which is different to that which is described above can be observed. Larger value of ordinary reinforcement ratio in the second member has positive influence on plastic hinge formation both at internal support and external reinforcement. It should be highlighted that in both cases, the stress increment in unbonded tendons is lower than the yield strength of ordinary reinforcement and is greater for Slab B. These two facts decide that this member could resist greater external loading,

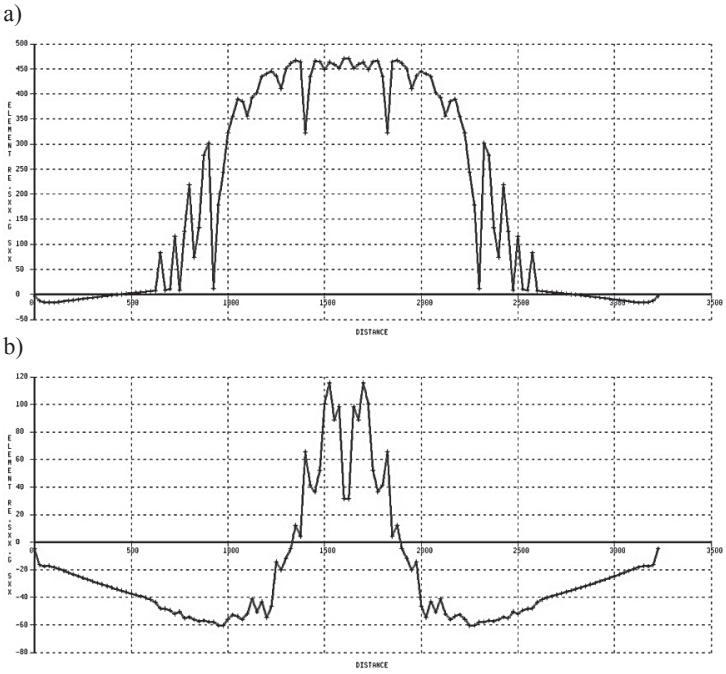

Fig. 7. Stresses in ordinary reinforcement in single-span model (100): a) bottom, b) top

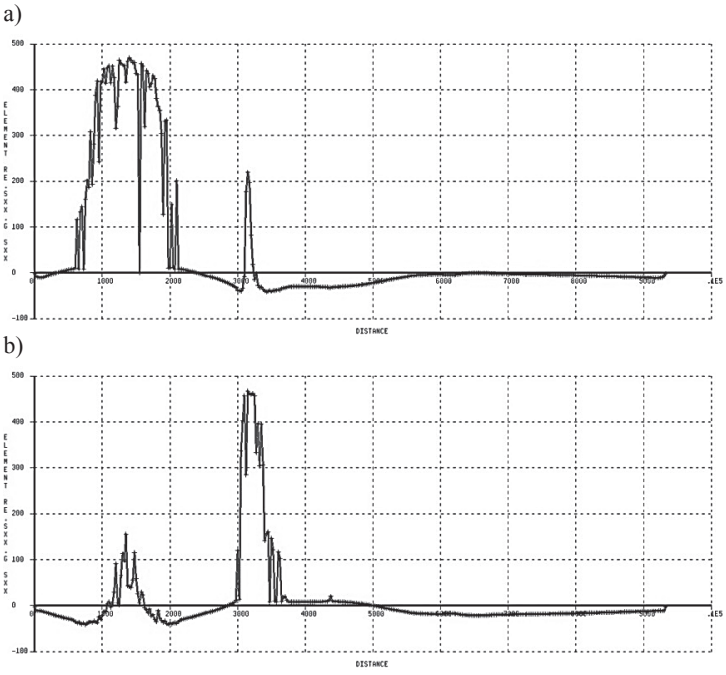

Fig. 8. Stresses in ordinary reinforcement in three-span model (111): a) bottom, b) top

a)

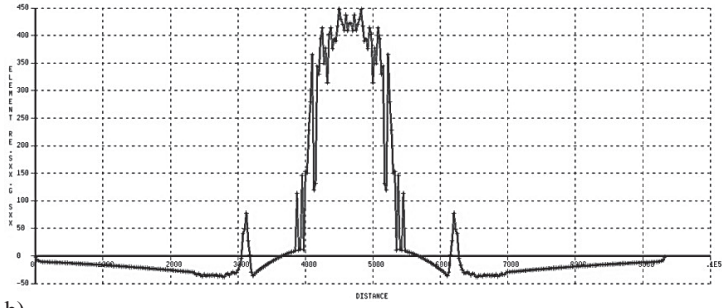

b)

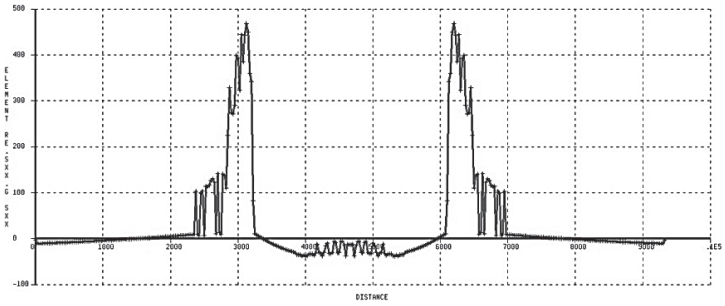

Fig. 9. Stresses in ordinary reinforcement in three-span model (112): a) bottom, b) top

a)

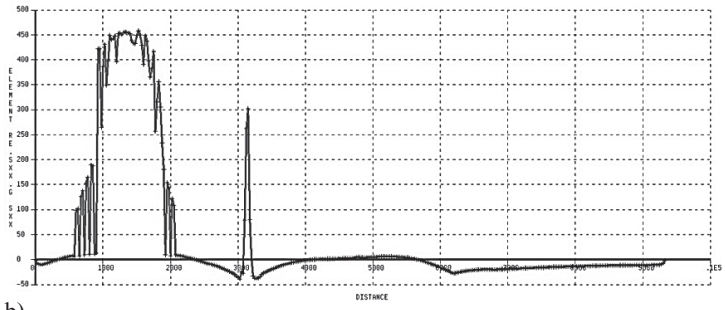

b)

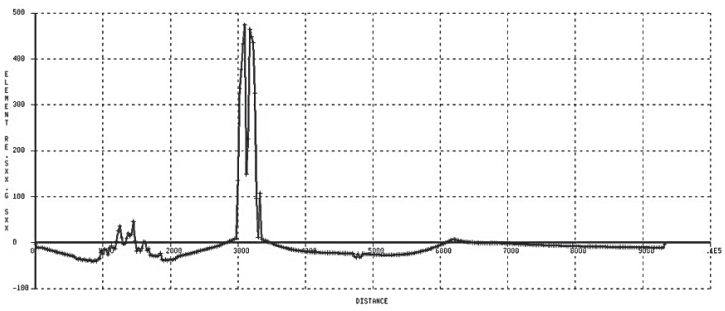

Fig. 10. Stresses in ordinary reinforcement in three-span model (113): a) bottom, b) top

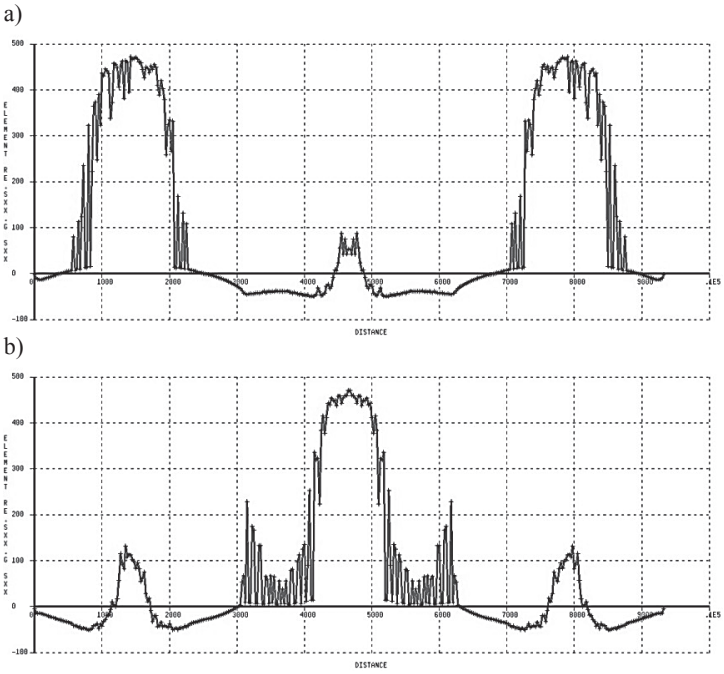

Fig. 11. Stresses in ordinary reinforcement in three-span model (114): a) bottom, b) top

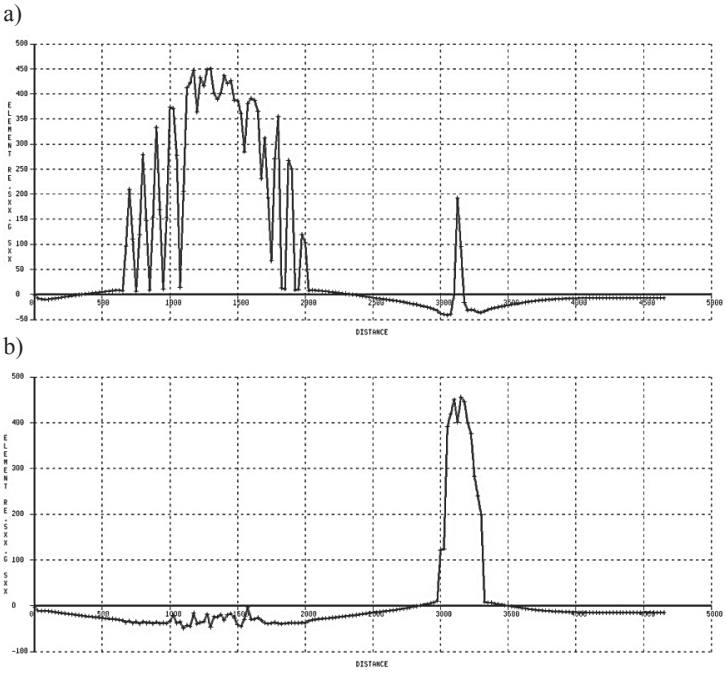

Fig. 12. Stresses in ordinary reinforcement in one and semi-span model (115): a) bottom, b) top

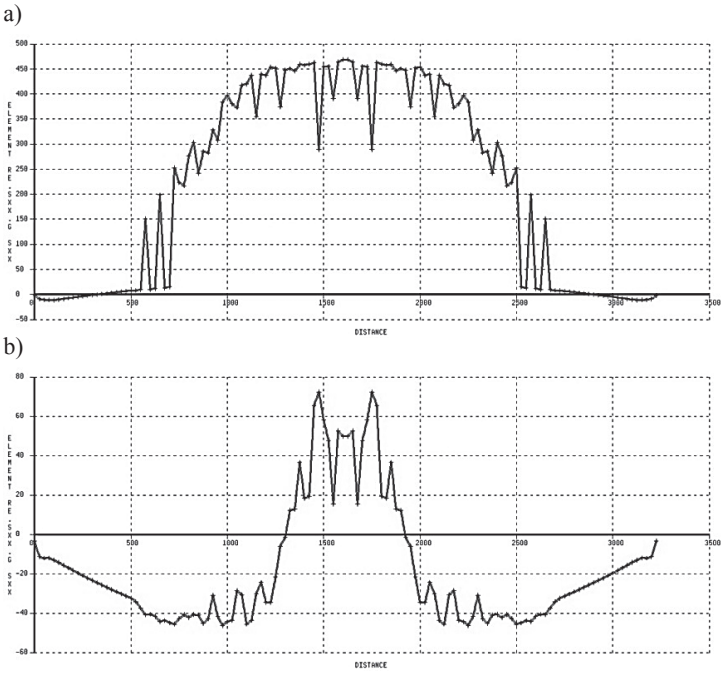

Fig. 13. Stresses in ordinary reinforcement in single-span model (200): a) bottom, b) top

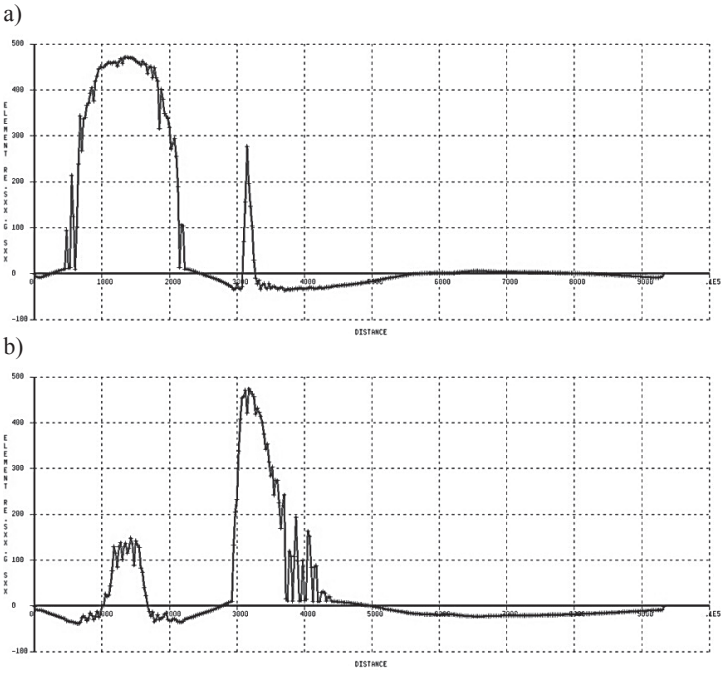

Fig. 14. Stresses in ordinary reinforcement in three-span model (211): a) bottom, b) top

a)

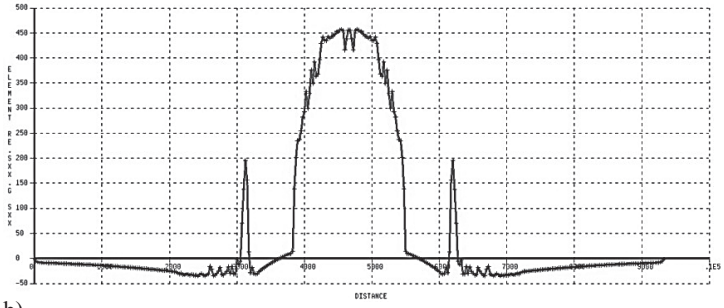

b)

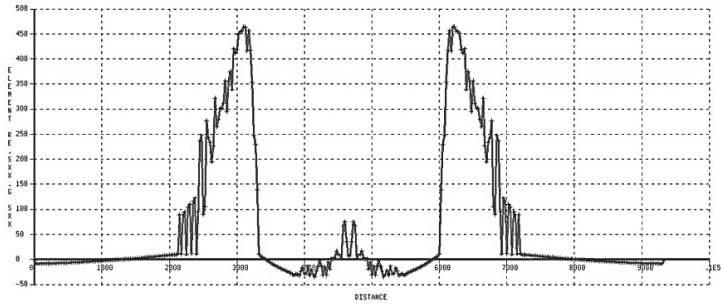

Fig. 15. Stresses in ordinary reinforcement in three-span model (212): a) bottom, b) top

a)

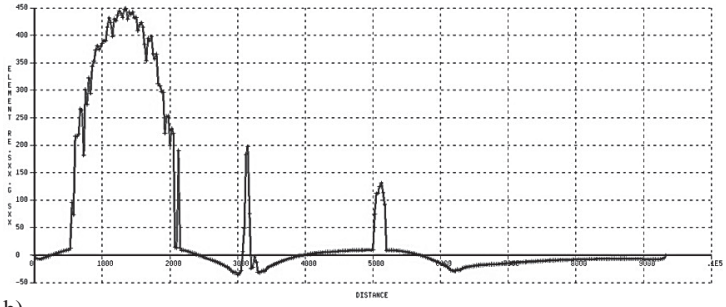

b)

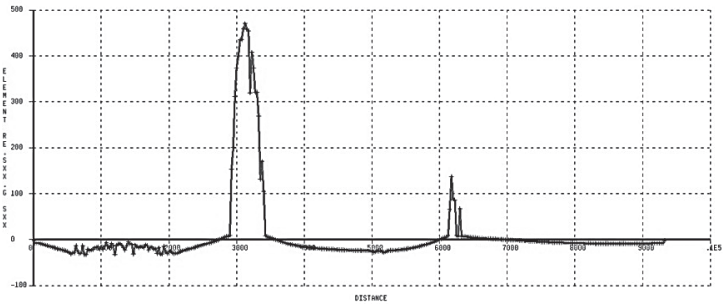

Fig. 16. Stresses in ordinary reinforcement in three-span model (213): a) bottom, b) top

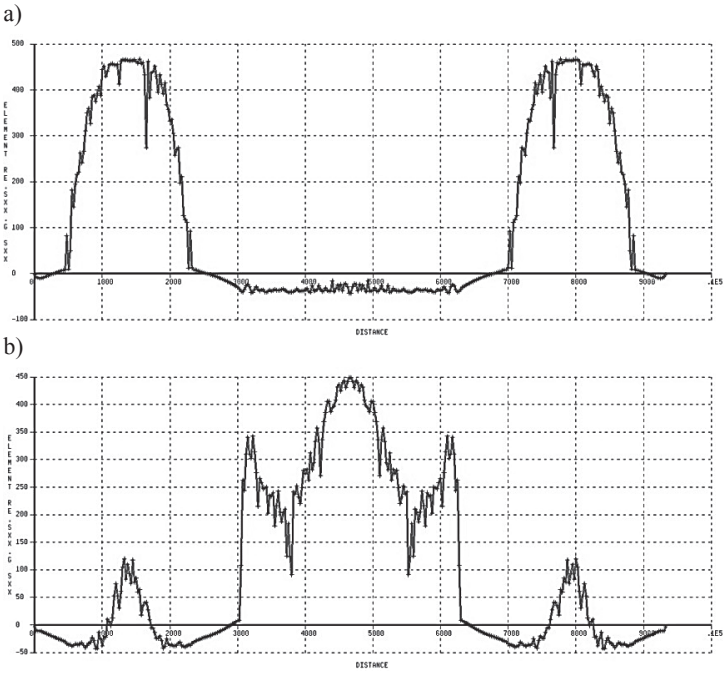

Fig. 17. Stresses in ordinary reinforcement in three-span model (214): a) bottom, b) top

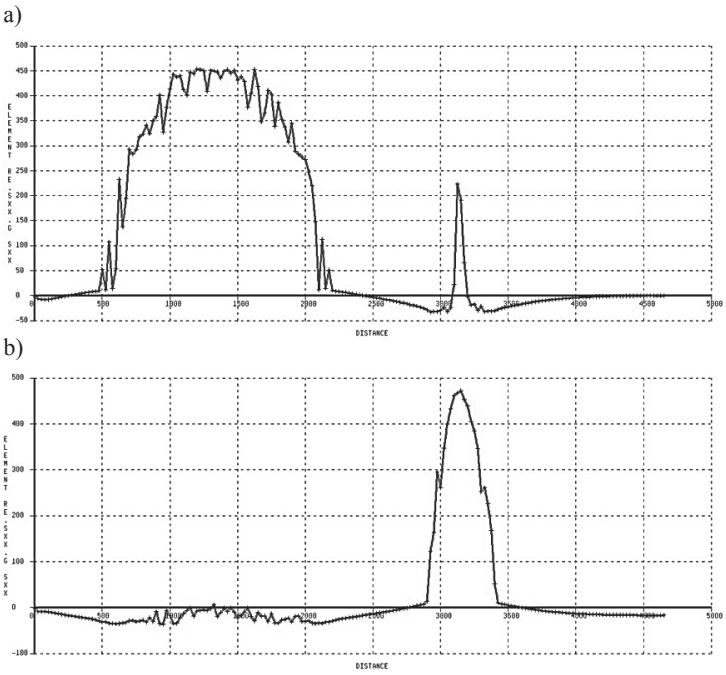

Fig. 18. Stresses in ordinary reinforcement in one and semi-span model (215): a) bottom, b) top

Table 6

Numerical analysis results for different loading patterns

		Loading pattern – Slab A						Loading pattern – Slab B					
		100	111	112	113	114	115	200	211	212	213	214	215
f_{pe} [MPa]		968	968	968	968	968	968	1006	1006	1006	1006	1006	1006
Plasticize $A_{s(top)}$ [kN/m]		–	7.7	11.6	6.6	8.9	6.9	–	8.6	13.5	6.8	11.7	7.9
f_{ps} [MPa]		–	1032	1025	998	1212	1031	–	1092	1105	1054	1549	1117
Δf_{ps} [MPa]		–	64	57	30	244	63	–	86	99	48	543	111
Plasticize $A_{s(bottom)}$ [kN/m]		4.3	7.7	13.2	7.6	7.7	8.4	5.2	8.6	14.3	9.0	8.4	9.6
f_{ps} [MPa]		1160	1032	1071	1031	1110	1102	1285	1092	1123	1104	1186	1202
Δf_{ps} [MPa]		192	64	103	63	142	134	279	86	117	98	180	196
Failure [kN/m]		8.4	9.3	13.2	8.8	10.9	8.4	7.7	11.3	16.0	9.1	11.7	10.4
f_{ps} [MPa]		1742	1139	1071	1080	1477	1102	1731	1310	1209	1107	1549	1252
Δf_{ps} [MPa]		774	171	103	112	509	134	725	304	203	101	543	246
Support 2 or Span B	σ_{s1} [MPa]	–	467	468	474	471	456	–	474	464	470	449	472
	σ_{s2} [MPa]	–	219	78	300	87	192	–	276	195	200	–16	225
	ε_c [‰]	–	–3.07	–1.52	–4.17	–1.77	–2.88	–	–3.64	–2.95	–2.97	–0.98	–3.68
Span	σ_{s1} [MPa]	471	470	448	458	472	451	469	471	457	449	467	453
	σ_{s2} [MPa]	116	155	–39	45	132	–3	72	148	75	–33	120	6
	ε_c [‰]	–2.32	–1.68	–0.95	–1.24	–2.07	–1.86	–2.01	–2.25	–1.60	–0.89	–1.99	–1.16

– for loading combinations where the internal span was loaded (112, 113, 115, 212, 213 and 215) plastifying of ordinary reinforcement appears earlier at supports than in spans. Due to the same reasons as above plastifying of ordinary steel occurs earlier in Slab A than Slab B. Similar behaviour as described above can be observed for combinations 111 and 211 – greater stress increment in unbonded tendons and accompanying resistance. This phenomenon is different in combinations where only the internal span is loaded (113 and 213). A slightly greater stress increment was achieved in Slab A, but it has no influence on the bending resistance of these two members. It should be underlined that only in loading combination 112 value of compressive strains at internal support was far from ultimate strain for concrete (3‰). In other cases, a further increase of loading will lead not only to exceeding the limit value of strains in tensile reinforcement A_{s1} (10‰) but also will cause crushing of the concrete,

– simultaneously loading of external spans (combinations 114 and 214) leads to earlier plastifying in spans. Instead of forming two plastic hinges at internal supports plastifying of top reinforcement in internal span could be observed. Such behaviour is caused by a lack of loading in this span and an additional action which comes from prestress. Similarly like previously greater value of ordinary reinforcement ratio leads to achieving larger values of stress increase in unbonded tendons. Also, bending resistance of Slab B is greater. Concrete strains at ultimate at support cross-section are very close to 2‰.

The stress increment value is related to the effort of spans' cross-sections (where long plastic hinges are formed) and effort of supports' cross-sections (where short plastic hinges are formed). If plastifying of ordinary reinforcement appears earlier in spans greater value of stress increment in unbonded tendons should be expected. The following conclusion can be drawn from results comparison of combinations where only external span is loaded (111 and 211) and other combinations where additional loading is acting in internal span (113, 213, 115 and 215). It has negative influence on stress increment in unbonded tendons because it leads to faster member failure at support and limits possibility of forming long plastic hinge in spans. Comparison of loading single external span (111 and 211) and internal span (112 and 212) enables to observe influence of which span is loaded. First loading pattern makes possible to form long plastic hinge in span which leads to greater stress increment in unbonded tendons. Greatest values of stress increment in unbonded tendons were achieved on case of simultaneously loading of external spans (114 and 214). It is worth to emphasize that they were not so big as for single-span members (100 and 200). Stress increase in unbonded tendons is not only influenced by pattern loading but also by ordinary reinforcement ratio which enables proper formation of plastic hinges (especially at support cross-sections). Its influence could be observed also in above numerical analysis. Of course it could be questionable due to different concrete properties used for Slab A and Slab B. Without doubt it should be claimed that 10% difference in compressive strength will not cause almost two times higher stress increase in unbonded tendons in some cases.

5. Loading pattern as a parameter

The consideration of the loading pattern as a parameter was taken by a few researchers. Naaman [4] presents this in a very simple way as the ratio of loaded spans to total spans length (distance between anchorages). In one of his first papers [5] Harajli proposes to express it in a very similar way as the ratio of the number of loaded spans to the total number of spans. Assuming equal length of all spans leads to the same value of loading patterns expressed by the equation below (4). For simply supported member value of this parameter is equal to 1.

$$\frac{L_1}{L_2} = \frac{n_o}{n} \tag{4}$$

In a subsequent paper [6], Harajli connected the value of this parameter with the number and length of plastic hinges formed at ultimate eq. (5). Plastic hinge length L_0 is influenced by the type of acting loading (uniformly distributed loading, one-point or two-point loading) and the manner of determining number of plastic hinges is presented in Fig. 19.

$$\frac{n_p}{n} \tag{5}$$

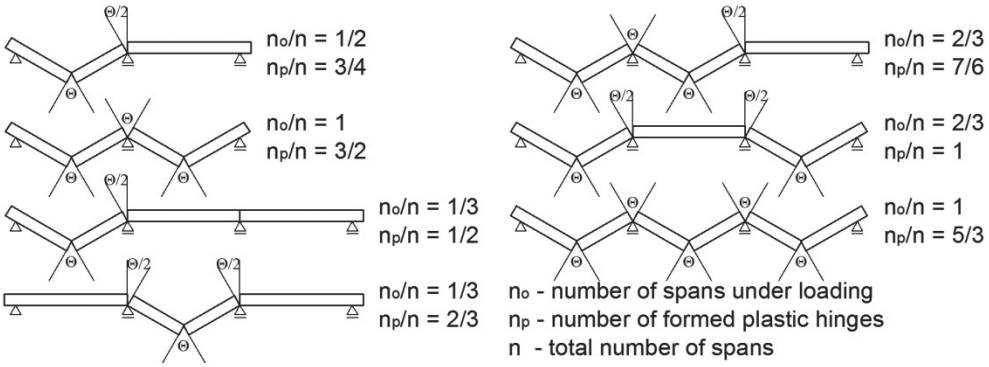

Fig. 19. Load pattern factor values – two- and three-span members

Some discrepancies could be found in abovementioned theory. Factor f which depends on the loading type, expresses only one plastic hinge length. It should be added that plastic hinge length differs in span where different types of loading could be acting ($f = 3$, 6 or ∞) and at support where reaction should be rather associated with one-point loading ($f = \infty$).

The next paper [7] deals with these doubts by introducing the distinction between plastic hinges formed in spans n_p^+ and at supports n_p^-. Both of these are connected and expressed by N_p factor. The method of calculating the N_p factor is presented in Figure 20. The number of plastic hinges in spans n_p^+ and at supports n_p^- are presented. Moreover two values of this factor which depend on type of loading are presented for one-point loading (1P) and uniformly distributed loading (q) respectively. It is worth emphasising that this value for simply supported beams equals 10.5 and 14 accordingly.

The load pattern parameter is expressed in equation (6) as a ratio of N_p value divided by total member length L to $N_{p(1span)}$ value calculated for single-span member divided by length $L_{(1span)}$ of span.

$$\frac{N_p / L}{N_{p(1span)} / L_{(1span)}} \tag{6}$$

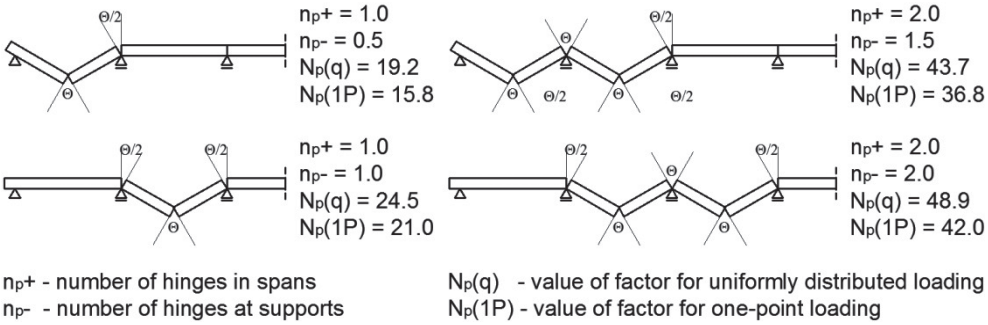

Fig. 20. Load pattern factor calculation with span and support hinge distinction taken into account

The following conclusions can be drawn from this short overview of the load pattern parameter and its influence on the stress increase in unbonded tendons:

– the first approach (eq. 4) treats this problem in a simplified way. The failure mechanism which has an influence on stress increment in unbonded tendons is not taken into consideration. It makes no significance whether or not external or internal span is loaded. The loading of all spans simultaneously should lead to the same value of stress increase in unbonded tendons as in simply supported members,
– the second approach (eq. 5) takes the failure mechanism into consideration and the stress increment in unbonded tendons is dependent on the number and length of plastic hinges. Their lengths are connected with the type of acting loading. However, the fact that plastic hinge lengths are smaller at supports is not taken into account. Support reactions should be treated in a similar way as point loading. In case of all or almost all spans loaded load pattern value could be greater than 1. This indicates that stress increase in unbonded tendons could be greater than in comparative simply supported members,
– the third approach (eq. 6) introduces an amendment considering plastic hinge length at supports. Once again, there is the possibility to achieve greater values of the stress increment in unbonded tendons in comparison to simply supported members.

Table 7 contains values of the load pattern factor calculated in accordance with the above equations (4)–(6) compared to the results of numerical calculations. It could be observed that in the case of loading acting in 2 or 3 spans, values of stress increment in unbonded tendons could be as large or even greater than calculated for simply supported members. Results gained from numerical analysis contradict these outcomes. It has been proven that there are correlations between the number and the length of plastic hinges created at ultimate; moreover they indicate the importance of a plastic hinge formation sequence. The greatest stress increase in unbonded tendons has been obtained for simultaneously loading acting in both external spans. In this case plastifying of ordinary reinforcement occurs firstly in spans which enables the formation of long plastic hinges. Gained values of stress increase in unbonded tendons do not exceed 75% of values achieved for simply supported members. In other cases short plastic hinges were formed at supports and as a consequence low stress increase in prestressing steel was obtained. Its value was within the limit <13÷42> percent of the value received for simply supported members. It should be mentioned that increasing q_s factor compared to q_e factor does not lead to a lower stress increment in prestressing

steel despite the fact that such behaviour was observed in both experimental and theoretical research on simply supported members – on the contrary its increase was triggered. This could be explained by improved behaviour at support cross-sections and better redistribution of bending moments.

Table 7

Load patterns values – comparison of theoretical approaches and numerical results

	Loading pattern – Slab A						Loading pattern – Slab B					
Load combination	100	111	112	113	114	115	200	211	212	213	214	215
Parameter value (4)	1	1/3	1/3	2/3	2/3	1	1	1/3	1/3	2/3	2/3	1
Parameter value (5)	1	1/2	2/3	7/6	1	5/3	1	1/2	2/3	7/6	1	5/3
Parameter value (6)	14.0	19.2	24.5	43.7	38.4	62.9	14.0	19.2	24.5	43.7	38.4	62.9
$N_p/N_{p\ (1\ span)}$	100%	46%	58%	104%	92%	150%	100%	46%	58%	104%	92%	150%
Δf_{ps} [MPa] – DIANA	774	171	103	112	509	134	725	304	203	101	543	246
Δf_{ps} $\Delta f_{ps(1\ span)}$	100%	22%	13%	14%	66%	17%	100%	42%	28%	14%	75%	34%

It can be assumed that the last proposal of Harajli introducing the load pattern factor as a function of the number and the length of plastic hinges could be true but only in specific conditions. The following assumptions and limitations regarding the formation of plastic hinges are introduced by the author:

– all plastic hinges behave similarly i.e. the concrete compressive block depth c, depth and area of prestressing reinforcement d_{ps} and A_{ps} and ordinary reinforcement d_s and A_s are the same or very similar in all span and support cross-sections,
– the section is rectangular or has the rectangular section behaviour,
– stress increase at ultimate above the effective prestress Δf_{ps} is assumed to be not greater than $(0.95f_{py} - f_{se})$ which assures that the stress in tendons will not reach the yield strength of prestressing reinforcement.

According to the author of this paper, similar behaviour of all plastic hinges could be assured by simultaneous plastifying of ordinary reinforcement by the means below:

– bending moment equalisation in critical cross-sections,
  ○ span bending moments – changing multi-span member geometry, e.g. reducing lengths of the external span in comparison to internal spans,
  ○ support bending moments – tendon duct adjustment allowing unloading of internal supports,
– adding ordinary reinforcement at internal supports and external spans.

These treatments cannot be implemented for all possible load combinations due to the fact that the ratio of bending moments at the support and span will change and will be different for e.g. combination 113 and 114. It is recommended to arrange reinforcing bars in such a way that ordinary reinforcement will plasticise firstly in spans and then at supports. This

allows forming longer plastic hinges and benefitting from greater stress increase in unbonded tendons. However, the possibility to obtain stress increase in unbonded tendons in multi-span members at the same level as for simply supported members is doubtful.

It should be underlined that during the design process of multi-span members bending moment resistance of support and span cross-sections is calculated with usage of loading patterns giving maximum values of moments at crucial cross-sections. In prestressed structures post-tensioned with unbonded tendons, additional span loading (combinations 114 and 214) in comparison with single-span loading (combinations 111 and 211), could bring more advantages (greater stress increase in prestressing steel) than disadvantages (slightly greater bending moment). In the case of structures with a higher number of spans this phenomenon can also be observed during the dimensioning of support cross-section. Ultimate Limit State will not be reached by sophisticated loading pattern but for simple scheme where one, external span is loaded.

6. Final conclusions

The design process of multi-span structures post-tensioned with unbonded tendons can differ from that used for reinforced concrete, pretensioned and members post-tensioned with bonded tendons. It may appear that ULS is reached by different load patterns to which we got used to. Theoretical approaches proposed by various authors should be applied with caution. The possibility to achieve such a great stress increase as that found in simply supported members is questionable. Extending the bending resistance of the whole structure is connected with enabling the formation of long plastic hinges in spans via the arrangement of additional reinforcement at supports which assures the proper redistribution of bending moments.

References

[1] Building Code Requirements for Structural Concrete (ACI 318M–14).
[2] PN-EN 1992-1-1:2004 Eurokod 2: Projektowanie konstrukcji z betonu – Część 1: Reguły ogólne i reguły dla budynków.
[3] PN-B-03264:2002 Konstrukcje betonowe, żelbetowe i sprężone. Obliczenia statyczne i projektowanie.
[4] Naaman A., Alkhairi F., *Stress at Ultimate in Unbonded Post-Tensioning Tendons: Part II - Proposed Methodology*, ACI Structural Journal, Vol. 88, No. 6, 1991, 683–692.
[5] Harajli M., Hijazi S., *Evaluation of the Ultimate Steel Stress in Partially Prestressed Concrete Members*, PCI Journal, Vol. 36 No. 1 1991, 62–82.
[6] Harajli M., *On the Stress in Unbonded Tendons at Ultimate: Critical Assessment and Proposed Changes*, ACI Structural Journal, Vol. 103, No. 6, 2006, 803–812.

[7] Harajli M., *Tendon Stress at Ultimate in Continuous Unbonded Post-Tensioned Members: Proposed Modification of ACI 318, Eq. (18-4) and (18-5)*, ACI Structural Journal, Vol. 109, No. 2, 2012, 183–192.
[8] Burns N.H., Charney F.A., Vines W.R., *Tests of One Way Slabs with Unbonded Tendons*, PCI Journal, Vol. 23, No. 5, October 1978, 66–83.
[9] DIANA, *User's manual: Finite element analysis*, TNO DIANA, Delft.
[10] CHARLES PANKOW FOUNDATION RGA 04-13, *Determination of Yield Strength for Nonprestressed Steel Reinforcement*, Final Report December 31, 2013, WJE No. 2013.4171.

CONTENTS

TREŚĆ